

Influence of the ambient flow upon Rossby wave propagation between the tropics and extra-tropics

A dissertation submitted to the

ETH ZURICH

for the degree of

Doctor of Science

presented by

THOMAS SPENGLER

Dipl. Met. Ludwig Maximilian University of Munich, Munich, Germany

born 4 September 1978

citizen of Germany

accepted on the recommendation of

Prof. Dr. Huw C. Davies, examiner
em. Prof. Dr. Joseph Egger, co-examiner

2008

Contents

Abstract	v
Zusammenfassung	vii
1 Introduction	1
1.1 Motivation	1
1.2 Aims and objectives of this study	3
2 On stationary Rossby waves modified by basic shear	5
2.1 Introduction	5
2.2 Linear perturbation equations	6
2.3 Basic state zonal flow only varying in y direction	7
2.3.1 $\bar{u} = \Lambda y + U_0, \Lambda > 0$	7
2.3.2 $\bar{u} = \Lambda y^2, 0 < \Lambda < \frac{4}{5}\beta$	9
2.4 Barotropic model	11
2.4.1 $U_0 = 0 \text{ m s}^{-1}$	11
2.4.2 $U_0 = 10 \text{ m s}^{-1}$	13
2.5 Basic state zonal flow only varying in z direction	16
2.5.1 $\bar{u} = \Lambda z + U_0, \Lambda > 0$	17
2.5.2 $\bar{u} = \Lambda z^2, \Lambda > 0$	18
2.6 Discussion	20
2.7 Final remarks	21
3 Extra-tropical response to sub-tropical Forcing: Global simulations with an idealized jet	23
3.1 Introduction	23
3.2 Experiment setup	24
3.2.1 Model	24
3.2.2 Initial conditions	24
3.2.3 Stationary wave number/Ray tracing	26
3.3 The linear QG stationary response to orography	28
3.4 Global IFS simulations	30
3.4.1 Time evolution and vertical structure	31
3.4.2 Vertical structure along and to the north of the jet	33
3.4.3 Wave detection along and to the north of the jet	34
3.4.4 The southern hemisphere response	36
3.5 Discussion	39
3.5.1 Sensitivity to the size and height of the mountain	41
3.6 Final remarks	42
4 Extra-tropical response to stationary and non-stationary tropical heating: Non-linear global simulations with a zonally asymmetric jet stream	45
4.1 Introduction	45
4.2 Experiment setup	46
4.2.1 Model	46
4.2.2 Initial conditions	47
4.2.3 Definition of the heating	47

4.3	Method	49
4.4	Response to stationary heating	50
4.4.1	Time evolution	50
4.4.2	Vertical structure	54
4.4.3	Extent of perturbation versus distance to wave guide	55
4.4.4	Response pole-ward of wave guide	57
4.4.5	Sensitivity to the amplitude and size of the forcing	58
4.5	Response to non-stationary heating	59
4.5.1	Time evolution	59
4.5.2	Vertical structure	61
4.6	Discussion	62
4.7	Final remarks	62
5	Concluding remarks and Outlook	65
	Bibliography	67
	Curriculum Vitae	73
	Acknowledgements	76

Abstract

Global teleconnection patterns identified by principal component analysis pinpoint leading patterns of atmospheric variability. In addition they also indicate a possible dynamical linkage between distant regions on the globe. The physical mechanisms involved in the initiation of these patterns has been intensively investigated for the last decades. However, there are still controversial views on the mechanisms involved in the generation of teleconnection patterns. There are e.g. three proposed mechanisms for the Pacific/North America teleconnection pattern (PNA): Stationary Rossby wave propagation along great circles, unstable modal barotropic growth on the climatological mean winter state or interactions between the transient and mean atmospheric flow. In this study the focus is on the plausibility of the proposed mechanisms and will be elaborated by means of theoretical deductions and model simulations.

Non-divergent barotropic stationary Rossby waves on the sphere transmit energy along ray path resembling great circles, where the stationary wave number is the key parameter determining the lateral reach of the perturbations. The obtained patterns of wave propagation on a climatological winter mean basic state bear great similarities with the PNA encouraging the interpretation of this teleconnection pattern by means of stationary Rossby wave propagation. However, the choice of a climatological mean state is somewhat equivocal, especially since recent studies pinpointed the sub-monthly time-scale of the PNA rendering stationary Rossby wave propagation on a multi-year seasonal time mean questionable. Thus it is desirable to study the impact of a more day-to-day weather situation on the propagability of stationary Rossby waves in the atmosphere shedding light on the fact if the argumentation based on a climatological mean state still holds.

In the study presented here the propagability of stationary Rossby waves is first investigated by means of a theoretical deduction utilizing different dynamical frameworks with idealized meridionally varying basic states. It is shown that lateral propagation is strongly reduced for increasing environmental shear and in fact propagation is even prohibited if a certain threshold of the shear parameter is exceeded.

The second part of the study comprises global model simulations on the sphere with a zonally symmetric barotropic jet. A circular mountain serves as a wave maker in the tropical and subtropical latitudes. Strong sensitivities are found with respect to the strength of the jet as well as to the relative position of the mountain. For reduced maximum jet speeds it is shown that stationary Rossby wave propagation along great circles is still feasible for higher zonal wave numbers. However for maximum zonal jet speeds in excess of a certain threshold value no evidence is found for wave trains along a great circle resembling similarity to the PNA. Instead the response pole-ward of the jet is characterized by a zonal wave number one pattern. The results are shown to be in general agreement with linear barotropic and quasigeostrophic theory.

In the last part of the thesis non-linear global model simulations are presented initialized with a baroclinic and meandering jet. The setup is designed to mimic a more day-to-day like weather situation compared to the idealized settings in the first part of the thesis. Furthermore the strongly varying structures contrast the background states of earlier studies using linearizations about a climatological mean state. The response to a tropical heating is investigated pinpointing dependencies of its amplitude and downstream extent on distinct features along the mid-latitude wave guide. It is shown that a tropical heating always triggers a downstream development along the mid-latitude wave guide (jet stream) resembling the characteristics of a growing baroclinic disturbance. The leading edge of the response along the wave guide progresses with a speed comparable to the mean zonal jet speed at upper levels. Within the first 15 days of time integration some experiments feature an appreciable response pole-ward of the jet. However, the pole-ward response is generally not attributable to linear stationary Rossby wave propagation and is in fact due to a pole-ward shift of preexisting troughs and ridges or in fact to wave breaking

events. The latter findings disclose the highly non-linear character of the dynamics involved in producing the response to the north of the wave guide.

Zusammenfassung

Globale Telekonnektionsmuster, welche durch Hauptkomponentenanalyse bestimmt wurden, zeigen die maßgebenden Strukturen von atmosphärischer Variabilität. Zusätzlich verweisen sie auch auf mögliche dynamische Interaktionen zwischen entfernten Regionen auf dem Erdball. Die physikalischen Mechanismen welche zur Initiierung diese Muster beitragen wurden in den letzten Dekaden intensiv untersucht. Allerdings gibt es nach wie vor kontroverse Sichtweisen über die verschiedenen Mechanismen die mit der Erzeugung dieser Telekonnektionsmuster verbunden sind. So werden z.B. im wesentlichen drei verschiedene Mechanismen für die Entstehung des Pacific/North America Telekonnektionsmusters (PNA) vorgeschlagen: Ausbreitung von stationären Rossbywellen entlang von Grosskreisen, instabiles modales barotropes Wachstum von Störungen auf dem mittleren klimatologischen Zustand der nördlichen Winteratmosphäre oder die Interaktion zwischen transienten und mittleren atmosphärischen Zustandsgrößen. Das Hauptaugenmerk der vorliegenden Studie zielt auf die Plausibilität der vorgeschlagenen Mechanismen. Die Untersuchungen basieren auf theoretischen Herleitungen und numerischen Modellsimulationen.

Die Energie divergenzfreier barotroper Rossbywellen auf einer Kugel breitet sich entlang von Grosskreisen aus, wobei die stationäre Wellenzahl den Schlüsselparameter darstellt welcher die laterale Reichweite der Störung determiniert. Die erhaltenen Muster von Wellenausbreitung auf einem mittleren klimatologischen Winterzustand der Atmosphäre weisen große Ähnlichkeit zum PNA auf. Dieser Fakt bestärkt die Interpretation dieses Telekonnektionsmusters durch Ausbreitung von stationären Rossbywellen. Allerdings ist die Wahl eines klimatologischen Hintergrundzustandes fragwürdig, vor allem da jüngere Veröffentlichungen auf die sub-monatige Zeitskala des PNA verwiesen und somit die Ausbreitung stationärer Rossbywellen auf einem mehrjährigen Mittel zweifelhaft erscheint. Folglich ist es wünschenswert den Einfluss eines Hintergrundzustandes auf die Ausbreitungsmöglichkeiten von stationären Rossbywellen zu untersuchen um somit Aufschluss über die Gültigkeit der Argumentation basierend auf einem klimatologischen Hintergrund zu geben.

In der vorliegenden Studie wird die Ausbreitung von stationären Rossbywellen zuerst unter Zuhilfenahme theoretischer Herleitungen in verschiedenen dynamischen Bezugssystemen mit idealisierten meridional variierenden Hintergrundzuständen untersucht. Es zeigt sich, dass die laterale Ausbreitung stark reduziert ist für eine Zunahme der Scherung des Hintergrundzustandes. In der Tat ist die Wellenausbreitung nicht möglich sobald der Scherungsparameter einen bestimmten Wert überschreitet.

Der zweite Teil der Studie beinhaltet globale Modellsimulationen auf der Erdkugel mit einem zonal-symmetrischen Strahlstrom. Ein runder Berg dient als Wellenerzeuger in den tropischen und subtropischen Breitengraden. In den Resultaten wurden starke Sensitivitäten gegenüber der Geschwindigkeit des Strahlstroms sowie gegenüber der relativen Position des Berges gefunden. Für geringere maximale Geschwindigkeiten des Strahlstroms ist eine Ausbreitung von stationären Rossbywellen entlang von Grosskreisen noch möglich. Für maximale Windgeschwindigkeiten oberhalb eines Schwellwertes gibt es allerdings keine Anzeichen mehr für Wellenausbreitung entlang von Grosskreisen welche mit dem PNA in Übereinklang gebracht werden können. Stattdessen sind die Störungen polwärts des Strahlstroms charakterisiert durch ein Muster mit einer zonalen Wellenzahl von eins. Es wird gezeigt, dass die präsentierten Resultate in Vereinbarung mit linearer barotroper und quasigeostrophischer Theorie sind.

Im letzten Teil der Dissertation werden nicht-lineare globale Modellsimulationen präsentiert welche mit einem baroklinen und meandrierender Strahlstrom initialisiert wurden. Diese Konfiguration wurde erstellt um das tägliche Wettergeschehen zu imitieren im Kontrast zu den ersten beiden Studien welche sich auf sehr idealisierte Hintergrundzustände beschränken. Des Weiteren sind die hier gewählten Strukturen in Kontrast zu Hintergrundzuständen früherer linearer Studien welche auf einem klimatologis-

chen Mittel als Hintergrundzustand basieren. Die Reaktionen auf eine diabatische Wärme-quelle in den Tropen zeigt die Sensitivitäten der Amplitude und der Reichweite der generierten Störung in Bezug auf verschiedene Strukturen des Wellenleiters in den mittleren Breiten. Es zeigt sich, dass ein diabatischer Antrieb in den Tropen immer eine Entwicklung stromabwärts entlang des Wellenleiters (Strahlstroms) auslöst welche die Eigenschaften einer wachsenden baroklinen Störung hat. Die vordere Flanke der Störung breitet sich mit einer Geschwindigkeit entlang des Wellenleiters aus welche vergleichbar zur mittleren zonalen Geschwindigkeit des Strahlstroms ist. Einige Experimente enthalten eine nennenswerte Störung polwärts des Strahlstroms innerhalb der ersten 15 Tage der Modellintegration. Allerdings ist diese Störung in der Regel nicht einer linearen stationären Ausbreitung einer Rossbywellen zuzuschreiben. Die Ursache liegt vielmehr in der Vertiefung von schon existierenden Trögen oder Rücken oder ist sogar durch Wellenbrechen hervorgerufen. Die zuletzt genannten Befunde verweisen auf den hochgradig nicht-linearen Charakter der involvierten dynamischen Prozesse welche für die Störungen nördlich des Strahlstroms verantwortlich sind.

Chapter 1

Introduction

The aim of this study is to shed light on the generation and propagation of global circulation patterns. In particular the initiation and propagation of Rossby waves in zonally and meridionally varying background flows is investigated by means of theoretical and numerical studies.

1.1 Motivation

The climate of the earth features distinct asymmetries in the latitudinal and longitudinal directions. The asymmetry in the meridional direction stems to first order from the different angles of the sun, yielding different amounts of insolation at different latitudes. The origin of asymmetries in the zonal direction are related to the zonally varying lower boundary condition, represented by orography and land-sea contrast. These effects can be further augmented by dynamical and diabatic effects.

An early study of the contribution of the earth's orography to the climatological mean state of the atmosphere was carried out by Charney and Eliassen (1949) utilizing stationary quasigeostrophic theory. They attributed a large fraction of the zonal asymmetry of the climate to the main mountain ranges on the planet. Later Smagorinsky (1953) investigated the contributions from diabatic heating. The studies above were extended (e.g. Egger, 1976a,b; Grose and Hoskins, 1979; Webster, 1972; Simmons, 1982; Valdes and Hoskins, 1989; Ting, 1994; Wang and Ting, 1999) using linear and non-linear global simulations. In general the studies listed above were able to reconstruct the observed climatological mean structures quite well indicating the importance of the earth orography and diabatic heating on the formation of the zonal asymmetry of the climate. Held et al. (2002) give a review on the theory and modeling of these stationary waves.

Complementary to the time mean view on climate, Walker (1909) used the one-point correlation technique to pinpoint possible dynamical linkages between distant regions on the globe. Several surveys applying this approach followed identifying well known patterns of atmospheric variability such as the Arctic Oscillation (Exner, 1913) or the North Atlantic Oscillation (NAO Defant, 1924; Exner, 1924) followed by the milestone paper of Walker (1924) where he describes three dominant modes of variability of the world weather (North Atlantic Oscillation, North Pacific Oscillation and Southern Oscillation). In a later paper Walker and Bliss (1932) extended the data analysis by a more comprehensive approach which can be seen as an approximation to a principal component analysis which became widely used in atmospheric sciences thereafter.

However, the data coverage at that time was rather limited especially regarding the area over the oceans and some time passed by before Wallace and Gutzler (1981) and Horel and Wallace (1981) published their influential papers on global teleconnection patterns. The most prominent patterns described in their studies are the Pacific/North America pattern (PNA) and the NAO. Jakob Bjerknes (Bjerknes, 1964, 1966, 1969), who actually established the term "teleconnections" in atmospheric sciences, was among the first trying to dynamically explain these patterns and hypothesized that the connection from one part of the planet to another is explainable by sea surface temperature - sea level pressure interactions.

Hoskins and Karoly (1981) investigated the response of a spherical atmosphere to thermal and orographic forcing utilizing a linearized steady-state five-layer baroclinic model showing that an easy way to produce an appreciable response in the middle and high latitudes is by subtropical forcing. The technique of ray-tracing (adapted from optics) proved to be useful in identifying preferred paths of stationary

Rossby wave propagation. The method basically relies on the WJKB (Wentzel, 1926; Jeffreys, 1924; Kramers, 1926; Brillouin, 1926) approximation, i.e. assuming slow variations of the basic state compared to the scale of the perturbations. The rays are parallel to the local group velocity of stationary Rossby waves. It was shown that stationary Rossby waves are generally refracted towards higher values of the stationary wave number which is basically determined by the basic state and the zonal wave number of the wave to be tracked. Hoskins and Karoly (1981) pointed out an increased pole-ward reach for Rossby waves with smaller zonal wave numbers. For the climatological mean winter flow Hoskins and Ambrizzi (1993) pinpointed strong sensitivities of stationary Rossby wave propagation to the background state showing the existence of wave guides as well as regions which are preferred for propagation.

There are a number of studies relating the growth of low-frequency patterns such as the PNA to linear dispersion of Rossby waves from a source of tropical heating via energy transmission along ray paths resembling great circles (Hoskins et al., 1977; Hoskins and Karoly, 1981) producing patterns like the PNA. Studies mainly comprise a stationary (Lim and Chang, 1983; Branstator, 1985; Sardeshmukh and Hoskins, 1988; Ting and Sardeshmukh, 1993; Ting and Yu, 1998) or non-stationary (Jin and Hoskins, 1995) approach linearized about idealized basic states or the climatological mean winter flow. Other studies invoke a barotropic instability due to the zonal asymmetry of the climatological winter mean state as the key mechanism (Simmons et al., 1983; Frederiksen, 1983; Frederiksen and Webster, 1988; Branstator, 1990, 1992). However, it was shown that small changes in the damping or in the forcing eliminate the instability (Borges and Sardeshmukh, 1995; Ting and Sardeshmukh, 1993; Ting and Yu, 1998) casting doubt on role of the proposed mechanism. Further studies indicate the importance of high-frequency eddy feedbacks on the time mean state of the atmosphere in generating low-frequency variability patterns such as the PNA (Egger and Schilling, 1983; Nakamura and Wallace, 1993; Branstator, 1995; Jin et al., 2006).

It is interesting to note that whereas the PNA is seen as a pattern of seasonal variability Feldstein (2002) showed that the PNA anomaly completes its life cycle within 2 weeks indicating the sub-monthly character of the dynamics involved in its generation highlighting the importance of sub-seasonal dynamics in the generation of the PNA.

In general the studies listed above point to the importance of a tropical forcing in the equatorial Pacific as a trigger for the perturbations in the extra-tropics resembling the PNA. One of the most prominent patterns of tropical variability connected to outbreaks of strong convective activity, and thus diabatic heating, is the Madden-Julian Oscillation (MJO) with a recurrence of about 40 days (Madden and Julian, 1971, 1972, 1994; Zhang, 2005). During its convective active phase the MJO is characterized by a slowly eastward progressing (5 m s^{-1}) conglomeration of convection along the equator, where the active phase is limited to the Indian and eastern to central Pacific Ocean (Hendon and Salby, 1994; Matthews, 2000; Zhang, 2005). There have been several studies investigating the impacts of the MJO on the mid-latitudes by means of data analysis and composite studies (Liebmann and Hartmann, 1984; Lau and Phillips, 1986; Knutson and Weickmann, 1987; Kiladis and Weickmann, 1992; Hsu, 1996; Higgins and Mo, 1997; Matthews and Kiladis, 1999; Kim et al., 2006) or modeling approaches (Salby et al., 1994; Hendon and Salby, 1996; Matthews et al., 2004). The MJO was shown to have a significant impact on the mid-latitudes by initiating global circulation patterns as well as changing the Pacific wave guide. Recently Mori and Watanabe (2008) investigated the direct impact of the MJO on the PNA by examining composite life cycles of the PNA. They found a strong coherence between the MJO and the development of a wave train along the Pacific wave guide which they hypothesize to be generated by the divergent winds primarily associated with anomalous convection of the MJO.

The studies listed above try to describe the dynamical mechanisms involved in the interaction of a tropical diabatic heating (as comprised e.g. by the MJO) and the mid-latitude wave guide mainly based on composite analysis or theories relating evolutions on synoptic time-scales to low-frequency variability. However, the day-to-day high-frequency interactions are still yet to be determined. The wave train along the Pacific wave guide initiated by the MJO (Mori and Watanabe, 2008) resembles the characteristics of a downstream development (Simmons and Hoskins, 1979; Chang, 1993; Chang and Yu, 1999;

Chang, 1999). Hakim (2003) and Danielson et al. (2006) also investigated the occurrence and dynamics of downstream development in the Pacific sector. Latter study successfully used wave activity fluxes (Takaya and Nakamura, 1997a,b) to diagnose the downstream progression of wave energy. However, it should be noted that our dynamical understanding of downstream development, especially the determination of the phase and group velocity of the perturbation, is still rather limited (Chang, 1999; Hakim, 2003). Since Mori and Watanabe (2008) clearly indicate a relationship between the MJO and a subsequent downstream development along the Pacific mid-latitude wave guide it is desirable to gain a better understanding of the dynamics involved in the initiation of the wave train by tropical convection. It should also be noted that the forecast performance on the onset and the progression of the MJO is still very poor in today's numerical weather prediction model (Ferranti et al., 1990; Hendon et al., 2000; Zhang et al., 2006; Moncrieff et al., 2008).

1.2 Aims and objectives of this study

The aim of this study is to shed light on the generation and propagation of global circulation patterns. In particular the initiation and propagation of Rossby waves in zonally and meridionally varying background flows is investigated by means of theoretical and numerical studies, where the primary focus in the study presented here is on the PNA teleconnection pattern.

Some of the key hypotheses addressed in this thesis are:

- Strong meridional shear of the zonal flow evident in day-to-day weather situation (compared to climatological mean states) impacts significantly on the propagability of stationary Rossby wave propagation.
- Stationary Rossby wave propagation along great circles is not realizable if the background state exhibits a strong jet stream.
- The character of the dynamics involved in teleconnection patterns is not solely attributable to stationary Rossby waves propagating along great circles and the comprehension of non-linear effects, i.e. interactions between the forcing and the jet stream as well as interaction of the triggered perturbations along the jet stream with the background state, is in fact important.

The first hypothesis is tested in chapter 2 by means of a linear investigation of propagability in a linear analytic model pinpointing the behavior of meridional Rossby wave propagation through idealized basic states. The main focus is on the meridional reach of the perturbations in order to better understand the impact of subtropical Rossby waves on the mid-latitude wave-guide (jet stream).

The second hypothesis is elaborated in chapter 3 where the non-linear evolution in time and space of stationary Rossby wave patterns in a three dimensional global model is investigated. The initial state of the atmosphere constitutes a zonally symmetric barotropic jet in each hemisphere where a single mountain located alternatively in the tropical or subtropical latitudes acts as a wave maker on an otherwise flat planet. The key interests are the sensitivities of the response to the latitude of the forcing and to the strength of the jet. The idealized nature of the setup helps to shed light on the dynamical features of wave propagation based upon adopting barotropic and quasigeostrophic Rossby wave theory.

In chapter 4 the focus is on the non-linear interaction between a prescribed stationary or migratory tropical heating with the extra-tropical flow and hence relating to the third hypothesis. A model setup is chosen which allows for the maintenance of a time-evolving meandering baroclinic mid-latitude jet in each hemisphere enabling an interpretation of the results beyond the realm of linearity and with a more complex and asymmetric nature of the atmosphere compared to a climatological mean.

Chapter 2

On stationary Rossby waves modified by basic shear

2.1 Introduction

Stationary Rossby waves in response to thermal and orographic forcing constitute a large fraction of the zonal asymmetry of the climatological mean state of the atmosphere (e.g. Charney and Eliassen, 1949; Smagorinsky, 1953; Egger, 1976a,b; Grose and Hoskins, 1979). Also one of the leading patterns of seasonal variability, the Pacific/North America (PNA) teleconnection pattern identified via one point correlations of the 500 hPa geopotential by Wallace and Gutzler (1981), is often thought to be resembled by stationary Rossby waves emanating out of the tropics where they are proposed to be triggered by diabatic heating and subsequent divergent outflow (e.g. Hoskins and Ambrizzi, 1993; Lim and Chang, 1983; Branstator, 1985; Sardeshmukh and Hoskins, 1988; Ting and Sardeshmukh, 1993; Ting and Yu, 1998).

Hoskins and Karoly (1981) investigated the response of a spherical atmosphere to thermal and orographic forcing utilizing a linearized steady-state five-layer baroclinic model showing that the easiest way to produce an appreciable response in the middle and high latitudes is by subtropical forcing. The technique of ray-tracing was proven to be useful in identifying preferred paths of stationary Rossby wave propagation. The method basically relies on the WJKB approximation, i.e. assuming slow variations of the basic state compared to the scale of the perturbations. It was shown that the zonal wave number k remains constant along the ray path within this framework. Thus the meridional wave number can be determined locally from the total stationary wave number $\left(K_s = \sqrt{\frac{\beta - \bar{u}_{yy}}{\bar{u}}}\right)$. The rays are parallel to the local group velocity of stationary Rossby waves. It was shown that stationary Rossby waves are generally refracted towards higher values of the stationary wave number. Furthermore Hoskins and Karoly (1981) pointed out an increased pole-ward reach for Rossby waves with smaller zonal wave numbers. For the climatological mean winter flow Hoskins and Ambrizzi (1993) pinpointed strong sensitivities of stationary Rossby wave propagation to the background state showing the existence of wave guides as well as regions which are preferred for propagation.

The motivation for the present study is to pinpoint the behavior of meridional Rossby wave propagation through idealized basic states. We consider analytic solutions of a steady-state linearized model on a β -plane, where the model framework comprises the barotropic, quasigeostrophic shallow-water (QGSW) or stratified QG set of equations, respectively. Two idealized ambient zonal flow profiles, i.e. a linear ($\bar{u} = \Lambda y + U_0$) and a parabolic profile ($\bar{u} = \Lambda y^2$) are chosen for discussion. The main focus here is on the meridional reach of the perturbations. This, for example, is of interest in order to better understand the impact of subtropical Rossby waves on the mid-latitude wave-guide (jet stream), since the waves have to propagate through non-uniform basic states to reach higher latitudes. We also discuss trapped modal waves which were identified for the linear basic state profile.

In addition to the horizontal propagation of stationary Rossby waves in a meridionally varying basic state we also present results for vertically propagating Rossby waves in the QG framework, where we assume linear ($\bar{u} = \Lambda z + U_0$) and parabolic ($\bar{u} = \Lambda z^2$) variations of the zonal basic state in the vertical. The non-stationary solution of the linear profile, i.e. the baroclinic instability problem, is extensively discussed in the literature (e.g. Charney, 1947; Eady, 1949). The vertical propagation of planetary Rossby waves was also identified to play a crucial role in the transfer of momentum upward into the Stratosphere (e.g. Eliassen and Palm, 1961; Charney and Drazin, 1961). Furthermore the dynamics of Stratospheric

Sudden Warmings are also linked to vertically propagating planetary waves (Matsuno, 1971).

In section 2.2 we derive the linearized vorticity equations for the respective dynamical frameworks. The results for the linear and parabolic meridional profile are derived in section 2.3. Numerical simulations utilizing a linear barotropic model initialized with linear and parabolic basic zonal flow are presented in section 2.4. The results for the linear and parabolic vertical profile are derived in section 2.5 followed by the discussion in section 2.6. Final remarks are given in section 2.7.

2.2 Linear perturbation equations

To discuss the horizontal and vertical propagation of linear Rossby waves in different dynamical frameworks we derive the respective potential vorticity equations for the barotropic, the QGSW and the stratified QG system assuming a zonal flow basic state which varies in the y -direction ($\bar{u}(y)$). For the QG approximation we also discuss a zonal basic state with variations in the z -direction ($\bar{u}(z)$).

Utilizing the QG vorticity equation (e.g. Pedlosky, 1987)

$$\frac{D_g}{Dt} \left(\Delta \Psi + \frac{f_0^2}{\rho_0} \left(\frac{\rho_0}{N^2} \Psi_z \right)_z \right) + \beta v_g = 0 \quad (2.1)$$

$$\frac{D_g}{Dt} = \frac{\partial}{\partial t} + u_g \frac{\partial}{\partial x} + v_g \frac{\partial}{\partial y} \quad (2.2)$$

where $N^2 = \frac{g}{\theta_0} \frac{d\theta_0}{dz}$ is the background stratification, Ψ is the QG stream function, f_0 is the Coriolis parameter and β its derivative in the y -direction, and $\rho_0(z)$ is the background density varying with height.

We now linearize equation (2.1) around a basic state zonal flow $\bar{\mathbf{v}} = (\bar{u}(y, z), 0)$

$$u_g = \bar{u}(y, z) + u' \quad (2.3)$$

$$v_g = v' \quad (2.4)$$

$$\theta = \bar{\theta}(y, z) + \theta' \quad (2.5)$$

which, assuming $N^2 = \text{const}$, $\rho_0 = \rho_{00} e^{-\frac{z}{H}}$ and substituting $\Psi = \Phi e^{\frac{1}{2H}z}$, yields

$$\begin{aligned} & \left(\frac{\partial}{\partial t} + \bar{u} \frac{\partial}{\partial x} \right) \left(\Delta_h \Phi + \frac{f_0^2}{N^2} \left(\Phi_{zz} - \frac{1}{4H^2} \Phi \right) \right) \\ & + \left(\beta - \bar{u}_{yy} - \frac{f_0^2}{N^2} \left(\bar{u}_{zz} - \frac{1}{H} \bar{u}_z \right) \right) \Phi_x = 0 \end{aligned} \quad (2.6)$$

(2.6) can be solved by defining

$$\Phi = \chi(y, z) e^{i(kx - \omega t)} \quad (2.7)$$

where $\chi(y, z)$ denotes the variations in the y and z -direction. Whereupon we obtain

$$\chi_{yy} + \frac{f_0^2}{N^2} \chi_{zz} + \left[\frac{\left(\beta - \bar{u}_{yy} - \frac{f_0^2}{N^2} (\bar{u}_{zz} - \frac{1}{H} \bar{u}_z) \right)}{(\bar{u} - c)} - \left(k^2 + \frac{f_0^2}{4N^2 H^2} \right) \right] \chi = 0 \quad (2.8)$$

(2.8) reduces to the corresponding barotropic or QGSW equation if variations in the z -direction are neglected and $H \rightarrow \infty$ or $g\bar{h} = 4N^2 H^2$, respectively. For the derivation of the QGSW equation we followed Pedlosky (1987) assuming the zonal basic state to be balanced by an external pressure force. The advantage of the latter assumption is that the surface of the mean depth of the fluid is allowed to be constant.

2.3 Basic state zonal flow only varying in y direction

Considering a linear ($\bar{u} = \Lambda y + U_0$) and a parabolic ($\bar{u} = \Lambda y^2$) profile for the zonal flow basic state we derive solutions for $\chi(y)$ where we assume wave-like behavior in the z -direction for the QG system (i.e. $\Phi = \chi(y)e^{i(kx+mz)}$). The focus is a priori on stationary wave propagation, i.e. $c = 0$.

2.3.1 $\bar{u} = \Lambda y + U_0$, $\Lambda > 0$

We can rewrite (2.8)

$$\chi_{yy} + \left(\frac{\beta}{\Lambda y + U_0} - \lambda^2 \right) \chi = 0 \quad (2.9)$$

where

$$\lambda^2 = k^2 + \frac{f_0^2}{N^2} m^2 + \frac{f_0^2}{4N^2 H^2} \quad (2.10)$$

for the barotropic ($m = 0$ and $H \rightarrow \infty$), the QGSW ($m = 0$ and $g\bar{h} = 4N^2 H^2$, where \bar{h} is the constant mean depth of the fluid) and the QG system.

(2.9) is a second order differential equation which has wave type solutions for $\frac{\beta}{\Lambda y + U_0} > \lambda^2$ and evanescent solutions for $\frac{\beta}{\Lambda y + U_0} < \lambda^2$. It is worthwhile briefly discussing the nature of propagability in the system above. For any given λ , β , Λ and U_0 there will be a certain value of y where the denominator of the first term in the brackets in (2.9) will eventually become large enough to prohibit wave propagation. It is also obvious from (2.9) that the reach of propagability in the y -direction will be enhanced for smaller values of Λ (i.e. reduced shear) and/or smaller values of λ (i.e. smaller zonal and/or vertical wave numbers or a shallower fluid in the QGSW framework). Thus larger and more barotropic like (m very small or zero) perturbations are able to penetrate further through shear than smaller scale perturbations with a rich structure in the vertical. Therefore (2.9) together with (2.10) also illustrate that one might overestimate propagability in a purely barotropic system compared to stratified QG theory. As $y \rightarrow -\frac{U_0}{\Lambda}$ the first term in the brackets becomes infinite indicating a decrease in the wave length in the y -direction.

In order to solve (2.9) we can define

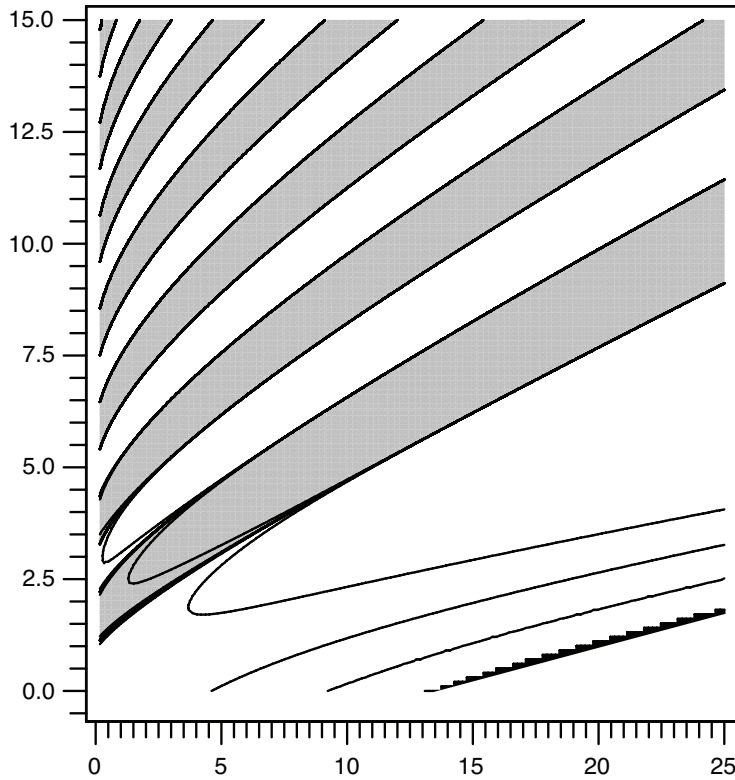


Figure 2.1: Contour plot of $W_{\kappa, \nu}(\gamma y)$ or $W_{\kappa, \nu}(\gamma z)$. Negative values shaded. The abscissa is γy or γz and the ordinate is κ for the linear horizontal ($\bar{u} = \Lambda y$) and linear vertical ($\bar{u} = \Lambda z$) profile, respectively. Contours are drawn every $\pm 10^x$, where $x = [-10, 9, \dots, 9, 10]$.

$$\kappa = \frac{\beta}{2\Lambda\lambda} \quad (2.11)$$

$$\nu = \frac{1}{2} \quad (2.12)$$

$$\gamma = 2\lambda \quad (2.13)$$

and end up with solutions for $\chi(y)$ (see pp 504 Abramowitz and Stegun, 1964)

$$\chi(y) = \Re \left\{ C_1 M_{\kappa, \nu} \left(\gamma y + \frac{\gamma U_0}{\Lambda} \right) + C_2 W_{\kappa, \nu} \left(\gamma y + \frac{\gamma U_0}{\Lambda} \right) \right\} \quad (2.14)$$

where $C_{1/2}$ are constants and $M_{\kappa, \nu}$ and $W_{\kappa, \nu}$ are the Whittaker functions of the first and second kind, respectively. κ represents the ratio of the planetary vorticity gradient to the shear parameter and λ . Hence κ is a measure of wave propagability. For $\kappa \ni \mathbb{N}$, $M_{\kappa, \nu}$ has only unbound solutions for $y \rightarrow \infty$. Thus we first focus on the contribution to the solution from $W_{\kappa, \nu}$ which takes the form of a purely decaying function for $\kappa < 1$, whereas for $\kappa \geq 1$ the solution becomes wave like up to a certain value of γy . The scaling in the y direction with γ illustrates the sensitivity of the reach in the y -direction to the zonal and

vertical structure of the perturbation as discussed above. Solutions for $\chi(y)$ are shown in Fig. 2.1, where the abscissa and ordinate are γy and κ , respectively. The grey shading indicates negative values. Bearing in mind that κ increases for decreasing Λ it is evident that the ability of wave propagation is reduced for stronger shear.

If the boundary condition $\chi(y = -\frac{U_0}{\Lambda}) = 0$ is requested, $M_{\kappa, \nu}$ has trapped modal solutions for $\kappa = 1, 2, 3, \dots$, which are shown for the first three modes in Fig 2.2 where the abscissa is chosen to be γy again.

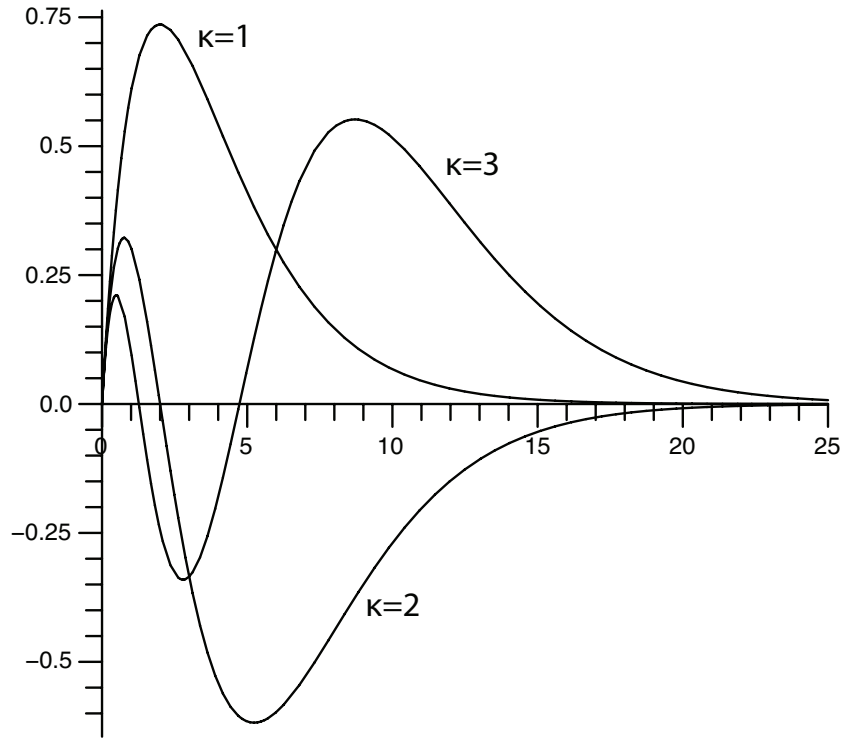


Figure 2.2: Modal solutions for $\kappa = 1, 2, 3$. The abscissa is γy or γz for the linear horizontal ($\bar{u} = \Lambda y$), or the linear vertical ($\bar{u} = \Lambda z$) and the parabolic vertical ($\bar{u} = \Lambda z^2$) profile, respectively.

2.3.2 $\bar{u} = \Lambda y^2, 0 < \Lambda < \frac{4}{5}\beta$

Using λ from above, (2.8) can be rewritten for the parabolic profile yielding

$$\chi_{yy} + \left(-\lambda^2 - \frac{\nu^2 - \frac{1}{4}}{y^2} \right) \chi = 0 \quad (2.15)$$

where

$$\nu^2 = \frac{5\Lambda - 4\beta}{4\Lambda} \quad (2.16)$$

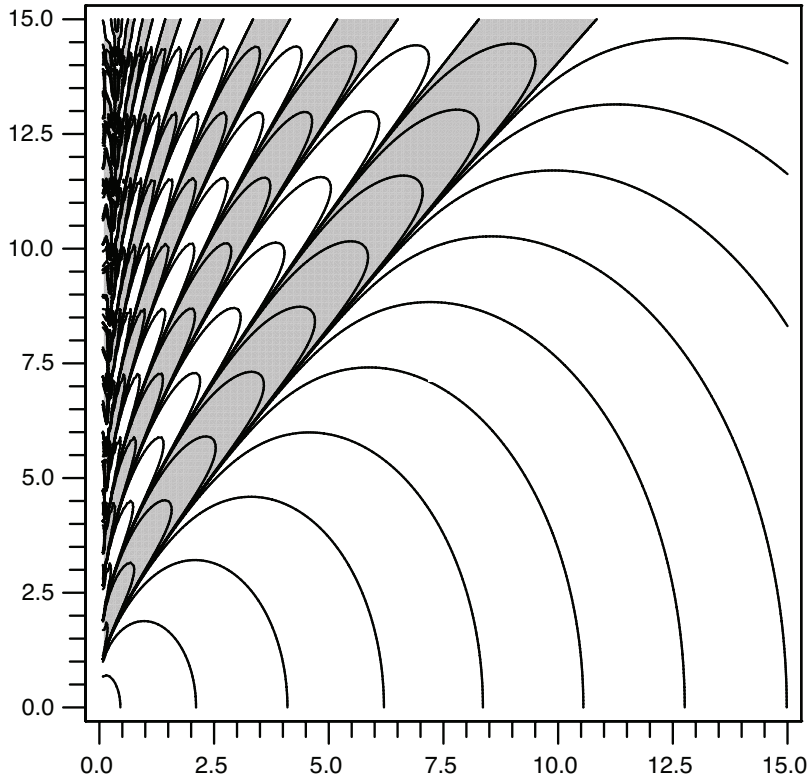


Figure 2.3: Contour plot of $K_v(\lambda y)$. Negative values shaded. The abscissa is λy and the ordinate is $\Im(v)$ for the parabolic horizontal profile ($\bar{u} = \Lambda y^2$). Contours are drawn every $\pm 10^x$, where $x = [-10, 9, \dots, 9, 10]$.

(2.15) is a second order differential equation with similar properties as discussed for (2.9), i.e. wave propagation only exists for $\left(-\lambda^2 - \frac{v^2 - \frac{1}{4}}{y^2}\right) > 0$, where v is the key parameter of propagability here representing the ratio of the planetary vorticity gradient and basic state shear. Since v is imaginary for the values of Λ chosen here, $v^2 < 0$. Thus for increasing y the second term in the brackets will eventually become small enough to prohibit wave propagation. The reach is again primarily determined by the shear parameter and the zonal and vertical structure of the perturbation, where an increase in shear and/or zonal and vertical structure reduces the propagability.

Following pp 355 in Abramowitz and Stegun (1964) we obtain solutions for (2.15) of the form

$$\chi(y) = \Re \{ C_1 \sqrt{y} I_v(\lambda y) + C_2 \sqrt{y} K_v(\lambda y) \} \quad (2.17)$$

where I_v and K_v are the 2. Order modified Bessel functions of the first and second kind, respectively. A similar solution was found by Wurtele et al. (1987) for vertically propagating gravity waves in a parabolic shear environment. For imaginary v , I_v is unbound for $y \rightarrow \infty$, thus we discard this contribution to the solution. K_v exhibits wave like behavior in y for $\Im(v) \geq 1$, whereas the solutions become purely decaying for $\Im(v) < 1$. Fig. 2.3 shows a contour plot (negative values shaded) of the solution, where the abscissa and ordinate are λy and $\Im(v)$, respectively. In the solution displayed in Fig. 2.3 we neglected the contribution from the \sqrt{y} term in (2.17). One should bear in mind that $\Im(v)$ is decreasing for increasing

Λ . Thus an increase in Λ reduces the ability of wave propagation in the y -direction. Like for the linear shear profile the scaling of the y -axis with λ illustrates the dependence of the reach of the waves to their zonal and vertical structure, featuring a further reach for larger scale perturbations with reduced vertical structure.

2.4 Barotropic model

Supplementary to the analytic solutions we integrated the barotropic vorticity equation linearized around similar background states ($\bar{u} = U_0 + \Lambda y$ and $U_0 + \Lambda y^2$) forward in time until the model reached a steady state. Here we force the vorticity equation by a prescribed divergence pattern

$$\zeta_t + \bar{u}\zeta_x + (\beta - \bar{u}_{yy})v = -fD - \nu\zeta \quad (2.18)$$

where f is the Coriolis parameter, $\nu\zeta$ represents a linear damping term ($\nu = 2 \times 10^{-6} \text{ s}^{-1}$) and

$$D = \begin{cases} A(x) \left(\cos\left(\frac{\pi(x-x_0)}{d}\right) \cos\left(\frac{\pi(y-y_0)}{d}\right) \right)^2 & \text{if } |x-x_0|, |y-y_0| \leq \frac{d}{2} \\ 0 & \text{if } |x-x_0|, |y-y_0| > \frac{d}{2} \end{cases}$$

is the distribution of the divergent forcing with $A(x) = \delta \sin(2\pi(\frac{x-x_0}{d}) + \pi)$, where $d = 2 \times 10^6 \text{ m}$ and $\delta = 1 \times 10^{-5} \text{ s}^{-1}$. The length and width of the model domain is chosen to be the circumference at 30° N ($L = 3.47 \times 10^7 \text{ m}$). This latitude is also chosen to be the center latitude of the β -plane. y varies from $-L/2$ to $L/2$, whereas x is chosen to vary from $-L/4$ to $L/3$. The model is run with 248 grid points in the x and y direction, resulting in a grid resolution of $1.4 \times 10^5 \text{ m}$, and with a time increment of 140 s. We apply a relaxation scheme at the boundaries in the y -direction following Davies (1983), whereas periodic boundary conditions are applied in the x -direction. The leap-frog scheme is used for the numerical integration in time.

We consider cases with different values of Λ for the linear and parabolic profiles with $U_0 = 0 \text{ m s}^{-1}$ and $U_0 = 10 \text{ m s}^{-1}$, respectively. The $U_0 = 0 \text{ m s}^{-1}$ and $U_0 = 10 \text{ m s}^{-1}$ studies are equivalent to the analytic solutions derived for the linear shear profile. For the parabolic shear profile we only found analytic solutions for $U_0 = 0 \text{ m s}^{-1}$. However, the numerical simulations with $U_0 = 10 \text{ m s}^{-1}$ and a parabolic profile demonstrate the more general validity of the analytic results.

2.4.1 $U_0 = 0 \text{ m s}^{-1}$

For the calculations without a constant zonal flow we shifted the forcing away from the center ($x_0 = 0 \text{ m}$, $y_0 = 5 \times 10^6 \text{ m}$) in order to situate the divergence in an area with significant basic state flow. Fig. 2.4 shows the results for the linear profile with $\Lambda = 10^{-6}/10^{-5} \text{ s}^{-1}$ in the top and bottom panel, respectively. For larger Λ there is less penetration into the positive y -direction from the forcing. Furthermore there is a collapse of meridional wave number to infinity as the perturbation reaches the origin of the y -axis yielding more elongated structures near the $y = 0$ line. The features depicted above can be directly linked to the analytic findings presented in Fig. 2.1. In order to pinpoint the sensitivity to the increased shear we can calculate $\kappa k \approx 10^{-6}$ for $\Lambda = 10^{-5}$ and $\kappa k \approx 10^{-5}$ for $\Lambda = 10^{-6}$. Hence for the same k we have values for κ being ten times larger for the case with smaller Λ resulting in enhanced ability of meridional propagation. The increase in the meridional wave number for $y \rightarrow 0$ is also evident in (2.9) where the first term in the brackets becomes infinite for $U_0 = 0$.

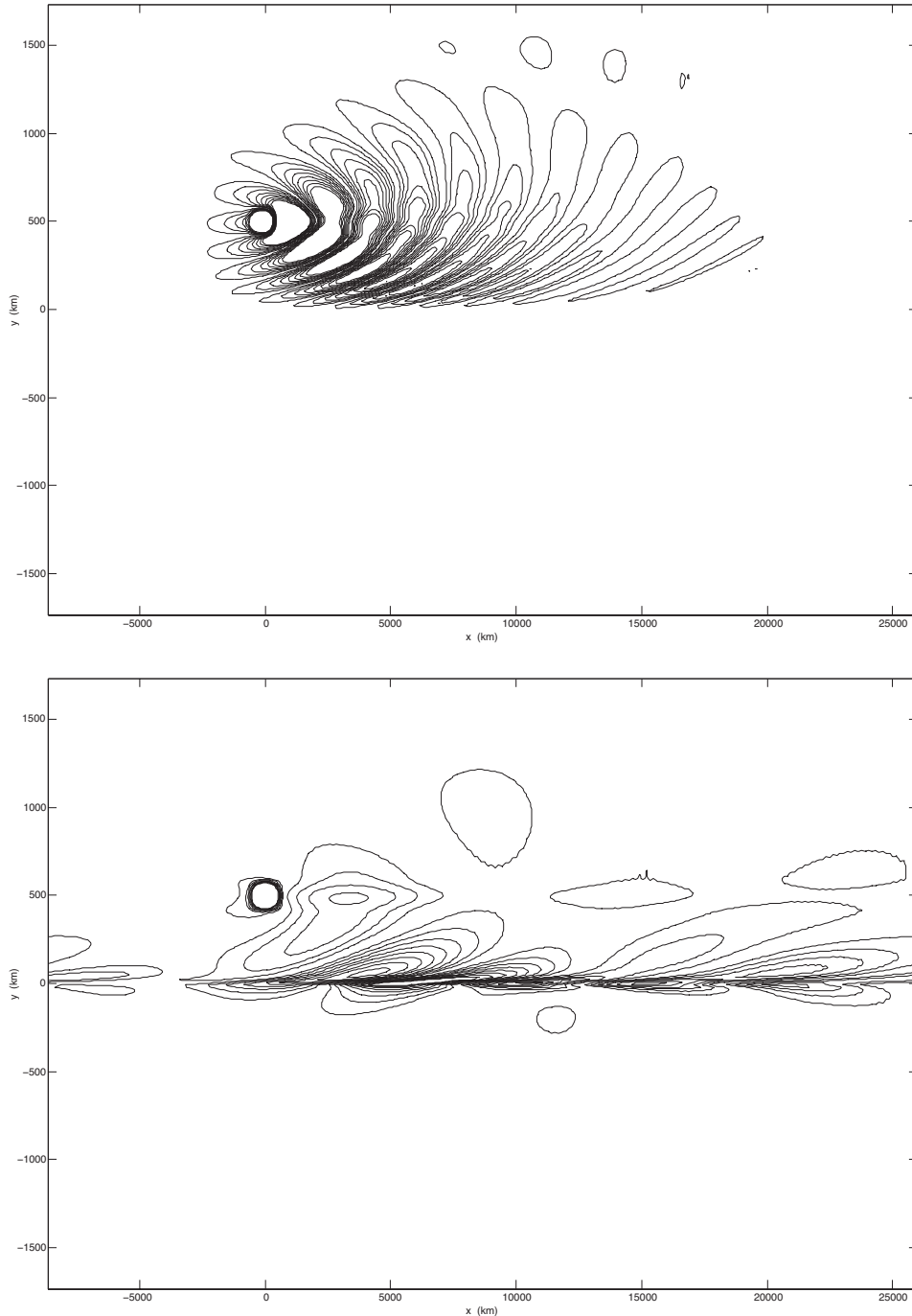


Figure 2.4: *Perturbation vorticity for the linear profile $\bar{u} = \Lambda y$ for $\Lambda = 10^{-6} \text{ s}^{-1}$ (top panel) and $\Lambda = 10^{-5} \text{ s}^{-1}$ (bottom panel). The x and y axis are in km, where the origin of x and y is at 1/4 and in the center of the domain, respectively. Solid (dashed) lines indicate positive (negative) vorticity.*

Fig. 2.5 shows the results for the parabolic profile with $\Lambda = 10^{-13}/10^{-12} \text{ m}^{-1} \text{ s}^{-1}$ in the top and bottom panel, respectively. In principal the same features of wave propagation are evident as for the linear case, i.e. decreased reach of the perturbation in the positive y -direction from the forcing for larger values of Λ and the collapse of the meridional wave number as the perturbation propagates towards $y = 0$. To link these numerical simulations to the analytic solution we can calculate the corresponding values of $\mathfrak{S}(v) \approx 4.3$ for $\Lambda = 10^{-12}$ and $\mathfrak{S}(v) \approx 14$ for $\Lambda = 10^{-13}$. For these values of v Fig. 2.3 shows enhanced propagability for the setup with reduced shear. Again, the increase of the meridional wave number of the

perturbations when approaching the $y = 0$ can be linked to (2.15) where the second term in the brackets becomes positively infinite for $y \rightarrow 0$ yielding an increase in the meridional wave number.

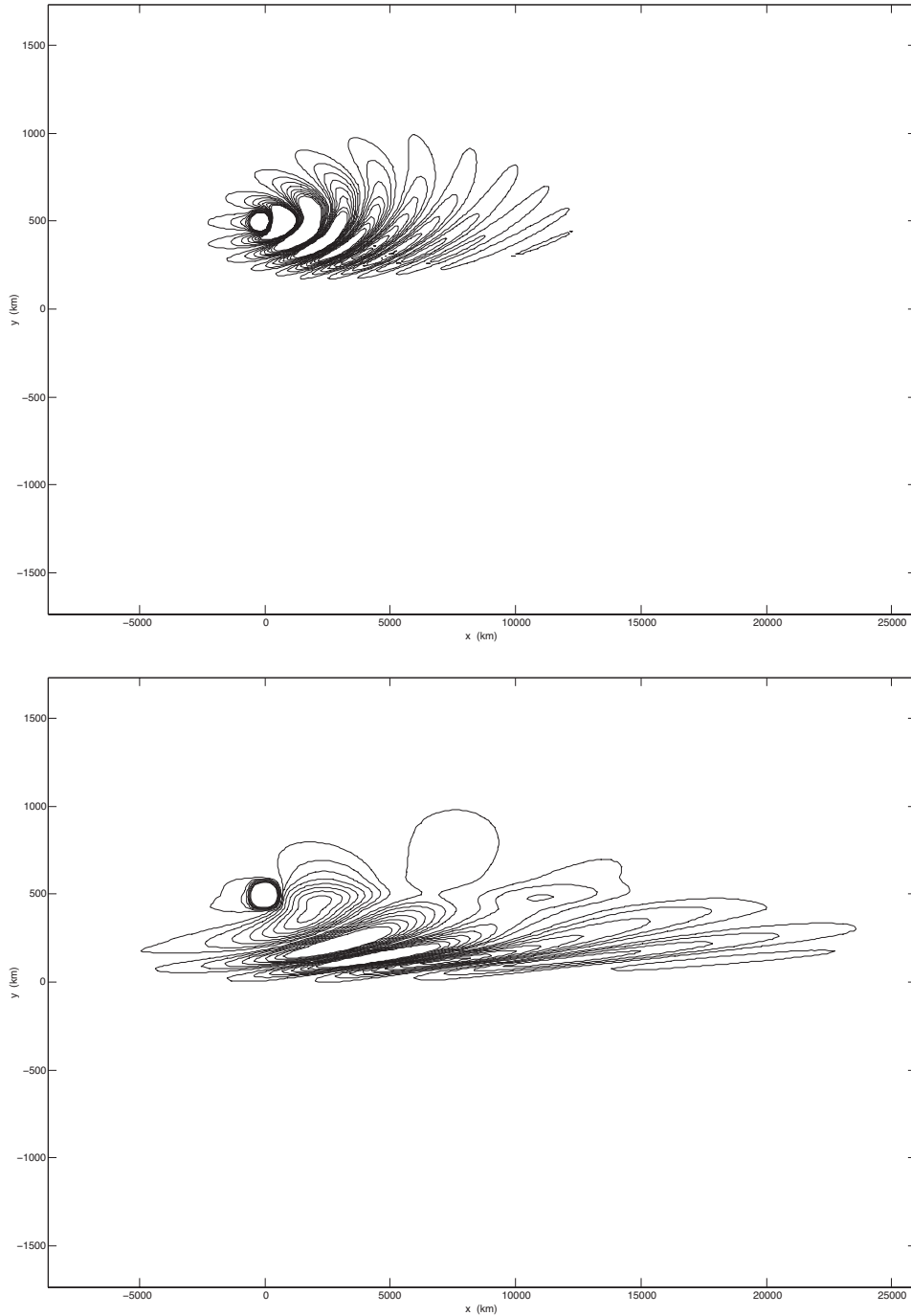


Figure 2.5: Perturbation vorticity for the parabolic profile $\bar{u} = \Lambda y^2$ for $\Lambda = 10^{-13} \text{ m}^{-1} \text{ s}^{-1}$ (top panel) and $\Lambda = 10^{-12} \text{ m}^{-1} \text{ s}^{-1}$ (bottom panel). The x and y axis are in km, where the origin of x and y is at $1/4$ and in the center of the domain, respectively. Solid (dashed) lines indicate positive (negative) vorticity.

2.4.2 $U_0 = 10 \text{ m s}^{-1}$

Fig. 2.6 shows the response to the forcing (situated at $x_0 = 0$ and $y_0 = 0$) for $U_0 = 10 \text{ m s}^{-1}$ with $\Lambda = 0$, i.e. no background shear. Downstream development (positive x -direction) of stationary Rossby waves is evident with symmetric dispersion in the positive and negative y -direction. The reach of the wave perturbation is solely determined by the damping term in (2.18). The meridional component of the group velocity is not changing along the wave train, thus the wave is not refracted. The constancy of the group velocity vector is determined through the constancy of the meridional wave number ($l = \sqrt{\frac{\beta}{U_0} - k^2}$) for a given zonal wave number k and $\beta = \text{const}$ and $U_0 = \text{const}$.

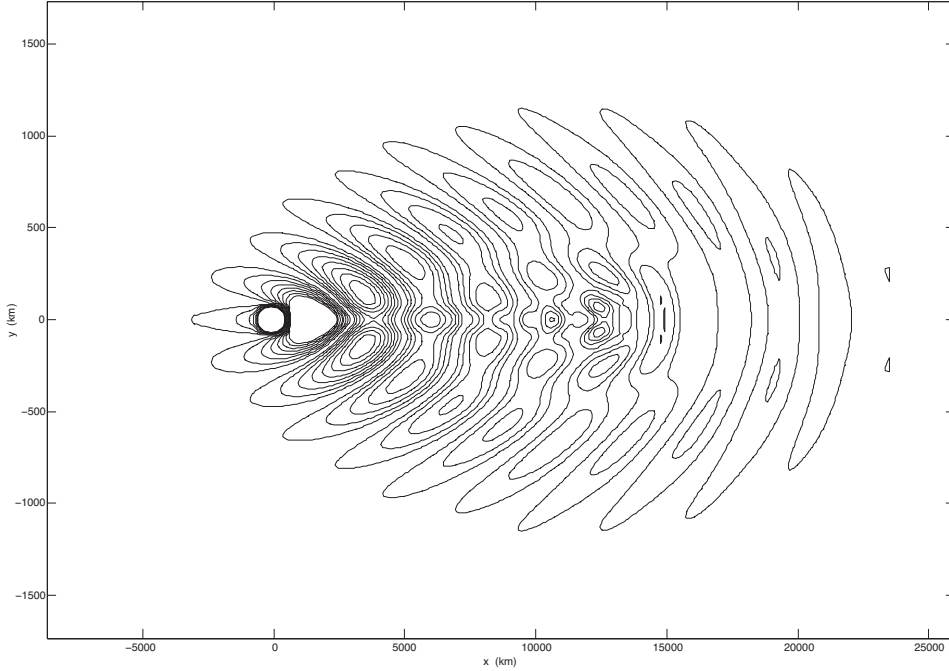


Figure 2.6: Perturbation vorticity for the constant zonal basic state profile $\bar{u} = U_0$ for $U_0 = 10 \text{ m s}^{-1}$. The x and y axis are in km, where the origin of x and y is at $1/4$ and in the center of the domain, respectively. Solid (dashed) lines indicate positive (negative) vorticity.

Figs. 2.7a/b show the results for the linear shear profile with $\Lambda = 10^{-6}/10^{-5} \text{ s}^{-1}$, respectively. Comparing these results to the results with no shear (Fig. 2.6) a reduced reach of the perturbation in the y -direction is clearly evident for increasing values of Λ as well as an increase in zonal wave length of the perturbations with greater distance from the origin of the y -axis. The response in Fig. 2.7a exhibits a propagating nature in the y -direction up to a certain value of y , whereas the response in Fig. 2.7b, where Λ is increased by a factor of ten, does not show a wave-like structure in the y -direction anymore. The perturbation is basically trapped to the origin of the y -axis in the latter case. The numerical results can be linked to the analytic findings by inferring a zonal wave number from Fig. 2.7. The dominant wave number near the center of the domain in Fig. 2.7a fits seven wave-lengths into the channel corresponding to $k \approx 1.27 \times 10^{-6} \text{ m}^{-1}$. We can also calculate $\frac{\gamma U_0}{\Lambda} \approx 25.4$ and $\kappa \approx 7.7$ for $\Lambda = 10^{-6} \text{ s}^{-1}$ to infer propagability from Fig. 2.1. The phase diagram basically indicates very weak propagability for this wave number. However the response further away from $y = 0$ is characterized by a lower zonal wave number. $k \approx 9.05 \times 10^{-7} \text{ m}^{-1}$ complies with a perturbation fitting 5 wave-length into the channel yielding $\frac{\gamma U_0}{\Lambda} \approx 18.1$ and $\kappa \approx 10.9$ for $\Lambda = 10^{-6} \text{ s}^{-1}$. For the latter parameters Fig. 2.1 predicts propagation for a significant distance in the y -direction. The trapped response in Fig. 2.7b can be linked to Fig. 2.1 by inferring $k \approx 1.09 \times 10^{-6} \text{ m}^{-1}$ (assuming a perturbation fitting 6 wave-lengths into the channel),

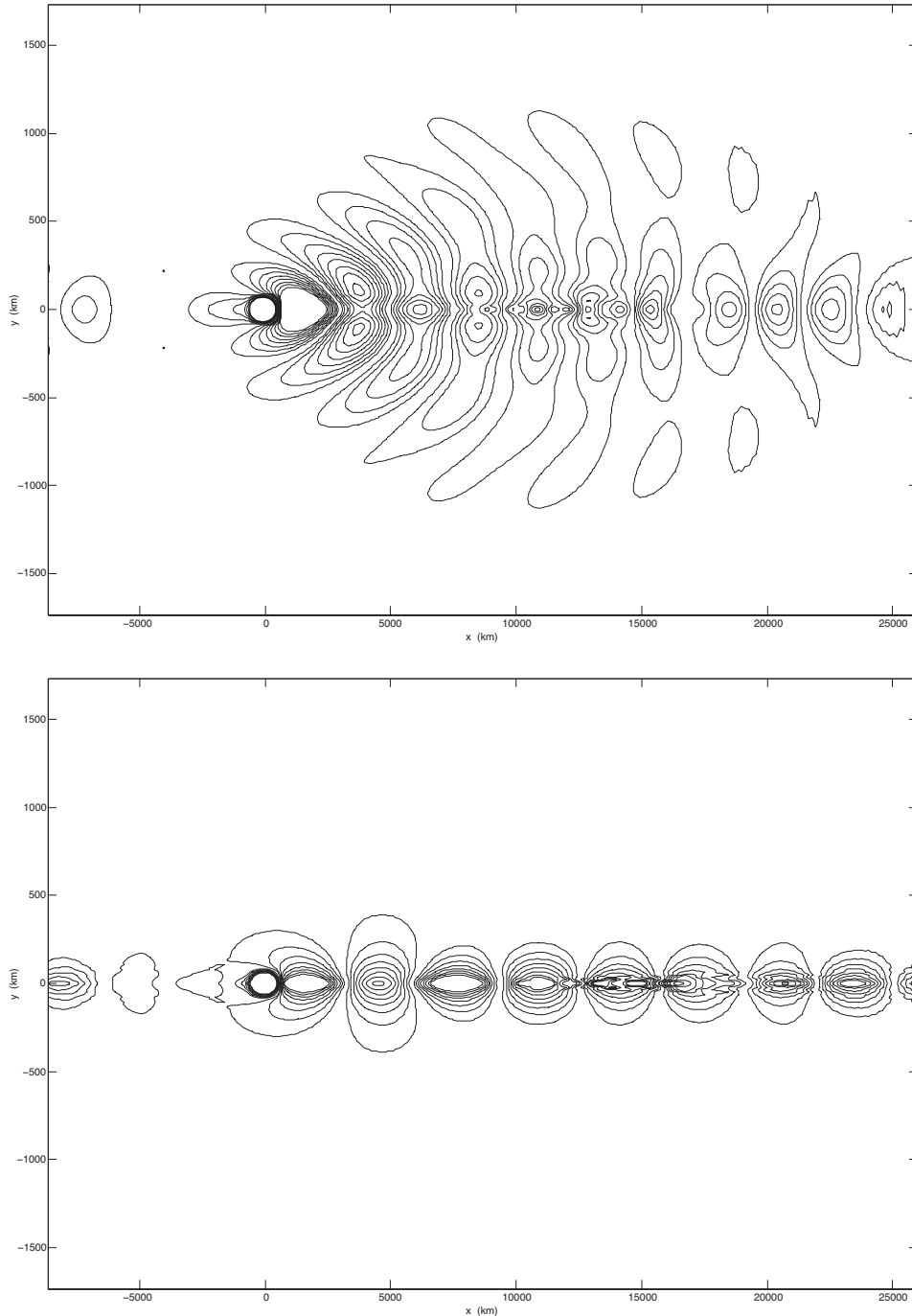


Figure 2.7: Perturbation vorticity for the linear profile $\bar{u} = U_0 + \Lambda y$ for $\Lambda = 10^{-6} \text{ s}^{-1}$ (top panel) and $\Lambda = 10^{-5} \text{ s}^{-1}$ (bottom panel). The x and y axis are in km, where the origin of x and y is at $1/4$ and in the center of the domain, respectively. Solid (dashed) lines indicate positive (negative) vorticity.

$\frac{\gamma U_0}{\Lambda} \approx 2.2$ and $\kappa \approx 0.9$ for $\Lambda = 10^{-5} \text{ s}^{-1}$, where the phase diagram depicts no propagation.

Figs. 2.8a/b show the results for the parabolic zonal basic state profiles with $\Lambda = 10^{-13}/10^{-12} \text{ m}^{-1} \text{ s}^{-1}$, respectively. Again the meridional reach of the perturbation is strongly linked to the value of Λ , i.e. for larger Λ there is less propagation in the y -direction. The response in Fig. 2.8a still shows characteristics similar to Fig. 2.6 (constant background flow) but features a decrease in zonal wave number with increasing distance from the origin of the y -axis, whereas the response in Fig. 2.8b exhibits

a much more trapped nature similar to Fig. 2.7b. To link these experiments to our analytic findings we can again utilize the results displayed in Fig. 2.3 with $\Im(v) \approx 4.3$ and $\Im(v) \approx 14$ for $\Lambda = 10^{-12} \text{ m}^{-1} \text{ s}^{-1}$ and $\Lambda = 10^{-13} \text{ m}^{-1} \text{ s}^{-1}$, respectively, suggesting a significant increase in meridional propagation for the lower value for Λ . However, from Fig. 2.3 we would still expect Rossby wave propagation for $\Lambda = 10^{-12} \text{ m}^{-1} \text{ s}^{-1}$ which is depicted in Fig. 2.8b near the forcing where the response resembles wave characteristics in the y -direction.

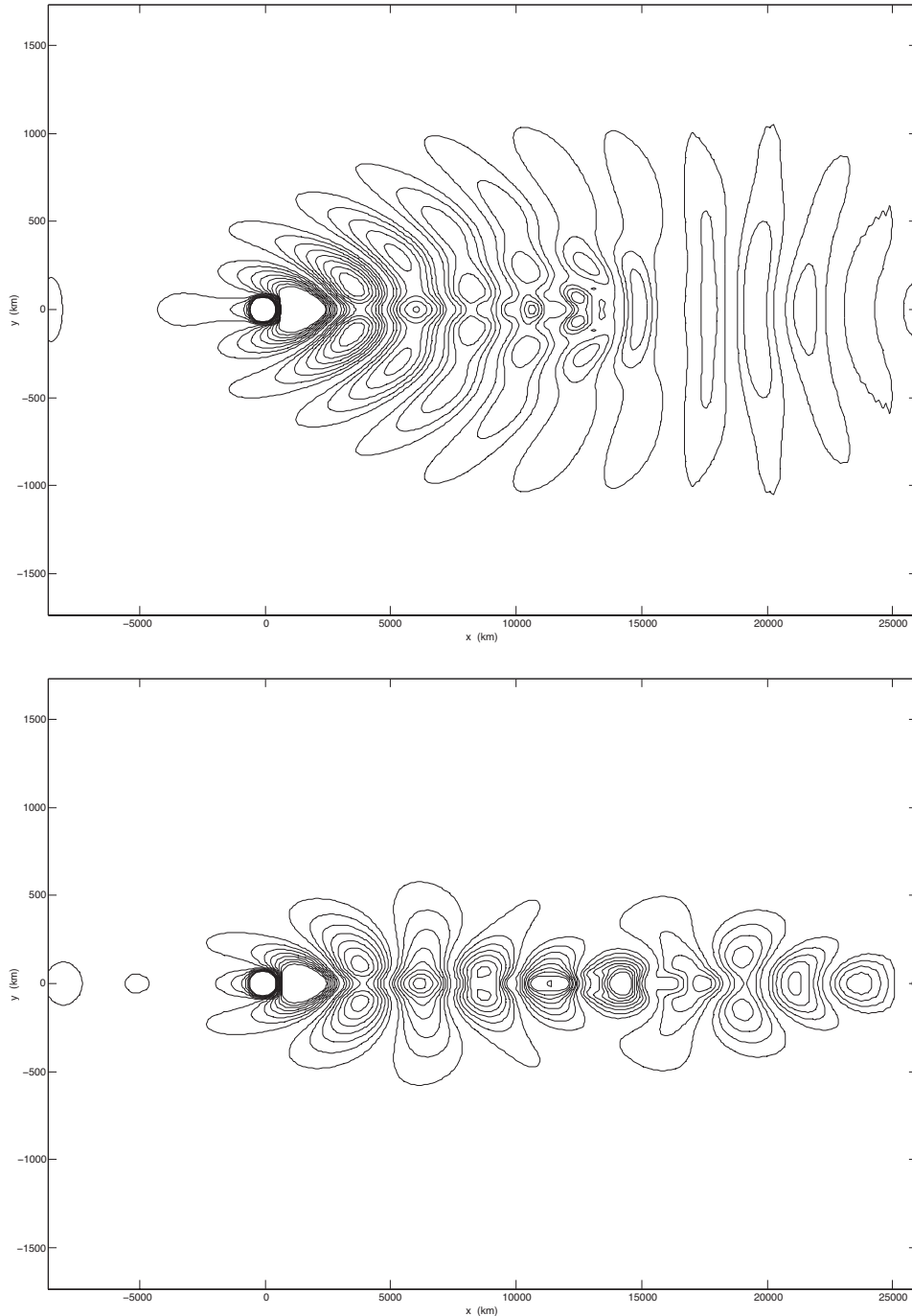


Figure 2.8: Perturbation vorticity for the parabolic profile $\bar{u} = U_0 + \Lambda y^2$ ($U_0 = 10 \text{ m s}^{-1}$) for $\Lambda = 10^{-13} \text{ m}^{-1} \text{ s}^{-1}$ (top panel) and $\Lambda = 10^{-12} \text{ m}^{-1} \text{ s}^{-1}$ (bottom panel). The x and y axis are in km, where the origin of x and y is at $1/4$ and in the center of the domain, respectively. Solid (dashed) lines indicate positive (negative) vorticity.

2.5 Basic state zonal flow only varying in z direction

The properties of vertical stationary Rossby wave propagation through linear ($\bar{u} = \Lambda z + U_0$) and parabolic ($\bar{u} = \Lambda z^2$) zonal basic state profiles are derived for the stratified QG system. For both profiles (linear and parabolic) we assume wave-like behavior in the x and y direction (i.e. $\Phi = \chi(z)e^{i(kx+ly)}$). The focus is a priori on stationary waves, i.e. $c = 0$.

2.5.1 $\bar{u} = \Lambda z + U_0$, $\Lambda > 0$

From (2.8) we obtain a 2nd order differential equation for χ .

$$\chi_{zz} + \left[\left(\frac{\frac{N^2}{f_0^2} \beta + \frac{\Lambda}{H}}{\Lambda z + U_0} \right) - \left(\frac{N^2}{f_0^2} (k^2 + l^2) + \frac{1}{4H^2} \right) \right] \chi = 0 \quad (2.19)$$

Again we end up with wave-type solutions if the value within the brackets is positive, i.e. the first term in the brackets has to be large enough. Thus propagability is increased for smaller zonal and meridional wave numbers, k and l , and for reduced shear (smaller Λ). As for linear QG theory for a constant background flow there is also a critical \bar{u} above which vertical wave propagation is prohibited (e.g. Charney and Drazin, 1961). The compressibility assumption yielding the term $\frac{1}{4H^2}$ tends to reduce propagability, too.

In order to solve (2.19) we define

$$\kappa = \frac{\frac{N^2 \beta}{f_0^2 \Lambda} + \frac{1}{H}}{\sqrt{4(k^2 + l^2) \frac{N^2}{f_0^2} + \frac{1}{H^2}}} \quad (2.20)$$

$$\nu = \frac{1}{2} \quad (2.21)$$

$$\gamma = \sqrt{4(k^2 + l^2) \frac{N^2}{f_0^2} + \frac{1}{H^2}} \quad (2.22)$$

and end up with solutions for χ in the form of (see pp 504 Abramowitz and Stegun, 1964)

$$\chi(z) = \Re \left\{ C_1 M_{\kappa, \nu} \left(\gamma z + \frac{\gamma U_0}{\Lambda} \right) + C_2 W_{\kappa, \nu} \left(\gamma z + \frac{\gamma U_0}{\Lambda} \right) \right\} \quad (2.23)$$

where $C_{1/2}$ are constants and $M_{\kappa, \nu}$ and $W_{\kappa, \nu}$ are the Whittaker functions of the first and second kind, respectively. The solution is very similar to its horizontal counterpart with linear shear. Analogous to the discussion above the vertical scaling parameter γ illustrates the sensitivity of wave propagation to the horizontal wave numbers. κ is basically the ratio of the first and the second term in the brackets. For $\kappa \ni \mathbb{N}$, $M_{\kappa, \nu}$ has only unbound solutions for $z \rightarrow \infty$. Thus we first focus on the contribution from $W_{\kappa, \nu}$ which takes the form of a purely decaying function for $\kappa < 1$, whereas for $\kappa \geq 1$ the solution becomes wave like up to a certain value of γz . The results for the basic state with a linear varying profile in the z -direction are shown in Fig. 2.1, where the abscissa and ordinate are γz and κ , respectively. The grey

shading indicates negative values. Bearing in mind that κ decreases for increasing Λ it is evident that the ability of wave propagation is reduced for stronger shear.

If the boundary condition $\chi(y = -\frac{U_0}{\Lambda}) = 0$ is requested, $M_{\kappa, \nu}$ has trapped modal solutions for $\kappa = 1, 2, 3, \dots$, which are shown for the first three modes in Fig 2.2 where the abscissa is chosen to be γz . We can solve (2.20) for the resonant total wave number $K = \sqrt{k^2 + l^2}$ yielding

$$K = \frac{f}{4N} \sqrt{\left(\frac{\frac{N^2 \beta}{f_0^2 \Lambda} + \frac{1}{H}}{\kappa} \right)^2 - \frac{1}{H^2}} \quad (2.24)$$

For $N = 0.01 \text{ s}^{-1}$, $f_0(45^\circ)$, $\beta(45^\circ)$, $H = 7000 \text{ m}$ and $\Lambda = 10^{-3} \text{ s}^{-1}$ we obtain

$$K(\kappa = 1) = 6.65 \times 10^{-7}; k(\kappa = 1) = 2.12 \quad (2.25)$$

$$K(\kappa = 2) = 9.60 \times 10^{-8}; k(\kappa = 2) = 0.31 \quad (2.26)$$

$$K(\kappa = 3) = 2.66 \times 10^7 i; k(\kappa = 3) = 0.85 i \quad (2.27)$$

where we assumed $k = l$ for simplicity to calculate the zonal wave number with respect to the circumference of the earth at 45° (the corresponding value of k for $l = 0$ is $\sqrt{2}k$). All K are imaginary for $\kappa \geq 3$ for the chosen background and basic state parameters indicating a decaying solution in the horizontal.

2.5.2 $\bar{u} = \Lambda z^2$, $\Lambda > 0$

From (2.8) we obtain a 2nd order differential equation for χ .

$$\chi_{zz} + \left[\left(\frac{N^2 \beta}{f_0^2 \Lambda} - 2 \right) z^{-2} + \frac{2}{H} z^{-1} - \left(\frac{N^2}{f_0^2} (k^2 + l^2) + \frac{1}{4H^2} \right) \right] \chi = 0 \quad (2.28)$$

(2.28) is again a second order differential equation featuring wave-like solutions if the value within the brackets in front of χ is greater than zero. The first two terms in the brackets become smaller for increasing z always yielding a level where the sum of the three terms alters its sign. Like for all other solutions presented within this study the propagability is reduced for higher horizontal wave numbers and for increasing shear. Like for the linear vertical shear profile the compressibility assumption tends to reduce propagability as well.

Defining

$$\kappa = \frac{2}{H \sqrt{4(k^2 + l^2) \frac{N^2}{f_0^2} + \frac{1}{H^2}}} \quad (2.29)$$

$$\nu = \frac{1}{2} \sqrt{9 - 4 \frac{N^2 \beta}{f_0^2 \Lambda}} \quad (2.30)$$

$$\gamma = \sqrt{4(k^2 + l^2) \frac{N^2}{f_0^2} + \frac{1}{H^2}} \quad (2.31)$$

we end up with solutions for χ in the form of (see pp 504 Abramowitz and Stegun, 1964)

$$\chi(z) = \Re \{C_1 M_{\kappa, \nu}(\gamma z) + C_2 W_{\kappa, \nu}(\gamma z)\} \quad (2.32)$$

where $C_{1/2}$ are constants and $M_{\kappa, \nu}$ and $W_{\kappa, \nu}$ are the Whittaker functions of the first and second kind, respectively. The γ again illustrates the sensitivity of wave propagation to the horizontal wave numbers. κ is basically the ratio of the second (z^{-1}) and the third term in the brackets. It is important to note that κ does not include the shear parameter. The sensitivity of the response to shear is only present in ν , which depicts the importance of the first term in the brackets (z^{-2}) and becomes imaginary if Λ is large enough. For $\kappa \ni \mathbb{N}$, $M_{\kappa, \nu}$ has only unbound solutions for $z \rightarrow \infty$. The principal behavior of $W_{\kappa, \nu}$ was already discussed above for the linear profile.

The results for $\kappa = 0.75$ are shown in Fig. 2.9, where we restricted ν to be imaginary only. For $\nu \in \mathbb{R}$ the corresponding $W_{\kappa, \nu}$ is decaying rapidly with z . Changing κ in a meaningful range does not significantly impact on the structures presented in Fig. 2.9. The κ chosen here is based on $N = 0.01 \text{ s}^{-1}$, $H = 7000 \text{ m}$, $f_0(45^\circ)$ and $k \approx 8$. Wave-type solutions in the z -direction are evident for larger values of $\Im(\nu)$. For very small values of $\Im(\nu)$ only a decaying solution is found for χ . Bearing in mind that $\Im(\nu)$ decreases for increasing Λ it is evident that the ability of wave propagation is reduced for stronger shear.

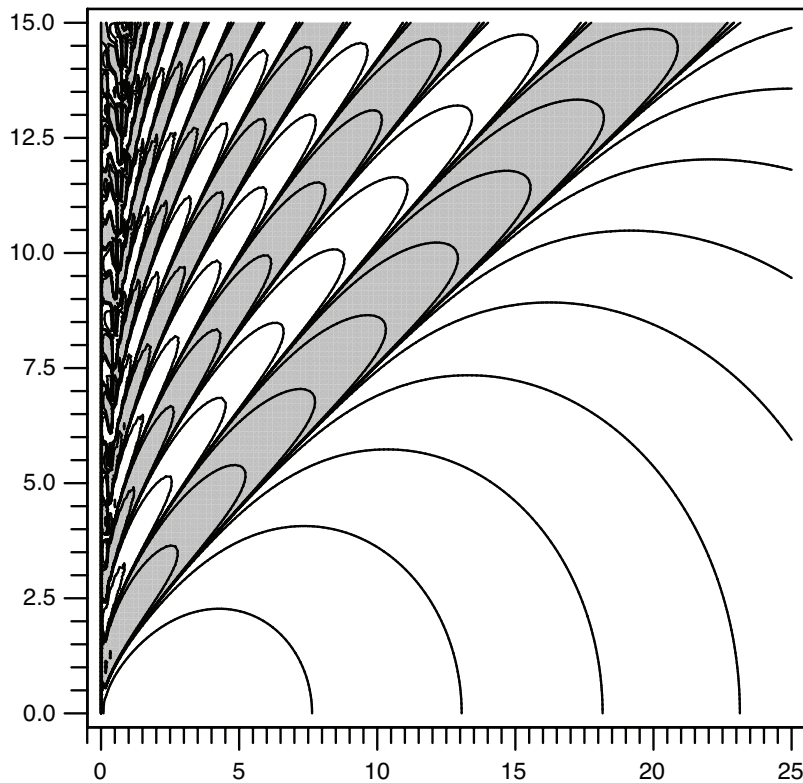


Figure 2.9: Contour plot of $W_{\kappa, \nu}(\gamma z)$. Negative values shaded. The abscissa is γz and the ordinate is κ for the parabolic vertical profile ($\bar{u} = \Lambda z^2$). Contours are drawn every $\pm 10^x$, where $x = [-10, 9, \dots, 9, 10]$.

If the boundary condition $\chi(y = -\frac{U_0}{\Lambda}) = 0$ is requested, $M_{\kappa, \nu}$ has trapped modal solutions for $\kappa = 1, 2, 3, \dots$ if $\frac{N^2 \beta}{f^2 \Lambda} = 2$. The solutions are shown for the first three modes in Fig. 2.2 where the abscissa is

chosen to be γz . We can again solve (2.20) for the resonant total wave number $K = \sqrt{k^2 + l^2}$ yielding

$$K = \frac{f}{NH} \sqrt{\frac{1}{\kappa^2} - \frac{1}{4}} \quad (2.33)$$

For $N = 0.01 \text{ s}^{-1}$, $f_0(45^\circ)$ and $H = 7000 \text{ m}$ we obtain

$$K(\kappa = 1) = 1.27 \times 10^{-6}; k(\kappa = 1) = 4.06 \quad (2.34)$$

$$K(\kappa = 2) = 0; k(\kappa = 2) = 0 \quad (2.35)$$

$$K(\kappa = 3) = 5.48 \times 10^{-7} i; k(\kappa = 3) = 1.75 i \quad (2.36)$$

where we assumed $k = l$ for simplicity to calculate the zonal wave number with respect to the circumference of the earth at 45° (the corresponding value of k for $l = 0$ is $\sqrt{2}k$). All K are imaginary for $\kappa \geq 3$ for the chosen background and basic state parameters indicating a decaying solution in the horizontal.

2.6 Discussion

We showed that the horizontal propagability of stationary Rossby waves is most sensitive to the shear parameter Λ and the parameters γ or λ for the Whittaker or Bessel function type of solutions, respectively. Whereas the solutions were found to be wave-like only for values of Λ being small enough, the reach of the perturbations is mainly determined by the scaling parameters in the y -direction (γ and λ). Thus the shear determines the type of response and the zonal and vertical structure of the perturbation (inherent in the parameters γ and λ) determines its meridional reach. We found that larger scale perturbations with smaller zonal wave numbers have an increased propagability. For the linear shear profile the structure of the perturbation actually also impacts on the parameter κ enhancing propagability through an increase of κ for smaller values of λ . Within the barotropic framework only the zonal wave number determines the reach of the perturbation, whereas for the QGSW and the stratified QG system the mean depth of the fluid and the vertical wave number impact on the reach as well. The meridional propagability is reduced if the mean depth of the shallow water system is reduced or if the vertical wave number increases. Thus the reach of Rossby waves can be significantly overestimated by a barotropic model if the perturbation exhibits a considerable vertical structure.

Our findings can be linked to the results of barotropic Rossby wave ray tracing as introduced by Hoskins and Karoly (1981) and Hoskins and Ambrizzi (1993). For the idealized profiles presented here $K_s \rightarrow \infty$ for $y \rightarrow -\frac{U_0}{\Lambda}/0$, hence all stationary Rossby waves are refracted towards the origin of the y -axis. Following Hoskins and Ambrizzi (1993) the ray path radius of curvature is $r = K_s^2 \left(k \frac{dK_s}{dy} \right)^{-1}$. With the chosen linear and parabolic profiles in this study it can be shown that $r \sim \Lambda^{-\frac{1}{2}}$. Thus the curvature yields a more rapid refraction of waves for higher values of Λ . However the strength of our results is that we can immediately infer propagability from our exact analytic solutions, i.e. for any chosen set of parameters we can deduce the structure of the response from our phase diagrams without integrating a complete ray path for each set of parameters, furthermore our solution does not rely on a WJKB approximation.

The numerical simulations in section 2.4 supplement our analytic findings in section 2.3, where the meridional reach of the waves can be directly inferred from the phase diagrams in Figs. 2.1 and 2.3 illustrating the strength of the deduced solutions.

The analytic solutions for vertical Rossby wave propagation show similar behavior compared to the horizontal, i.e. for larger values for Λ the ability of vertical wave propagation is significantly reduced.

The similarity of the solutions for the linear profiles is manifested in the possibility to display the solutions with the same figure (see Fig. 2.1). The only differences are the scaling of the abscissa and the values depicted along the ordinate. The similarity of the solutions for the parabolic profiles can easily be seen by comparing Fig. 2.3 for the horizontal with Fig. 2.9 for the vertical parabolic profile. Again the values displayed along the abscissa and ordinate are different and the range of the abscissa is chosen to vary from 0 to 25 for the vertical case, but the resemblance of the two is striking. Similar to their horizontal counterparts there is a large sensitivity of the vertical propagability to the horizontal wave numbers. For the linear and parabolic shear cases we find that $\kappa \sim \sqrt{k^2 + l^2}^{-1}$ yielding larger values of κ , hence increased propagability, for smaller zonal and meridional wave numbers. Since the scaling of the abscissa is directly proportional to $\sqrt{k^2 + l^2}$, the vertical reach of wave perturbations is enhanced for smaller wave numbers as well.

The results for the vertical propagation of Rossby waves can be seen as an extension to Charney and Drazin (1961) who were among the first to comment on the dependence of vertical propagability on the basic state flow and also investigated the linear varying vertical profile. They also identified an increase in vertical propagation for smaller wave numbers. Matsuno (1970) and Lindzen et al. (1982) applied the concepts of Charney and Drazin (1961) to realistic time mean basic states confirming that only the lowest zonal wave numbers, i.e. one and two, can significantly impact on the stratosphere. Charney and Drazin (1961) also indicated that planetary perturbations cannot propagate vertically if the stratospheric polar vortex is very strong due to a critical velocity for which vertical propagation is inhibited.

We identified a level where a critical velocity is reached within our solutions above which propagation is inhibited. This level is lifted for decreased values of the shear parameter Λ and a smaller scaling parameter λ which is proportional to the horizontal wave numbers. Thus the earlier findings are covered by our analytic solutions. In addition our results show that for perturbations approaching a strong jet from below through a parabolic or linear profile the vertical penetration of Rossby waves is significantly reduced and again only very long waves with low wave number are able to propagate. Latter finding can be related to the situation of a very strong polar night vortex. The reduced propagability in the case of a strong polar vortex has been perceived before indicating the sensitivity of stratospheric sudden warming to the state of the stratosphere. Due to the decreased propagability McIntyre (1982) suggested a preconditioning of the polar vortex where planetary waves successively deplete positive zonal momentum in the lower stratosphere enabling further vertical propagation. In their model study Scott and Polvani (2006) pinpointed the importance of preconditioning by highlighting the crucial role of the vertical structure of stratosphere on the propagability of planetary waves and hence on stratospheric sudden warmings.

The solutions also contain trapped modal solutions for all basic state profiles except for the parabolic profile in the horizontal. The trapped solutions for the horizontally varying profile within the QGSW framework have been identified before by Harlander et al. (2000). However, their set of QGSW equations is different to the one presented here due to the fact that they assumed the basic state zonal flow $\bar{u}(y)$ to be balanced by a varying mean depth of the fluid $\bar{h}(y)$. Furthermore in contrast to our derivation they utilized a WJKB approximation in their study. In our derivation we have chosen the zonal basic state to be balanced by an external pressure field acting at the free surface of \bar{h} . The approximation by Harlander et al. (2000) has a weakness for large model domains since \bar{h} can become small or even negative. First would lead to a loss of the validity of the assumptions made within the QG approximation and latter would be unphysical. In Harlander et al. (2001) the authors extended their analytic study with numerical simulations pinpointing the applicability of their earlier findings. Apart from other features they demonstrated the agreement between their theory and their model simulations by comparing the resonant zonal wave numbers, which turned out to be 8 in their model studies. They obtain a theoretical value of $k = 7.71$ with their chosen shear profile of $\Lambda = \frac{10^{-6}}{2}$, whereas for $\kappa = 2$, which corresponds to their $n = 1$ mode, we obtain $k = 8.85$. This difference in the solution is due to the discrepancy in the QGSW set of equations used and the fact that Harlander et al. (2000) used the WJKB approximation for their derivation.

2.7 Final remarks

We presented analytic solutions for horizontal stationary Rossby wave propagation through linear and parabolic zonal basic states ($\bar{u} = U_0 + \Lambda y$ or Λy^2) utilizing the barotropic, the QGSW and the stratified QG framework. These results were supplemented by numerical integrations of a linear barotropic model. In addition we also discussed analytic solutions for vertical stationary Rossby wave propagation through zonal basic states with a linear and parabolic structure in the vertical ($\bar{u} = U_0 + \Lambda z$ or $U_0 + \Lambda z^2$) for the stratified QG system.

We showed that the ability of horizontal and vertical stationary Rossby wave propagation decreases for increased linear or parabolic shear. For large values of the shear parameter Λ the propagation of Rossby waves is inhibited. It was shown that an increase in the zonal and vertical wave numbers decreases the horizontal propagability, whereas an increase in the zonal and meridional wave numbers decreases the vertical propagability. The numerical simulations performed with a linear barotropic model facilitate the analytic findings and even illustrate the more general nature of the results for cases where a constant mean flow is added to the parabolic basic state zonal flow.

Within the analytic framework we also identified several trapped modal solutions for all basic state profiles except for the parabolic profile in the horizontal ($\bar{u} = \Lambda y^2$). Albeit the academic nature of these modal solutions and their limited applicability to the real atmosphere, their existence illustrates certain issues for idealized model studies. Numerical simulations with similar basic state profiles and boundary conditions ($\Psi = 0$ at $y = 0$ or $z = 0$) can be significantly contaminated by these resonant modes, which might hamper the interpretation of the results.

Chapter 3

Extra-tropical response to sub-tropical Forcing: Global simulations with an idealized jet

3.1 Introduction

Stationary planetary waves constitute a large fraction of the zonal asymmetry of the climatological mean state of the atmosphere. Held et al. (2002) reviewed the theory and modeling of these stationary waves. Studies ranging from stationary quasi-geostrophic (QG) linear theory to the integrations of the primitive equations on the sphere aimed to highlight the relative contributions of orographic and diabatic forcings to the composition of the asymmetry (Charney and Eliassen, 1949; Smagorinsky, 1953; Egger, 1976a,b; Webster, 1972; Hoskins and Karoly, 1981; Simmons, 1982; Valdes and Hoskins, 1989; Ting, 1994; Wang and Ting, 1999).

The identification of global teleconnection patterns (e.g. Pacific North American (PNA)) (Wallace and Gutzler, 1981; Horel and Wallace, 1981) suggested a dynamical linkage of distant regions on the globe. Hoskins et al. (1977) and Hoskins and Karoly (1981) demonstrated that rays of non-divergent barotropic stationary Rossby waves on the sphere resemble paths along great circles similar to the pattern of the PNA indicating that the dynamics of teleconnections might be linked to stationary Rossby waves emerging from the tropical Pacific. Henceforth stationary linear shallow water (Lim and Chang, 1983) or barotropic (Branstator, 1985; Sardeshmukh and Hoskins, 1988; Hoskins and Ambrizzi, 1993) models were used to pinpoint the dynamical linkage of the PNA to tropical forcing. The studies mainly comprise a steady-state approach linearized about the winter mean state of the atmosphere. Global stationary baroclinic studies linearized about the same basic state basically support the barotropic findings (Ting and Sardeshmukh, 1993; Ting and Yu, 1998).

Some studies considered a normal mode instability maintained by a fixed forcing as an alternative cause for the existence of the PNA (e.g. Simmons et al., 1983; Frederiksen and Webster, 1988). However, it was shown that small changes in the damping or in the forcing eliminate the instability (Borges and Sardeshmukh, 1995; Ting and Sardeshmukh, 1993; Ting and Yu, 1998) casting doubt on the proposed mechanism.

The studies listed above are all limited to the scope of linearity and the assumption of steady-state. Jin and Hoskins (1995) were among the first to investigate the time evolution of the response to a tropical forcing in a baroclinic model linearized about the climatological winter mean state. Within the first 20 days they identified a similar barotropic response compared to earlier studies before baroclinic instability dominates their linear integration from day 20 onwards.

In the study presented here we go beyond linearity. We investigate the non-linear evolution in time and space of stationary Rossby wave patterns in a three dimensional global model. We designed an initial state of the atmosphere with a zonally symmetric barotropic jet in each hemisphere and analyze the response forced by a single mountain located alternatively in the tropical or subtropical latitudes on an otherwise flat planet. The key interests are the sensitivities of the response to the latitude of the forcing and to the strength of the jet. The idealized nature of the setup helps to shed light on the dynamical features of wave propagation based upon adopting barotropic and QG Rossby wave theory.

Our initial setup features a critical latitude for stationary Rossby waves at the equator. Linear stationary theory would prohibit the transmission of stationary Rossby waves from one hemisphere into the other since the meridional group velocity becomes zero and the response collapses to very small and

very elongated structures in the meridional and zonal directions, respectively. Some theories predict the energy to be trapped along the equator, possibly yielding wave breaking (Dickinson, 1968, 1970) or reflection at the critical latitude (Killworth and McIntyre, 1985; Brunet and Haynes, 1996). However, our non-linear results show that non-stationary Rossby waves are in fact transmitted from one hemisphere into the other despite the stationary character of the forcing in our simulations.

In section 3.2 we introduce the model used for this study followed by the description of the initial conditions and a short recapitulation on the concepts of ray tracing. A brief discussion of three dimensional linear QG Rossby wave dispersion is presented in section 3.3. Our results are presented in section 3.4 where we also introduce our method of wave detection. In section 3.5 we discuss our results in the context of Rossby wave propagation theory. Our final remarks are given in section 3.6.

3.2 Experiment setup

3.2.1 Model

We utilize the CY31R2 version of the Integrated Forecast System (IFS) from the European Centre for Medium Range Weather Forecasts (ECMWF) (see ECMWF (2007) and references therein). In a nutshell the IFS is a hydrostatic, primitive equation, global spectral model with hybrid levels ($0 \leq \eta \leq 1$) in the vertical (Simmons and Burridge, 1981). It employs a semi-Lagrangian semi-implicit time-stepping scheme and was developed for operational forecasts at ECMWF.

Our experiments are performed with a stripped-down version of the model (i.e. dynamical core), basically constituting an adiabatic version of the full code. Hence all physical parameterizations (radiation, condensation, convection, boundary layer processes etc.) are switched off. The rationale for this is to facilitate the interpretation by separating the complex nature of diabatic processes hence elucidating the purely dynamical response.

We integrate the model for a time span of 100 days with 60 levels in the vertical using a triangular truncation T159, which roughly corresponds to a 125 km grid spacing. The time increment was set to 3600 or 1800 seconds (see below).

The boundary condition for the hybrid level vertical velocity is $\dot{\eta} = 0$ at the bottom ($\eta = 1$) and at the top ($\eta = 0$) of the model domain. The condition at $\eta = 0$ would allow for reflection of gravity waves from the lid. The impact of this unphysical reflection is minimized in the IFS by increasing the horizontal diffusion in the uppermost model levels linearly with $\log(p)$.

3.2.2 Initial conditions

The initial fields of the experiment are designed to pinpoint the dynamical behavior of the propagation of Rossby waves through an idealized background state which comprises a barotropic zonal jet in each hemisphere. A single circular mountain acts as a wave source on an otherwise flat planet. The zonal wind profile is geostrophically balanced in an isothermal atmosphere (288 K) yielding a constant stratification of $N \approx 0.018 \text{ s}^{-1}$.

In order to minimize the effects of barotropic instability on the simulations it is desirable to design a jet profile with an absolute vorticity gradient greater than zero everywhere. If the absolute vorticity gradient changes sign somewhere the necessary condition for barotropic instability is fulfilled (Drazin et al., 1982). We found a zonal wind profile on the sphere

$$U(\Phi) = U_0 |\Phi|^\kappa \exp^{-\gamma|\Phi|} \cos \Phi \quad (3.1)$$

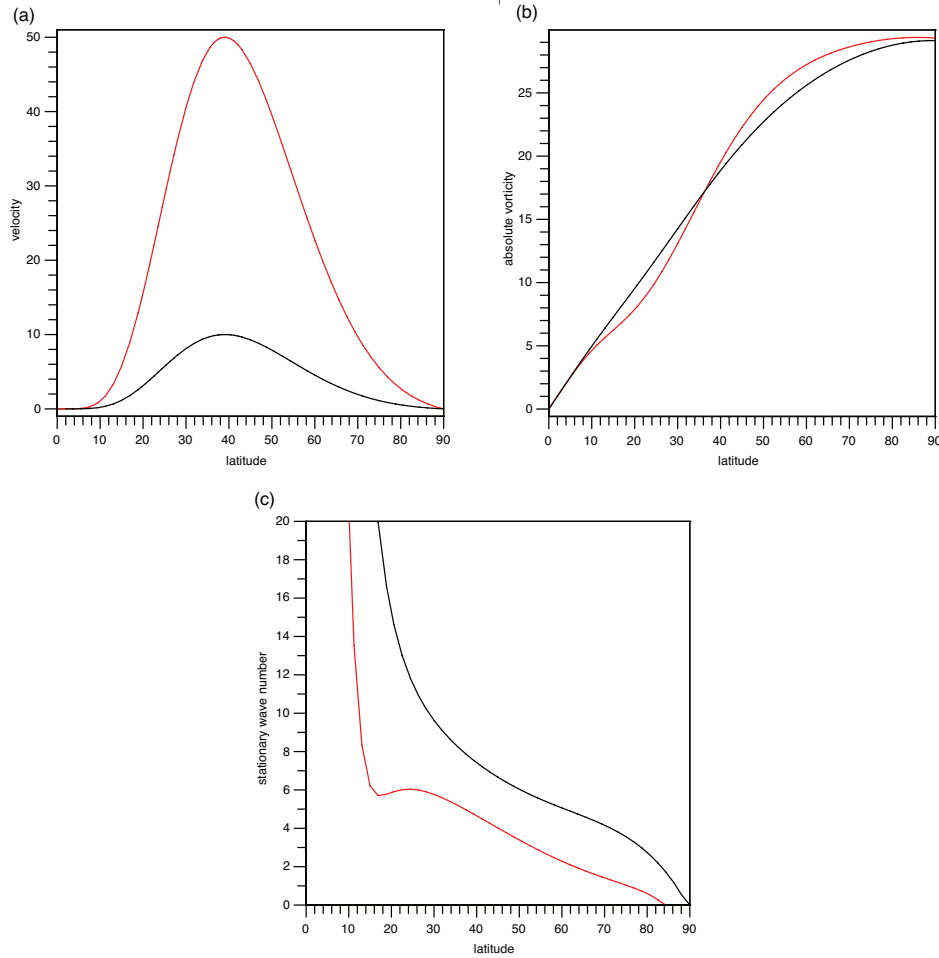


Figure 3.1: Zonal wind speed [$m s^{-1}$] (a), absolute vorticity [$\times 10^{-5} s^{-1}$] (b) and stationary wave number K_s (b) as a function of latitude for the setup with a maximum jet speed of $50 m s^{-1}$ (red) and $10 m s^{-1}$ (black).

which yields barotropic stability everywhere, except at very high latitudes (i.e. $|\Phi| > 85^\circ$) for very large maximum jet speeds ($\max(U) \geq 40 m s^{-1}$). U_0 is a constant defining the maximum wind speed, Φ is the latitude and κ and γ determine the shape of the jet profile. For our setup we have chosen $\kappa = 6$ and $\gamma = 8$, yielding a jet maximum at around 39° N/S. We will present results for experiments with five different maximum jet speeds, i.e. 10, 20, 25, 30, 40 and $50 m s^{-1}$. All simulations were performed with a time increment of $dt = 3600 s$ except for maximum jet speeds of 40 and $50 m s^{-1}$ where we set $dt = 1800 s$ in order to maintain numerical stability.

Our wave source, the circular mountain, is specified by

$$h(\lambda, \Phi) = \begin{cases} h_0 \cos^2\left(\frac{\pi r(\lambda, \Phi)}{2R}\right) & \text{if } r(\lambda, \Phi) \leq R \\ 0 & \text{if } r(\lambda, \Phi) > R \end{cases}$$

where λ is the longitude, h_0 is the maximum mountain height, $R = a/3$ corresponds to a third of the radius of the earth a and $r(\lambda, \Phi)$ is the great circle distance from the center of the mountain. Thus the dimensions of our orographic forcing are similar to the dimensions of the thermal forcing used in Jin and Hoskins (1995) and Ting and Yu (1998). The longitudinal position of the mountain is identical for all experiments, i.e. 180° W, whereas the center latitude is set to 0° , 10° , 20° or 30° N. The standard

mountain height was chosen to be $h_0 = 2000$ m. The sensitivity of the results to these standard settings will be discussed in section 3.5.1

Fig. 3.1 shows the velocity profiles for two selected jet profiles with a maximum wind speed of 10 and 50 m s^{-1} . Also shown is the absolute vorticity and the stationary wave number for each jet profile. The stationary wave number determines the refraction of the waves along their ray paths (Hoskins and Karoly, 1981; Karoly, 1983; Hoskins and Ambrizzi, 1993). Since we will refer to the concepts of ray tracing of non-divergent barotropic Rossby waves in the discussion it is worthwhile to briefly outline some of the key features.

3.2.3 Stationary wave number/Ray tracing

The basic idea is that stationary waves disperse along their local group velocity vector where the dispersion relation for barotropic Rossby waves (Rossby, 1939) is used to derive the group velocities. Due to the complex nature of the equations of motion on the sphere Hoskins and Karoly (1981) utilized the Mercator projection to simplify the set of equations. They furthermore applied the WKB approximation to investigate wave propagation on a slowly varying background flow. We basically follow their derivation but use a slightly different version of the meridional derivative to account for the sphericity of the earth. Where

$$\omega = Um - \frac{\beta^*}{K^2}m \quad (3.2)$$

$$\beta^* = \frac{\partial}{a\partial\Phi} \left(f - \frac{1}{\cos(\Phi)} \frac{\partial(U\cos(\Phi))}{a\partial\Phi} \right) \quad (3.3)$$

$$K = \sqrt{m^2 + l^2} \quad (3.4)$$

$$f = 2\Omega \sin(\Phi) \quad (3.5)$$

is the dispersion relation used in our study with β^* being the absolute vorticity gradient on the sphere. ω is the frequency of the wave, a is the radius of the earth, U is the background flow, f is the Coriolis parameter, $\Omega = \frac{2\pi}{86400} \text{ s}^{-1}$ and m and l are the zonal and meridional wave numbers, respectively. Thus the stationary wave number becomes $K_s = \sqrt{\frac{\beta^*}{U}}$.

We can now use (3.2) yielding

$$C_{gx} = \frac{\partial\omega}{\partial m} = U + \frac{m^2 - l^2}{K^4} \beta^* \quad (3.6)$$

$$C_{gy} = \frac{\partial\omega}{\partial l} = \frac{2kl}{K^4} \beta^* \quad (3.7)$$

where C_{gx} and C_{gy} are the zonal and meridional group velocities. The concept of ray tracing assumes

$$\frac{dx}{dt} = C_{gx}; \frac{dy}{dt} = C_{gy} \rightarrow \frac{dy}{dx} = \frac{l}{m \left(1 + \frac{cK^4}{2\beta^*m^2} \right)} \quad (3.8)$$

to obtain the ray paths of the Rossby waves where m turns out to be constant along the ray (due to the WKB approximation) and l is varying along the paths according to

$$l = \pm \sqrt{\frac{\beta^*}{U-c} - m^2} \quad (3.9)$$

where $c = \frac{\omega}{m}$ is the phase speed of the wave, which is usually set to zero for the investigation of stationary wave propagation. From (3.9) we have propagation in the lateral direction for $l \in \mathbb{R}$. For imaginary l the waves become evanescent. However, linear ray tracing assumes the waves to be reflected when l becomes zero, thus the evanescent regime is not entered within this technique. It is worthwhile to briefly discuss the implications of (3.9) for the rays. Assuming $l > 0$ (i.e. pole-ward propagation) and increasing U with latitude, l decreases and its real part becomes zero at a certain latitude depending on β^* and m . When this latitude is reached the meridional component of the group velocity becomes zero and the wave no longer propagates in the meridional direction ($C_{gy} = 0$). This is the latitude where the ray tracing postulates the reflection of the wave with a change in sign of l thereafter. Hence by looking for the latitude where $l = 0$ one can find the latitude of maximum meridional propagation of a certain zonal wave number m . It is clear from (3.9) that the extend of meridional propagation is increased for smaller zonal wave number m .

Inspecting the stationary wave number profiles for our jet setup in Fig. 3.1c a decrease in latitude is evident for both profiles implying a refraction of stationary waves towards the equator. However, for the setup with a maximum jet speed of 10 m s^{-1} wave number 4 perturbations can be expected up to a latitude of 80° N , whereas the setup with 50 m s^{-1} can only sustain very large scale wave perturbations at higher latitudes.

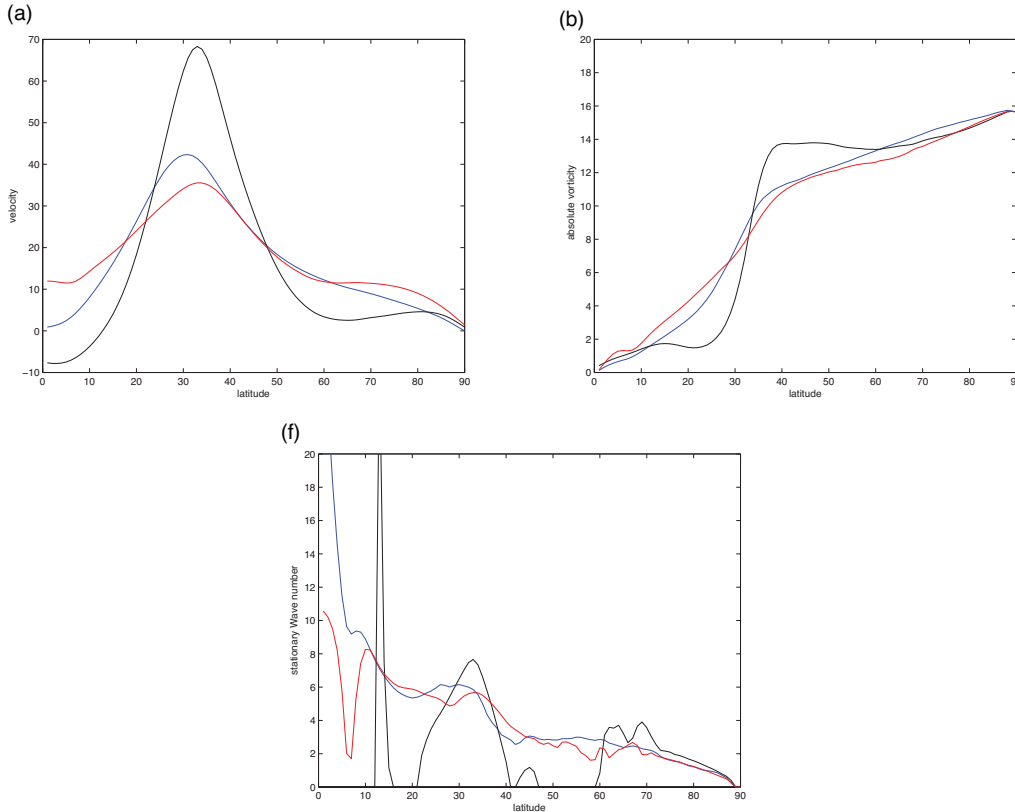


Figure 3.2: Zonal wind speed [m s^{-1}] (a), absolute vorticity [$\times 10^{-5} \text{ s}^{-1}$] (b) and stationary wave number K_s (c) as a function of latitude for the DJF mean at 200 hPa from ERA40 for zonal mean (blue), western Pacific [120-180 E] (black) and eastern Pacific [180-120 W] (red).

Fig. 3.2 shows the the zonal wind, absolute vorticity and stationary wave number at 200 hPa for the 1958-2002 December/January/February (DJF) mean from the ECMWF ERA40 re-analysis data-set (Uppala and Coauthors, 2005) for a comparison. The blue curves correspond to the zonal mean fields, whereas the black and red curves correspond to the fields averaged over 120-180 E (western Pacific) and 180-120 W (eastern Pacific), respectively. The zonal mean wind features a jet with a maximum amplitude of around 40 m s^{-1} at approximately 32° N similar to the eastern Pacific, whereas the western Pacific is dominated by a very strong sub-tropical jet with tropical easterlies. The strong jet in the western Pacific results in a very sharp increase in absolute vorticity around 33° N . The stationary wave numbers for the zonal mean and the eastern Pacific bear some similarities to our idealized flow setup, whereas in the western Pacific stationary wave propagation is inhibited in the low latitude easterlies and a wave guide is evident at the latitudes of the jet stream.

3.3 The linear QG stationary response to orography

In order to support our interpretation of the response in the 3D IFS global simulations it is worthwhile to briefly recapitulate the linear QG stationary response to orography on a β -plane. Following Pedlosky (1987) we use the QG vorticity equation

$$\left(v + \bar{u} \frac{\partial}{\partial x} \right) \left[\Psi_{xx} + \Psi_{yy} + \frac{f^2}{N^2} \left(\frac{1}{\rho} \frac{\partial}{\partial z} \rho \Psi_z \right) \right] + \beta \Psi_x = 0 \quad (3.10)$$

where Ψ is the QG stream-function, \bar{u} is a constant zonal flow, $N = 0.02 \text{ s}^{-1}$ is the Brunt Vaisala frequency, f is the Coriolis parameter and β its derivative in the y -direction. We centered the model at 30° N and included the effects of compressibility by letting $\rho = \rho_0 e^{-\frac{z}{H}}$, with $H = 7000 \text{ m}$ and $\rho_0 = 1.2 \text{ kg m}^{-3}$. The linear damping ($\nu = 6 \times 10^{-6} \text{ s}^{-1}$) term is added in order to remove the resonance of the solution at the stationary wave number. ν was chosen to be just large enough to prevent the perturbations to fully encircle the periodic channel in the x -direction, which lengths was chosen to be the circumference of the earth at 30° N . The lower boundary condition of the thermodynamic equation is used to force the waves, assuming $w = \bar{u} \frac{\partial h}{\partial x}$

$$\left(v + \bar{u} \frac{\partial}{\partial x} \right) \Psi_z = -\bar{u} \frac{N^2}{f} \frac{\partial h}{\partial x} \quad (3.11)$$

$$h(x, y) = \frac{h_0}{1 + \left(\frac{x}{L_x} \right)^2 + \left(\frac{y}{L_y} \right)^2} \quad (3.12)$$

where $h_0 = 2000 \text{ m}$ is the maximum mountain height and $L_x = L_y = 500 \text{ km}$ is the horizontal scale of the mountain. We can solve (3.10) by defining a streamfunction

$$\Psi = \chi(z) \Phi(x, y) \quad (3.13)$$

where we separated the horizontal and vertical components of the solution into $\Phi(x, y) = e^{i(kx + ly)}$ (k (l) is the wave number in the x (y)-direction) and $\chi(z)$, respectively. Substituting (3.13) into (3.10) we obtain

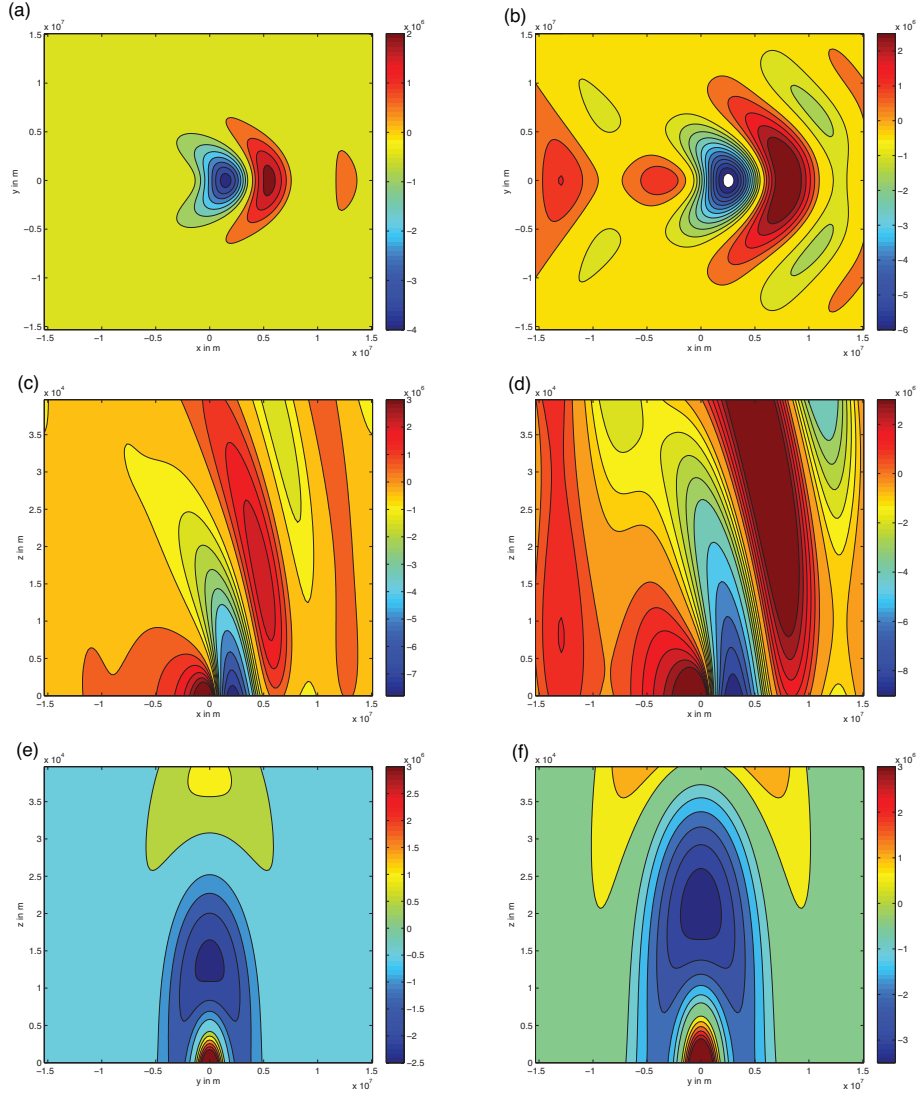


Figure 3.3: Streamfunction [$m^2 s^{-1}$] of linear, stationary, quasigeostrophic solution forced by a circular mountain. $\bar{u} = 20 m s^{-1}$ (a,c,e) and $\bar{u} = 40 m s^{-1}$ (b,d,f). $N = 0.02 s^{-1}$. Horizontal distribution at $z = 10$ km (a,b), vertical cross-section at central $y = 0$ (c,d) and vertical cross-section at $x = 0$ (e,f).

$$\chi_{zz} - \frac{1}{H}\chi_z + \frac{N^2}{f^2} \left(\frac{\beta ik}{v + \bar{u}ik} - (k^2 + l^2) \right) \chi = 0 \quad (3.14)$$

which can be solved by assuming $\chi = e^{\lambda z}$ yielding

$$\lambda_{1/2} = \frac{1}{2H} \pm i \left(\frac{N^2}{f^2} \left(\frac{\beta ik}{v + \bar{u}ik} - (k^2 + l^2) \right) - \frac{1}{4H^2} \right)^{1/2} \quad (3.15)$$

where we have an exponentially growing part with height $\frac{1}{2H}z$ due to the reduced density with height enlarging the perturbation and a complex part resembling the wave structure in the vertical. If the term within the square root becomes negative we obtain a non-oscillatory solution in the z -direction and have

to restrict (3.15) to be bound for $z \rightarrow \infty$. Hence we only allow for the plus sign in (3.15). On the other hand we apply the radiating boundary condition for $z \rightarrow \infty$ for wave propagation which also yields the plus sign in (3.15). The vertical wave number for $v = 0$ can be defined as

$$m_z = \left(\frac{N^2}{f^2} \left(\frac{\beta}{\bar{u}} - (k^2 + l^2) \right) - \frac{1}{4H^2} \right)^{1/2} \quad (3.16)$$

Thus for given spectra k and l and $f = \text{const}$, $N = \text{const}$, $H = \text{const}$, m_z decreases as u increases up to a critical value of u where m_z becomes imaginary and the solution becomes trapped in the vertical.

Figs. 3.3a,b show the horizontal propagation at a height of 10 km for a constant zonal flow of $\bar{u} = 20$ and $\bar{u} = 40 \text{ m s}^{-1}$, respectively. The typical downstream development of stationary Rossby waves with a constant background flow is evident with the main component of group velocity being directed downstream but also resembling some lateral components. The change in the dominant stationary wave number depending on \bar{u} is clearly evident ($K_s(20 \text{ m s}^{-1}) = 4.5$, $K_s(40 \text{ m s}^{-1}) = 3.2$). Figs. 3.3c,d show the vertical propagation in the downstream direction. The phase tilt for an upward and downstream group velocity is clearly evident. An interesting feature of meridional and vertical propagation is highlighted in Figs. 3.3e,f where a vertical cross-section in the y - z -direction is shown. The wave crests are aligned vertically above the mountain but bend down towards the ground away from the obstacle with a decrease in vertical wave number for increased zonal flow. This structure leads to a more 'barotropic-like' (i.e. the less varying with height) response further away from the mountain.

3.4 Global IFS simulations

In order to shed light on the different behavior of wave propagation depending on the basic state and the position of the forcing we present the time-space evolution of different responses and comment on their vertical and horizontal structure pinpointing intrinsic dynamical differences in the model simulations. The main focus herein lies on the latitudinal reach of perturbations and its sensitivity to the chosen model setup as well as the structure of the perturbation itself.

Fig. 3.4 shows the deviation from the zonal mean of geopotential at 300 hPa displaying the two main types of responses at day 20 in the model simulations. In Fig 3.4a two distinct ray paths of Rossby wave propagation are evident. One wave train propagates along the jet stream (approximately 40° N) and the

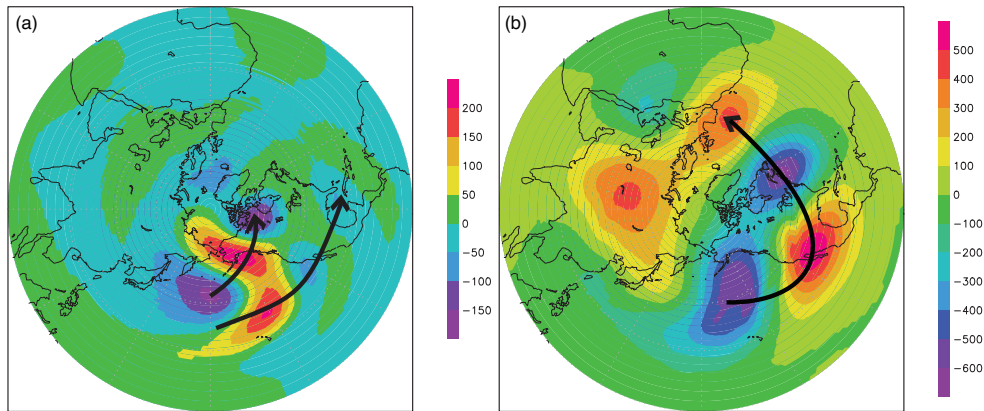


Figure 3.4: Deviation from zonal mean of geopotential [$\text{m}^2 \text{s}^{-2}$] at 300 hPa at day 20 of model integration. The mountain is located at 180° W and 20° N with a maximum jet speed of 10 m s^{-1} (left panel) or 50 m s^{-1} (right panel).

second wave train crosses the jet and propagates northward along a path similar to a great circle. On the other hand the wave train in Fig. 3.4b propagates exclusively along the jet stream. The waves in both cases were forced with the mountain centered at 180W and 20 N. The only difference in the initial setup is the maximum jet speed which was set to 10 m s^{-1} and 50 m s^{-1} in Fig 3.4a and b, respectively.

The effect of the wind speed on the response along the jet is also clearly evident in the dominant stationary wave number K_s . For the higher jet speed the wave number is lower compared to the setup with the reduced jet speed (see Fig. 3.1). Even though there is no clear wave signal evident north of the jet in Fig. 3.4b one can identify a wave number 1 pattern in the area north of 60° N where the two negative anomalies located at the west and east coast of North America and the two positive anomalies to the west of Spain and over central Asia join in the area of northern Canada and northern Europe, respectively. This suggests that some low wave number components of the forcing are still able to penetrate the jet.

3.4.1 Time evolution and vertical structure

In order to investigate the time evolution of the response along and to the north of the jet we show Hovmöller (1949) diagrams of geopotential averaged over $30^\circ\text{-}50^\circ \text{ N}$ (along jet) and $60^\circ\text{-}80^\circ \text{ N}$ (north of jet). We only show the wave number 1-8 components of the geopotential, hence the mean and the small-scale structures are removed. It should be noted that the exclusion of the higher wave number components does not significantly change the results, but in the following subsection we will discuss

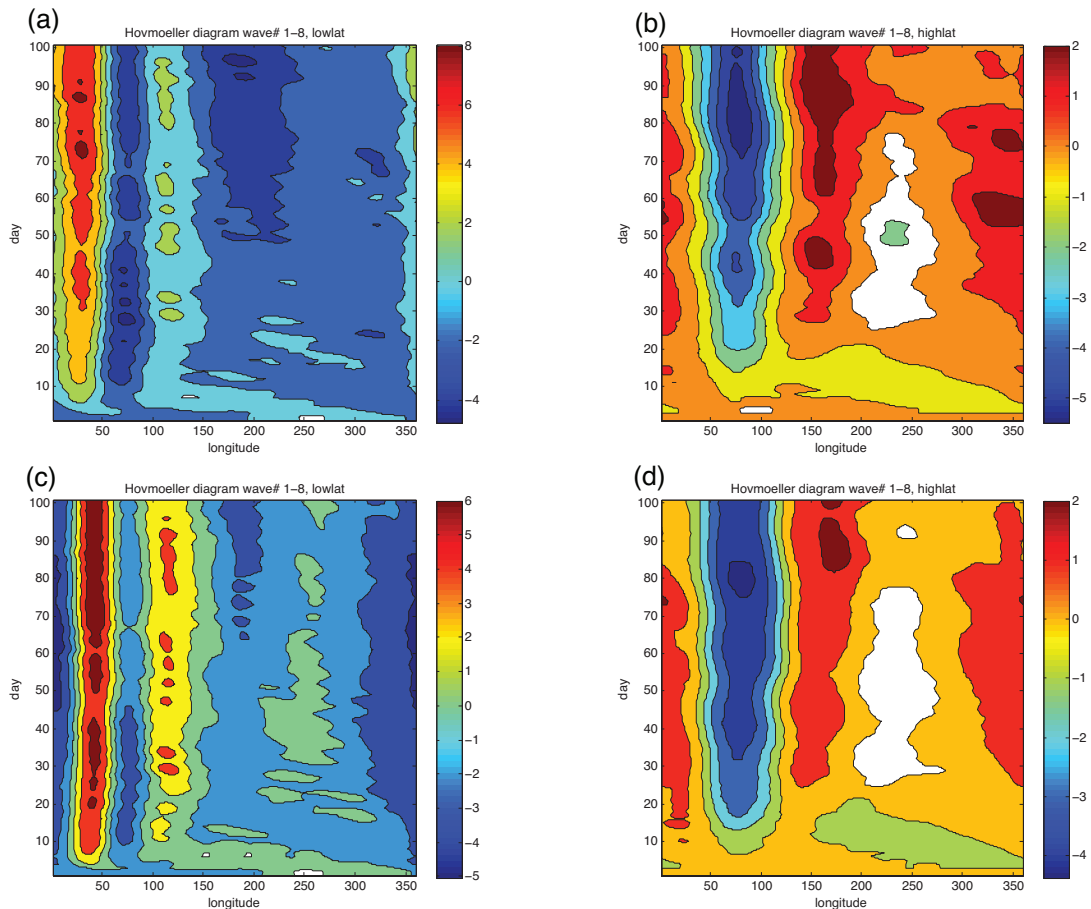


Figure 3.5: Hovmoeller diagram centered at the longitude of the mountain of geopotential [$\text{m}^2 \text{ s}^{-2}$] (only wavenumber 1-8 components) at 300 hPa (a,b) and 1000 hPa (c,d) averaged over $30\text{-}50 \text{ N}$ (a,c) and $60\text{-}80 \text{ N}$ (b,c) for maximum jet speed of 20 m s^{-1} . The mountain is centered at $180 \text{ W } 0 \text{ N}$.

wave detection based on the first eight Fourier components and therefor decided to restrict the focus to these wave numbers here as well.

Fig. 3.5 shows the time evolution of geopotential at 300 and 1000 hPa for the setup with a maximum jet speed of 20 m s^{-1} . The mountain is located at 180° W and 0° N . In all panels the stationary response (constant phase with time) to the mountain is clearly evident, but with a significantly lower wave number to the north of the jet (right panels). Comparing Fig. 3.5a and 3.5c there is a phase shift of about 45 degrees between the upper and lower levels. This phase shift is completely absent at higher latitudes (see Figs. 3.5b,d), suggesting that the response has a more barotropic nature north of the jet.

Fig. 3.6 shows the response for the same jet but with the mountain centered at 20° and 30° N . The response to the mountain at 20° N (Fig. 3.6a,b) resembles some similarities to the response where the mountain is at 0° N (Fig. 3.5) but the phase of the wave component north of the jet is shifted by 180 degrees. The latter shift suggest that the waves travelled different distances in the horizontal until reaching the higher latitudes. It is also evident that the response along the jet becomes less coherent with the mountain situated closer to the jet. Comparing Figs. 3.6a,c and Figs. 3.6b,d it is evident that the response along the jet becomes even less coherent as the mountain moves closer to the jet maximum and the response north of the jet is again shifted by about 90 degrees. In the simulation with the mountain located at 30° N the response north of the jet also starts to become disjointed in time. For both simulations there is again a clear difference in the leading wave number of the response indicating a reduced wave number at higher latitudes compared to the mid-latitude response. Like for the case with the mountain located at 0° N the response resembles a barotropic nature to the north of the jet whereas a phase shift in

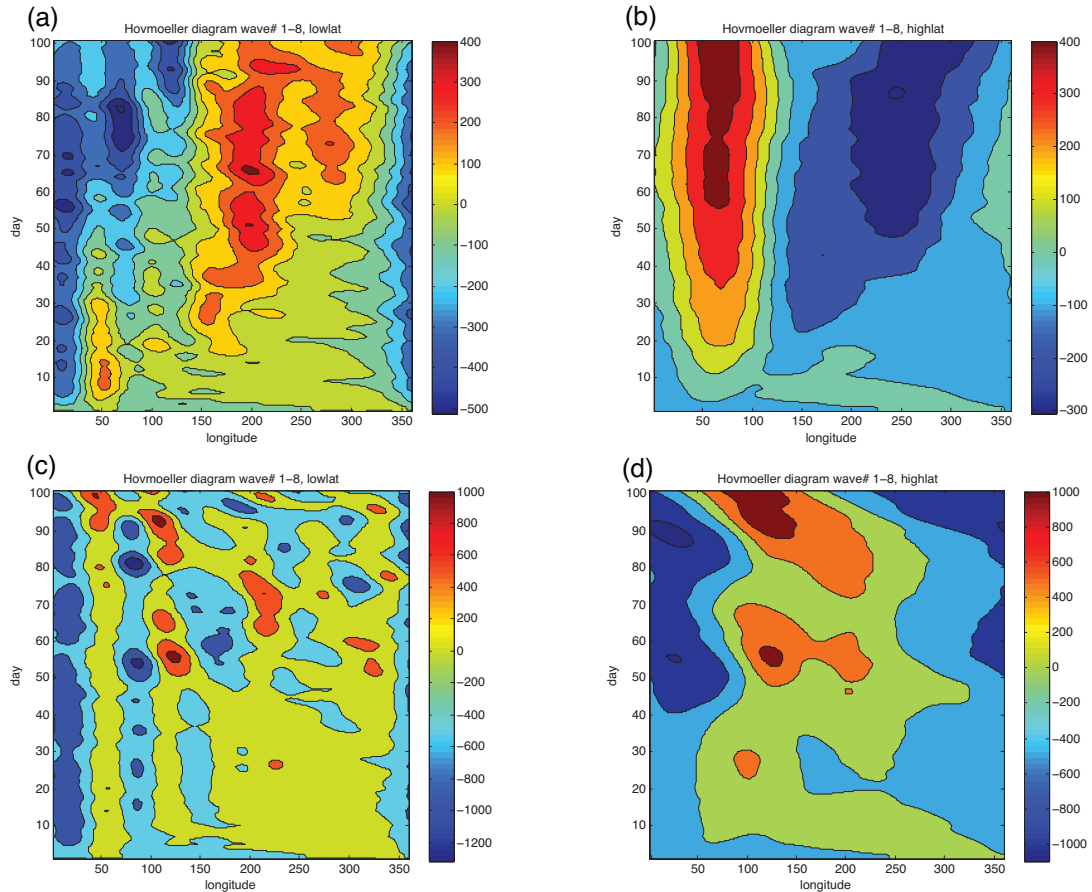


Figure 3.6: Hovmoeller diagram centered at the longitude of the mountain of geopotential [$\text{m}^2 \text{s}^{-2}$] (only wavenumber 1-8 components) at 300 hPa averaged over 30-50 N (a,c) and 60-80 N (b,c) for maximum jet speed of 20 m s^{-1} . The mountain is centered at 180° W 20° N (a,b) and 180° W 30° N (c,d).

the vertical is evident for the mid-latitudes (not shown).

The Hovmöller diagram in Fig. 3.7 shows the response for a maximum jet speed of 40 m s^{-1} , where the mountain is centered at 0° (Fig. 3.7a,b) and at 20° (Fig. 3.7c,d), respectively. Again the response along the mid-latitudes becomes less coherent if the mountain is located closer to the jet maximum. The phase of the response at higher latitudes is again shifted by about 150° for the different latitudes of the mountain. However there is only a small phase shift of 20° evident at mid-latitudes. At higher latitudes the response is dominated by a wave number one pattern whereas a wave number four pattern is evident at mid-latitude. Again the response at higher latitudes is barotropic in nature in contrast to its mid-latitude counterpart which exhibits a change of phase in the vertical.

3.4.2 Vertical structure along and to the north of the jet

In order to better understand the structural differences in the vertical Fig. 3.8 shows several vertical cross-sections of the deviation from the zonal mean of geopotential at day 10 for maximum jet speeds of 20 m s^{-1} (Figs. 3.8a,c,e) and 40 m s^{-1} (Figs. 3.8b,d,f), respectively. The mountain is centered at 0° N for all panels. The vertical cross-sections along the jet maximum (40° N, Fig. 3.8a,b) resemble the structure of vertical propagating Rossby Waves similar to the results obtained with the QG linear model (Fig. 3.3). The phase tilt featuring an upward and downstream propagation of wave energy is clearly evident. Examining Figs. 3.8c,d with the cross-sections at 60° N the orientation of the phase lines exhibits the same structures but with a reduced vertical wave number. Hence the response below 100 hPa

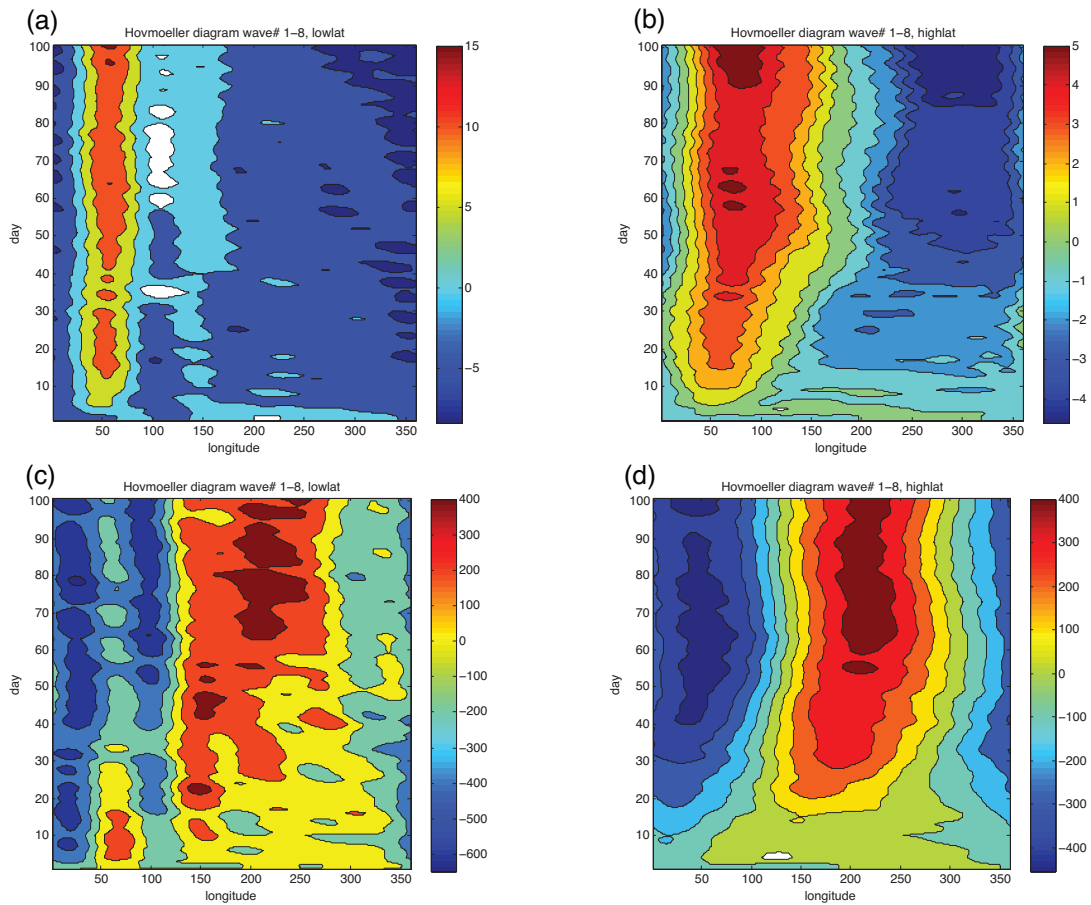


Figure 3.7: Hovmoeller diagram centered at the longitude of the mountain of geopotential [$\text{m}^2 \text{ s}^{-2}$] (only wave number 1-8 components) at 300 hPa averaged over 30-50 N (a,c) and 60-80 N (b,c) for maximum jet speed of 40 m s^{-1} . The mountain is centered at 180 W 0 N (a,b) and 180 W 20 N (c,d).

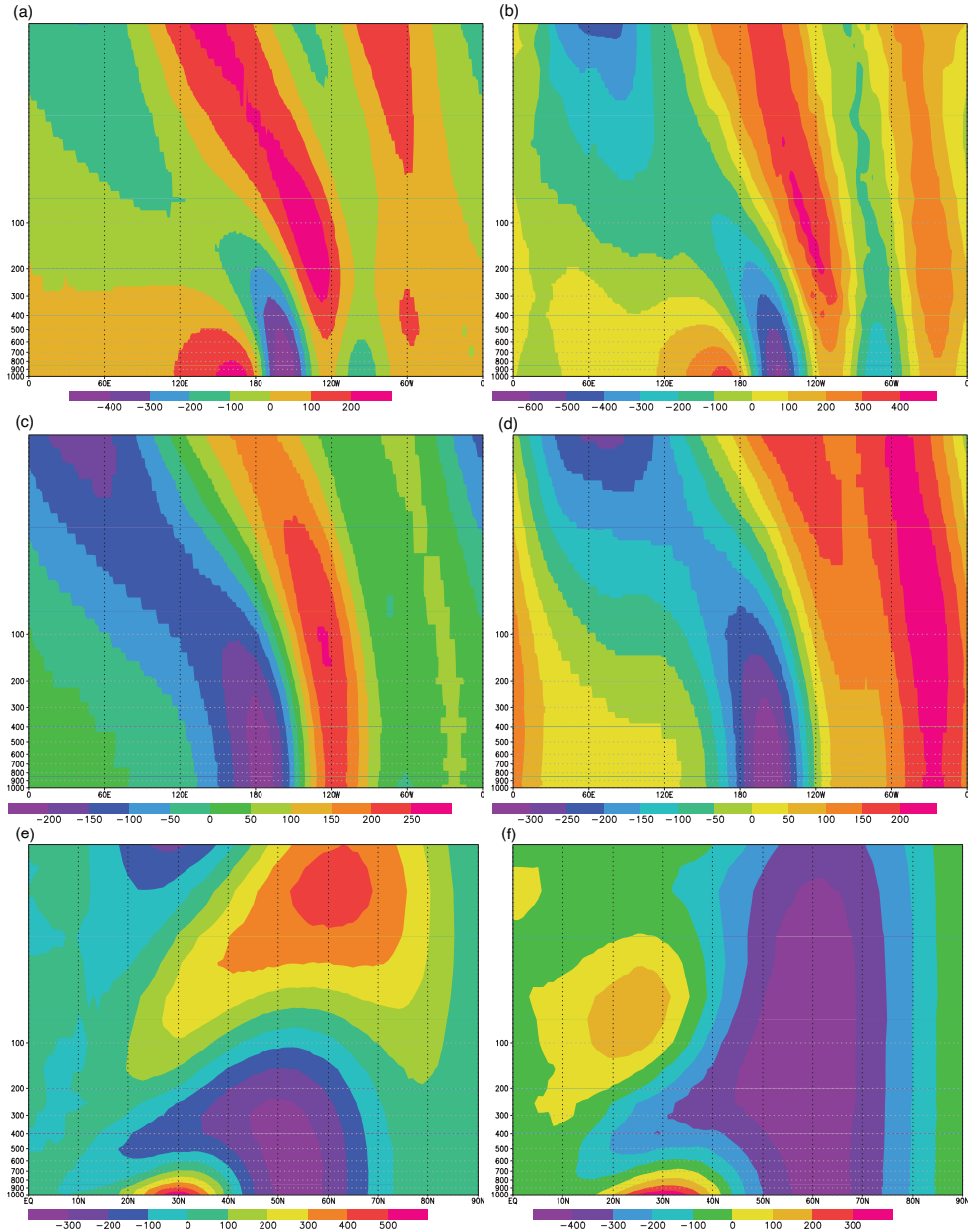


Figure 3.8: Vertical cross-sections of deviation from zonal mean of geopotential [$m^2 s^{-2}$] at day 10 for maximum jet speed of $20 m s^{-1}$ (a,c,e) and $40 m s^{-1}$ with the mountain centered at $20 N$. Cross-sections for constant latitude of $40 N$ (a,b) and $60 N$ (c,d) and at constant longitude of $180 W$ (e,f). The vertical axis ranges from 1000 to 5 hPa using a log scale.

at higher latitudes appears almost barotropic. This fact is nicely illustrated in the vertical cross-section along the $180 W$ meridian shown in Figs. 3.8e,f. For the case with a maximum jet speed of $20 m s^{-1}$ (3.8e) a vertically propagating wave is evident, which is refracted towards higher latitudes in the lower levels and propagates straight upwards at around $60^\circ N$. Again the pattern resembles great similarity to the linear QG solution presented in Fig. 3.3c. For the larger jet speed the negative perturbation takes up the space of the entire atmosphere up to 5 hPa north of $50^\circ N$. This reduction in the vertical wave number for increasing zonal flow is inherent in (3.16) where \bar{u} appears in the denominator. Thus the barotropic character of the response at higher latitudes can be explained by the nature of meridional and vertical propagation of stationary QG Rossby waves.

3.4.3 Wave detection along and to the north of the jet

The results presented in the previous section highlight the strong sensitivity of the wave response to the strength of the jet stream as well as to the center latitude of the mountain. Especially the dominant wave number north of the jet compared to its mid-latitude value is altered significantly as the wind speed increases. This is illustrated in Fig. 3.4 where a great circle type wave train is detectable for the jet with a maximum of 10 m s^{-1} whereas for the setup with the 50 m s^{-1} jet only a wave number one pattern is evident in the area north of 60° N .

In order to compile a comprehensive overview of these dependencies (maximum jet speed, latitude of mountain) impacting on the wave propagation we define a wave detection algorithm in order to look for differences in the wave spectra in the mid- and high-latitudes. A strength of our approach is that we are not restricted to a purely stationary discussion of the problem and will also be able to comment on the time evolution as well. We define R to be the ratio of the sum of the squared Fourier components of the geopotential averaged over $30^\circ\text{-}50^\circ \text{ N}$, $\hat{z}_{30-50}^2(m)$, and averaged over $60^\circ\text{-}80^\circ \text{ N}$, $\hat{z}_{60-80}^2(m)$, where m indicates the zonal wave number.

$$R = \sqrt{\frac{\sum_{m=j}^k \hat{z}_{60-80}^2(m)}{\sum_{m=j}^k \hat{z}_{30-50}^2(m)}} \quad (3.17)$$

This ratio represents the fraction of the perturbation penetrating the jet. The advantage of this approach is that we can separate different spectral bands from each other, which enables us to determine the dominant modes in the response. We showed that mainly zonal wave numbers $m \leq 4$ are evident at higher latitudes and that the wave number $m = 1$ dominates the response for higher jet speeds. In order to pinpoint the meridional reach of lower wave number perturbations as well as highlighting the impact of the wave number $m = 1$ pattern on the results we will focus on two spectral bands. The first band ($m = 1, \dots, 4$) is designed to detect a significant response at higher latitudes, whereas the second band ($m = 2, \dots, 4$) demonstrates the sensitivity of the detection to the wave number $m = 1$ component. In the following we define an event of significant penetration of the jet as the day when a threshold value of $R \geq 0.75$ is reached and if in addition the average of the remaining time series of the ratio is above the threshold value as well. The chosen threshold value proves very useful against a manual inspection of the three dimensional data set.

Fig. 3.9 shows the phase diagrams for the events defined above, where Figs. 3.9a,b,c correspond to the spectral band $m = 1, \dots, 4$ for different pressure levels (300, 500, 1000 hPa) and Fig. 3.9d shows the phase diagram for the spectral band $m = 2, \dots, 4$ at 300 hPa. If no event was detected for a certain set of parameters we omit the data point in the phase space. For the diagrams including the wave number one component there are several dependencies evident. There is an increase in time until an event is detected with increasing maximum jet speed. For example it takes less than 10 days to detect an event for a maximum jet speed of 10 m s^{-1} , whereas the time of detection varies between 15 and 30 days for the highest jet speeds. For jets with a maximum amplitude of 40 and 50 m s^{-1} there is a dependence indicating a delayed penetration of the jet if the mountain is located closer to the equator. Comparing Figs. 3.9a,b,c for different pressure levels it is clearly evident that an event is identified earlier at upper levels compared to the lower levels. The latter sensitivity is found to be strongest for the largest jet speed. Excluding the wave number one contribution from the ratio calculations changes the picture dramatically (Fig. 3.9d). Events are only detected for a maximum jet speed up to 25 m s^{-1} and for a maximum jet speed of 30 m s^{-1} if the mountain is located south of 30° N . When the mountain is located at the equator the time of an event is significantly increased. Also comparing Fig. 3.9a,d (both at 300 hPa) it is evident that the response is delayed if the wave number one component is omitted.

The strong sensitivity to the inclusion of the lowest wave number component in the ratio analysis

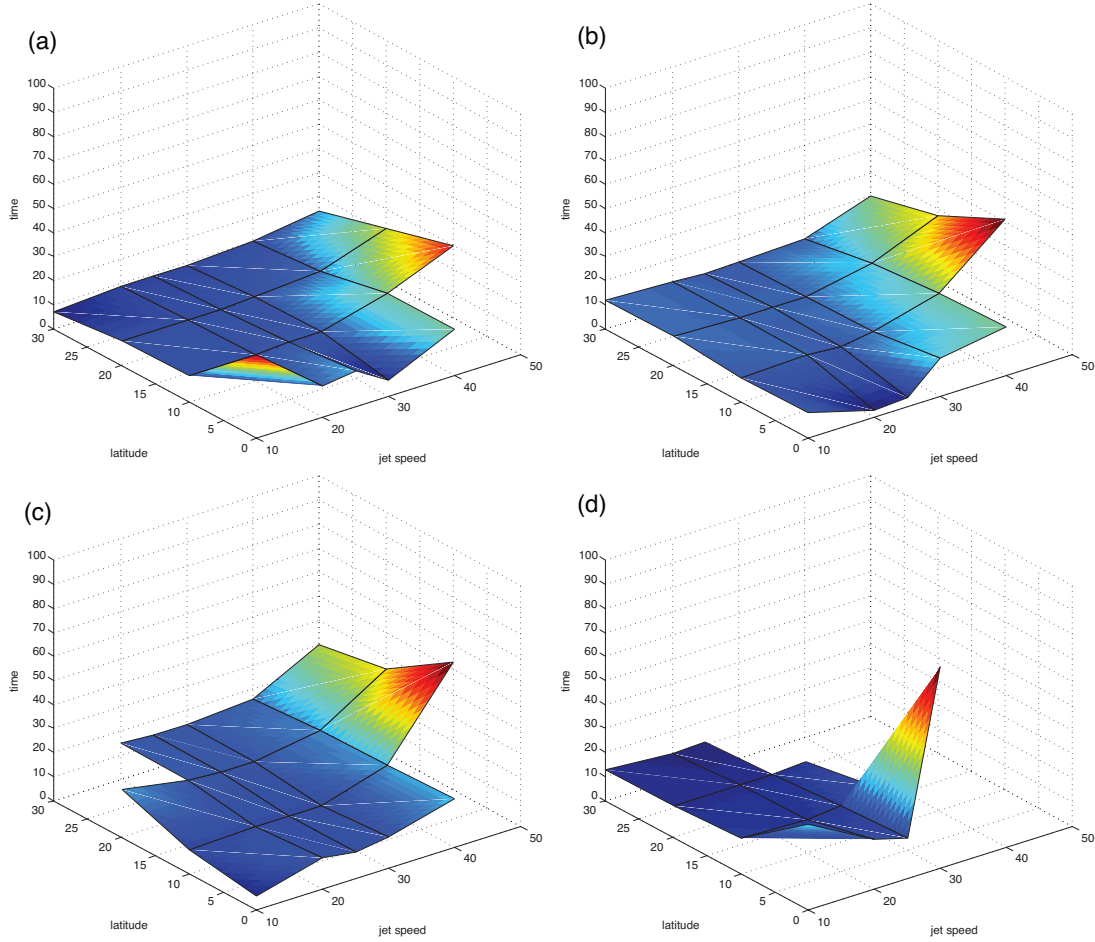


Figure 3.9: Phase diagram with time of wave detection depending on maximum jet speed and center latitude of mountain. The threshold is chosen to be 0.75 (see text for explanation) for wave numbers 1-4 (a,b,c) and 2-4 (d) of geopotential at 300 hPa (a,d), 500 hPa (b) and 1000 hPa (c).

pinpoints the dominance of this low component in the response for the experiments with higher maximum jet speeds. This fact is nicely illustrated in Fig. 3.10 where we show different time mean ratios of wave components at the same latitudes. The time mean ratio is defined as

$$r = \sqrt{\frac{\overline{\sum_{m=1}^j \hat{z}_{lat}^2(m)}}{\overline{\sum_{m=j+1}^k \hat{z}_{lat}^2(m)}}} \quad (3.18)$$

where lat can be either $30^\circ - 50^\circ$ N or $60^\circ - 80^\circ$ N and the over-bar indicates the time average over 100 days. For Figs. 3.10a,b we have chosen $j = 2$ and $k = 4$ limiting the focus on the large scale structures in the model simulations. The corresponding ratio for the latitudes centered around the jet maximum shows a clear dependence of the ratio on the latitude of the mountain indicating a shift to lower wave number components for a mountain situated at higher latitudes, i.e. closer to the jet. This is in contrast to the ratio at higher latitudes where the main dependence is on the maximum jet speed. Above 25 m s^{-1} there is a very rapid increase in the ratio with a maximum peaking at 40 m s^{-1} and a decrease thereafter for 50 m s^{-1} .

A rather different pattern is evident for the ratios focusing on the relative contributions of larger scale compared to synoptic scale wave components, i.e. $j = 4$ and $k = 8$ (Fig. 3.10c,d). At the lower latitudes

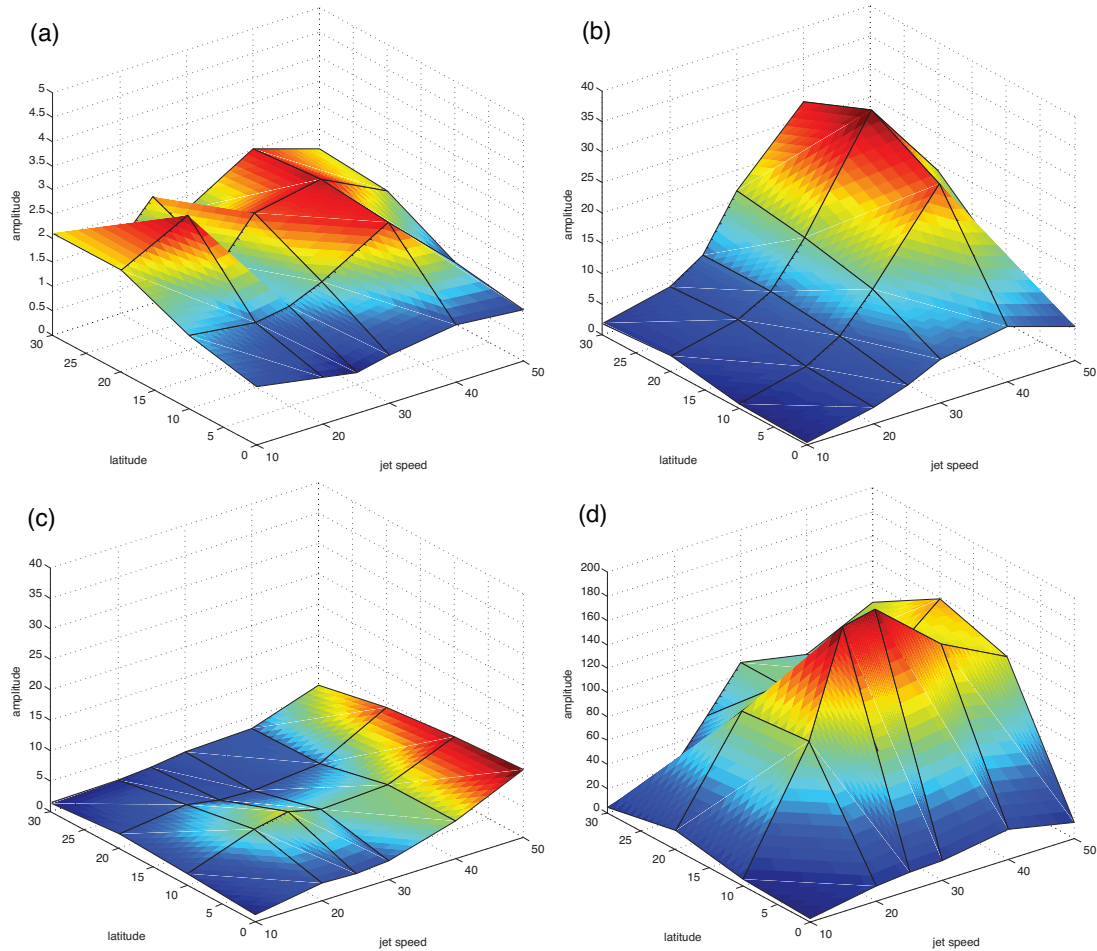


Figure 3.10: Phase diagram for different wave number ratios of geopotential averaged over 60-80 N (a,c) and 30-50 N (b,d) (see text for explanation). All panels are for 500 hPa. Wave number ratios 1-2/3-4 and wave number ratios 1-4/5-8 are shown in (a,b) and (c,d), respectively

the ratio depends strongly on the maximum jet speed. The phase diagram for the higher latitudes shows a similar dependency with increasing ratio with the maximum jet speed as above in Fig. 3.10b but now the maximum occurs for the mountain being centered at a latitude of 10° N and maximum jet speed around 25-30 m s⁻¹.

3.4.4 The southern hemisphere response

Similar to the analysis presented for the northern hemisphere we also investigated the response triggered by the mountain in the southern hemisphere. For the experiments with the mountain centered at the equator the results are symmetric in both hemispheres and we obtain the same features as discussed above for the northern hemisphere. However, if the mountain is shifted to the north of the equator the response in the southern hemisphere differs significantly from the northern hemisphere. Comparing the Hovmöller diagrams for the southern hemisphere at the mid- and high latitudes for the 20 and 40 m s⁻¹ jet stream (Fig. 3.11) with the same diagrams as for the northern hemisphere (Fig. 3.6a,b and Fig. 3.7c,d) the absence of the stationary wave patterns is evident. The response appears to be exclusively of transient nature with the characteristics of an westward wave propagation. The dominance of the wave number one component at higher latitudes is still evident in the southern hemispheric response and like for the northern hemisphere the wave number of the leading component is reduced at higher compared to the mid-latitudes.

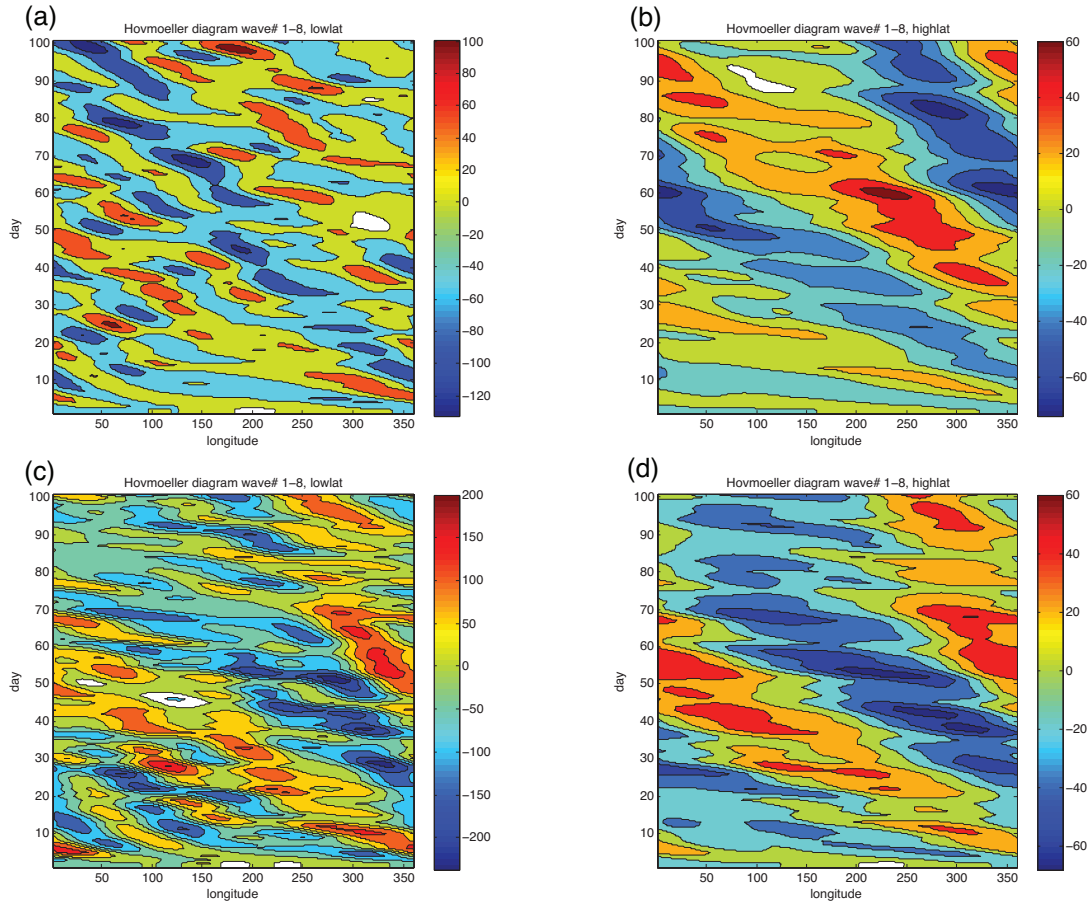


Figure 3.11: Hovmoeller diagram centered at the longitude of the mountain of geopotential [$m^2 s^{-2}$] (only wave number 1-8 components) at 300 hPa averaged over 30-50 S (a,c) and 60-80 S (b,d) for maximum jet speed of $20 m s^{-1}$ (a,b) and $40 m s^{-1}$ (c,d). The mountain is centered at 180 W 20 N.

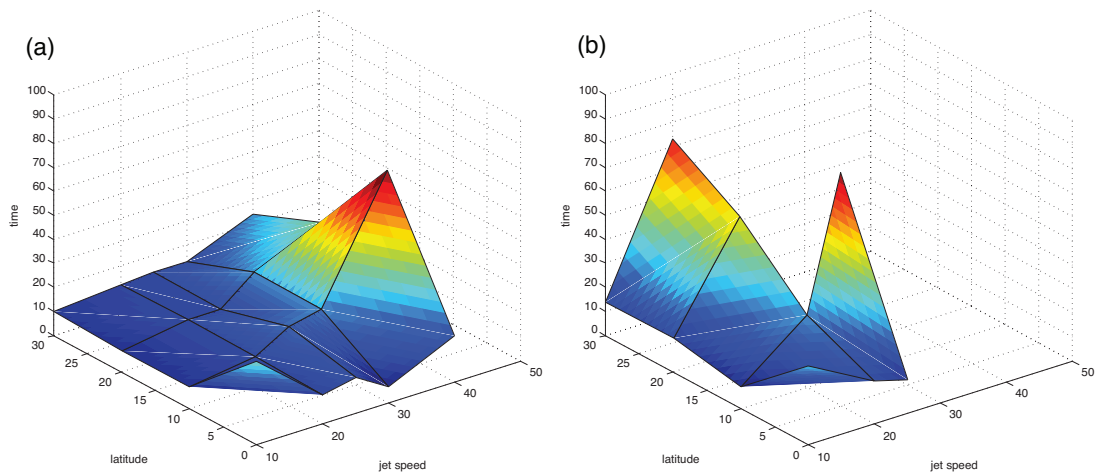


Figure 3.12: Phase diagram with time of wave detection depending on maximum jet speed and center latitude of mountain. The threshold is chosen to be 0.75 (see text for explanation) for wave numbers 1-4 (a) and 2-4 (b) for geopotential at 300 hPa.

Despite the non-stationarity of the response we also present the phase diagram with the events detected in the southern hemisphere for the same threshold as for the northern hemisphere (0.75) applied to the

wave number components 1-4 and 2-4 at 300 hPa (Fig. 3.12). The diagram for wave number 1-4 (Fig. 3.12a) resembles some similarities with its northern hemispheric counterpart, i.e. the increase in time of detection for higher jet speeds. The impact of excluding the wave number one component is shown in Fig. 3.12b, where events are now only detected for the low jet speed experiments. Hence even for the non-stationary response in the southern hemisphere the wave number one component dominates the analysis and has the largest contribution at higher latitudes as pointed out before for the Hovmöller diagrams.

In order to investigate the time mean relative contributions to the response along and to the poleward of the jet Fig. 3.13 shows the different ratios with $j = 2$ and $k = 4$ (3.13a,b) as well as $j = 4$ and $k = 8$ (Fig. 3.13c,d). Comparing Fig. 3.13a,b with Fig. 3.10a,b for the low spectral ratios a similar rather flat distribution is evident along jet. However, the higher latitude response differs significantly, where no distinct peak at the 40 m s^{-1} jet speed is evident for the southern hemisphere. There is a maximum around $25\text{-}30 \text{ m s}^{-1}$ but it is much less pronounced than its northern hemispheric counterpart. The ratio for the lower to higher spectral bands in Fig. 3.13c bears some similarities to the northern hemisphere (Fig. 3.10c) but featuring a much stronger increase with jet speed exhibiting a very steep ascent from 40 to 50 m s^{-1} . Fig. 3.13d shows that the higher spectral ratios at higher latitudes are also very distinct to the northern hemisphere where an increase of the ratio with the latitude of the mountain is evident with the strongest change between 10° and 20° N , whereas Fig. 3.10d reveals a maximum at 10° N for the northern hemisphere.

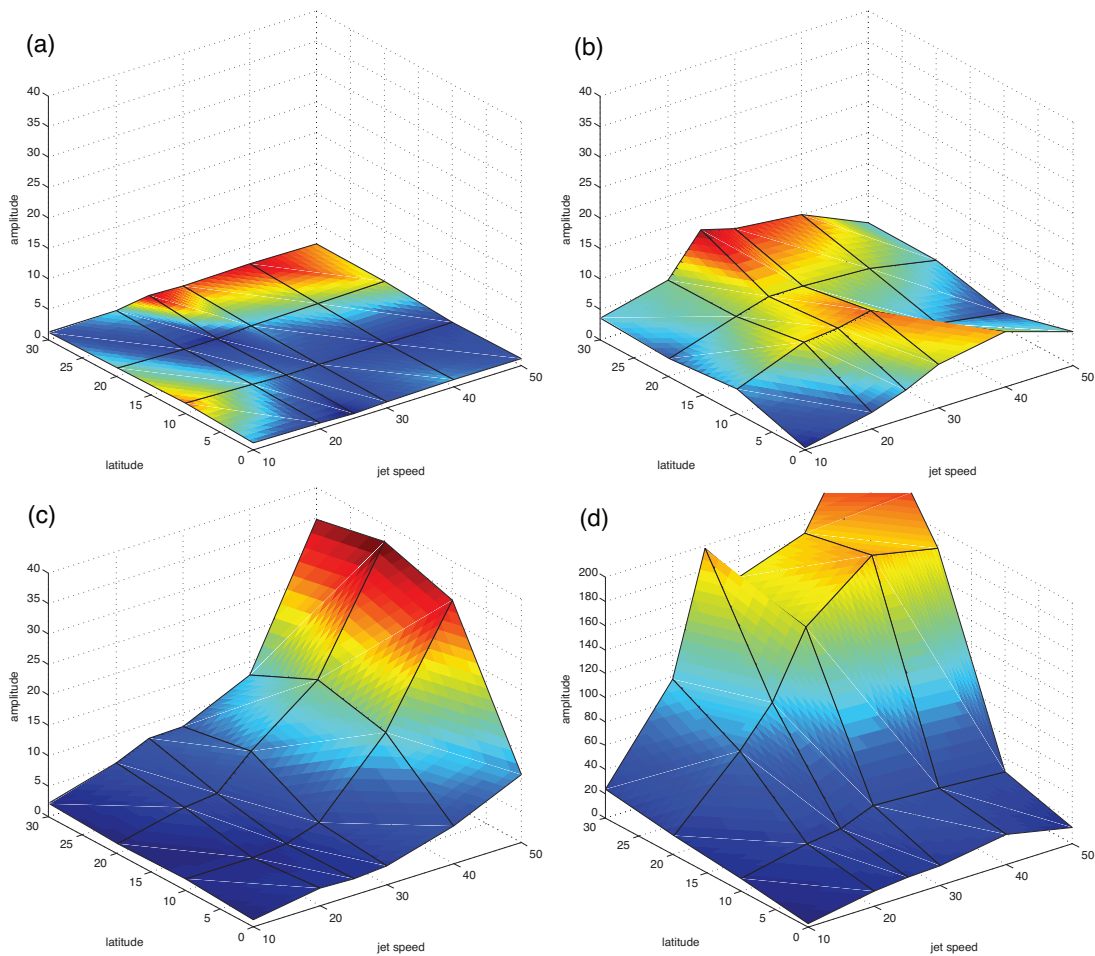


Figure 3.13: Phase diagram for different wave number ratios of geopotential averaged over $60\text{-}80 \text{ N}$ (a,c) and $30\text{-}50 \text{ N}$ (b,d) (see text for explanation). All panels are for 500 hPa . Wave number ratios 1-2/3-4 and wave number ratios 1-4/5-8 are shown in (a,b) and (c,d), respectively

3.5 Discussion

In order to shed light on the differences in dynamical behavior dependent on the jet speed as well as the latitude of the mountain we will now discuss the different patterns presented above by adopting the concepts of linear barotropic and QG Rossby wave theory. At the end of this section we will also present sensitivity studies to underline the general validity of the experiments carried out.

Fig. 3.14 shows the meridional wave number l (see eq. (3.9)) depending on different zonal wave numbers m for the jet setup with 10, 20, 40 and 50 m s^{-1} . Since the meridional propagation reaches the latitude where l becomes zero the zonal wave number $m = 1$ always has the furthest reach in the experiments. We find that zonal wave numbers $m = 1, \dots, 4$ reach significantly northward of 60°N for the 10 m s^{-1} jet, whereas only $m = 1, 2$ can be expected to penetrate north of 60°N for 30 m s^{-1} and for the 50 m s^{-1} jet only zonal wave number one will be able to reach the higher latitudes. This is in very good qualitative agreement with the analysis presented in the previous section where for a jet speed of 20 m s^{-1} zonal wave number one and two dominated the higher latitude response whereas for a jet speed of 40 m s^{-1} only evidence of wave number one was found at higher latitudes. The dominant zonal wave numbers at the mid-latitudes were found to be 4, 5 and 6 for the two jet speed setups. Since the response along the jet can be expected to propagate exclusively along the jet, i.e. $C_{gy} = 0$, we can assume $l = 0$ and thus can identify the dominant zonal wave numbers in Fig. 3.14. For 20 and 40 m s^{-1} we find zonal wave number 4, 5 and 6 to be the the ones for which l becomes zero within the latitude band of

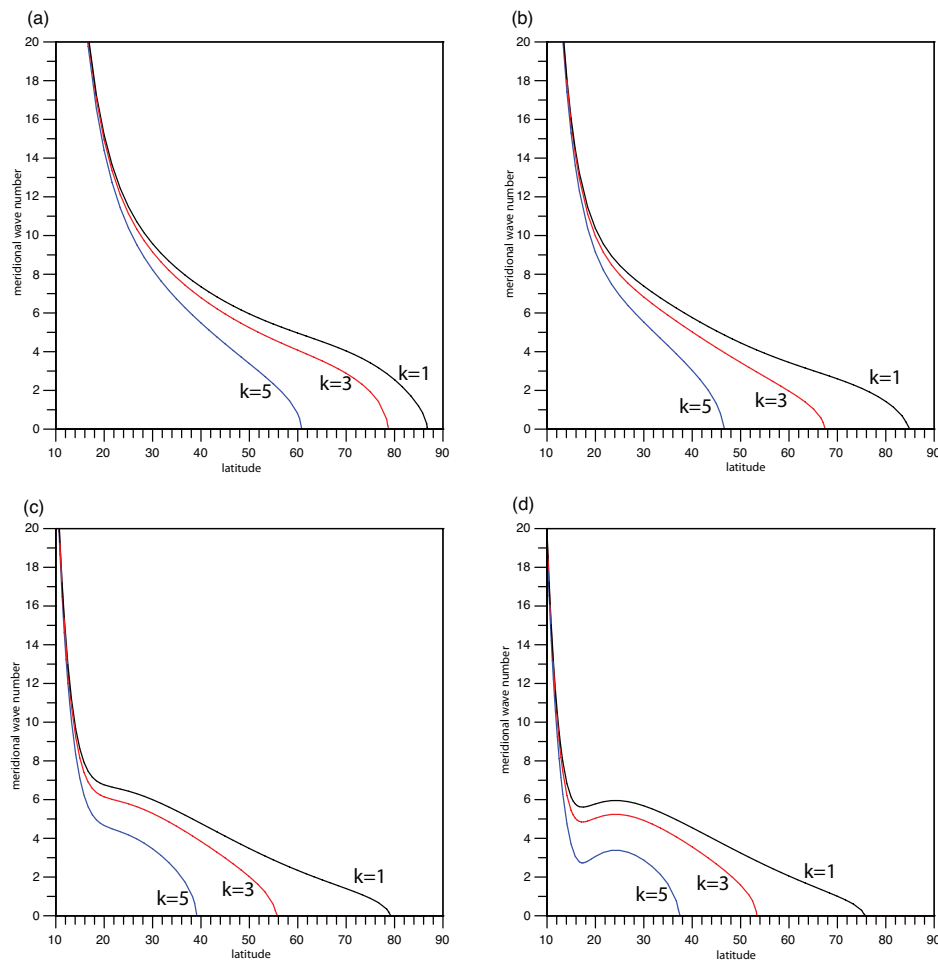


Figure 3.14: Meridional wave number l for $k = 1, 3$ and 5 in black, red and blue for maximum jet speed of 10 m/s (a), 20 m/s (b), 40 m/s (c) and 50 m/s (d).

30°-50° N, which again demonstrates the usefulness of the linear barotropic theory.

However, it was also shown that the dominant wave number also depends on the latitude of the mountain, which cannot be simply explained by the diagram in Fig. 3.14. Furthermore there was a dependence of the phase shift evident as well. Comparing Figs. 3.5a, 3.6a and 3.6c for the 20 m s⁻¹ jet with the mountain located at 0°, 20° and 30°, respectively, an increase of zonal wave number is evident with increasing latitude of the mountain. The dominant wave numbers are still the ones predicted by the stationary theory, i.e. 4, 5 and 6, but the dominant contributions vary significantly with the latitude of the mountain with an increase in zonal wave number as the mountain moves closer to the jet. This can be explained by the wave numbers forced by the mountain at its latitude. The mountain will mainly force the wave components which correspond to the stationary wave number at and around the latitude of the forcing. Hence according to Fig. 3.1 the forced spectra will include higher zonal wave numbers at the lower latitudes compared to the latitudes of the jet. The stationary wave number for the 20 m s⁻¹ jet at 20° N is $K_s(20^\circ) = 10.4$ and for 30° $K_s(30^\circ) = 7.4$. Thus there are a lot of components forced by the mountain which are not sustainable further northward and will decay away from its source. Due to their northward evanescence these wave components are only detectable close to the mountain, thus the further the mountain is away from jet the less impact these components will have on the latitudes of the jet, but if the mountain is closer to jet there will be a fingerprint on the jet latitudes of the higher wave number evanescent components. Comparing Figs. 3.7a,c the impact of the higher wave numbers is less evident for the 40 m s⁻¹ jet. There are two reasons for that. First the stationary wave number for a mountain centered at 30° N is $K_s(30^\circ) = 6.1$, thus already close to the observed wave number 5 and on the other hand the wave number 6 component is highly evanescent in the jet latitude band compared to the 20 m s⁻¹ jet where even wave number 6 is still sustainable up to about 40° N becoming evanescent only further northward.

The maximum in the ratios at 40 m s⁻¹ in Fig. 3.10 can be explained by utilizing Fig. 3.14. The stationary wave number at the latitudinal belt of interest (60°-80° N) remains above one for the entire area for 40 m s⁻¹ whereas it becomes less than one in the northern part of the belt for the 50 m s⁻¹ jet. This again implies that this wave number is not sustainable at higher latitudes and will be reflected before crossing the belt or be evanescent further northwards. This results in reduced mean amplitudes for the 50 m s⁻¹ jet compared to the 40 m s⁻¹.

In order to explain the non-stationary response in the southern hemisphere we can again utilize (3.9). As pointed out above and as is evident in Fig. 3.11 the planetary waves have a negative, i.e. westward, phase speed, which appears to be rather small (≈ 50 days to encircle the globe for wave number one at higher latitudes and about 60-70 days for wave number ≈ 4 at mid-latitudes).

Inspecting (3.9) meridional propagation is still possible at $\bar{u} = 0$ if $c < 0$, i.e. westward propagating Rossby waves can be transmitted into the southern hemisphere through the critical latitude for stationary Rossby waves. This explains the existence of westward propagating planetary waves in Fig. 3.11 for the southern hemisphere. Since the arguments of wave refraction in (3.9) are still valid for propagating waves with constant phase speed for a given zonal wave number we expect only lower zonal wave numbers to penetrate into higher latitudes, like for the northern hemisphere. Since we know the approximate phase speeds of the waves crossing the equator we can calculate the meridional wave number at the equator for $m = 1$ with $c \approx 10$ m s⁻¹ and $m = 4$ with $c \approx 7.5$ m s⁻¹ yielding $l \approx 10$ for both cases. Hence there seems to exist a preferred meridional wave number for equatorial transmission independent of the zonal wave number. We obtain the same results if the mountain is located at 30° N. However, so far we are unsure which mechanisms determine this wave number for the mountain centered at 20° and 30° N and can only speculate about possible reasons. The wave number might in fact be dependent on the model resolution as well as be dependent on dynamical aspects. If the mountain is located at 10° N the phase speed is significantly reduced (not shown) and the transmitted equatorial meridional wave number changes. The most plausible cause for the different behavior for the mountain centered at 10° N is the possibility of wave transmission due to its proximity to the equator where the edge of the mountain reaches the equator.

3.5.1 Sensitivity to the size and height of the mountain

All experiments were carried out with the identical mountain, i.e. 2000 m high and with a radius of one third of the radius of the earth. Within linear QG theory the lower boundary condition (3.11) is used to force solutions in (3.10). Neglecting damping and utilizing λ from (3.15) the amplitude of the mountain forcing at $z = 0$ becomes

$$\hat{\Phi}(k, l) = -\frac{N^2}{f\lambda} \hat{h}(k, l) \quad (3.19)$$

where the $\hat{\cdot}$ denotes the Fourier transforms of the variables. Hence the response at the same latitude, i.e. same f and β with identical N and the same mountain, $\hat{\Phi}$ depends only on $\frac{1}{\lambda}$. For wave solutions where $m_z^2 > 0$ the real part of $\hat{\Phi}$, thus its amplitude, is almost unaffected by changes in \bar{u} which will primarily impact on the phase shift of the solution. We tested this by running the QG model for different \bar{u} and only found a weak sensitivity of the lower boundary condition to changes in the background flow. Held and Ting (1990) showed that the amplitude of the response in a baroclinic atmosphere is directly proportional to \bar{u} . Thus the vertical shear of the background flow, i.e. the meridional temperature gradient, dominates over the advection of the perturbation potential temperature by the zonal background flow. However, due to the barotropic nature of our model setup their results are not applicable to the study presented here.

Anyhow, the amplitudes of the responses in the different experiments can be separated by a factor of 100 indicating that linear QG theory does not hold for a fully non-linear model. Pierrehumbert (1985) derived the non-dimensional number $Fr^{-1}Ro$ as the key parameter for non-linearity for rotational flow across topography, where Fr^{-1} is the inverse Froude number $\frac{Nh}{U}$ and Ro is the Rossby number $\frac{U}{fL}$. For values $FrRo < 1$ Pierrehumbert (1985) concludes that the flow can be treated as approximately linear. For the setup of our experiments with the mountain located at 10° , 20° and 30° N we obtain $FrRo \approx 0.8$, 0.4 and 0.25 , respectively. We are not able to calculate $FrRo$ for the experiments at the equator since $Ro \rightarrow \infty$. Hence according to Pierrehumbert (1985) all our calculations are carried out in a quasi-linear framework. However, one should bear in mind that Pierrehumbert (1985) neglected the β -term in his semi-geostrophic set of equations disallowing for the existence of Rossby wave propagation.

A plausible cause for the difference in the experiments with the different jet speeds is the resonance at the stationary wave number evident in (3.19) for $K_s = \sqrt{m^2 + l^2} = \sqrt{\frac{\beta}{\bar{u}}}$ where the denominator becomes zero. The leading zonal wave number of the mountain spectrum is around 9-10 for all mountain latitudes. Assuming l to be small (zonal propagation) one can directly infer the resonant m from Fig. 3.1. Thus for mountains located at 10° and 20° N the response is much closer to resonance for higher jet speeds where the stationary wave number is smaller compared to the lower jet speeds. However, m_z can become imaginary for increasing \bar{u} reducing vertical propagability which would account for a reduced response at upper levels.

The discussion above shows that we cannot rule out non-linearity in our calculations and it might in fact play an important role in determining the difference in the amplitudes of the responses. In order to strengthen the confidence in the results presented here we carried out several experiments to check for the sensitivity of the results to the size and height of the mountain pinpointing the robustness of the material presented. We reran the experiments with maximum jet speeds of 20 and 40 m s^{-1} and the mountain centered at 0° and 20° N with half the radius, i.e. $R=a/6$ and also repeated the same experiments with the original radius but with the height reduced to 500 m. The differences in the results based on the wave detection as well as the ratios of the different wave spectra are not significant. In fact the day of detection is on average only shifted by $\pm 3 - 6$ days. However, the amplitude of the response is significantly reduced for all experiments where the mountain size or height is reduced indicating that the spectrum as well as the height of the mountain are key players in determining the amplitude of the response.

3.6 Final remarks

We presented the time and space evolution of a global response to a single mountain in an idealized atmospheric setting with a zonal jet in each hemisphere. The latitude of the mountain as well as the maximum jet speed were varied to pinpoint the dynamical influences on the wave propagation.

In accordance to earlier studies we find that a constant forcing (i.e. the mountain) always yields a stationary response in the hemisphere in which it is centered and that the response is mainly composed of two wave trains: One along the jet and one crossing the jet into higher latitudes. The concepts of ray tracing of stationary non-divergent barotropic Rossby waves proved to be useful in order to explain the differences in the 3D response. Especially the dependence of the higher latitude response was to a great extent attributable to differences in the latitudinal profiles of the stationary wave number.

The lateral structure of forced QG stationary Rossby waves accounts for the difference in the vertical composition of the response along (wave-like in vertical) compared to north of the jet (quasi-barotropic). Furthermore we found that a change in the latitude of the mountain leads to a phase shift of the stationary response north of the jet, which can be attributed to the different path lengths of the rays of the waves.

A remarkable finding of this study is the non-stationarity of the response in the hemisphere without the mountain. We were able to explain the existence of a non-stationary response by Rossby wave theory and showed that the concepts of wave refraction still hold for waves with a phase speed unequal zero. However, the mechanism generating the non-stationary Rossby waves at the equator is still unknown and requires further investigation.

Chapter 4

Extra-tropical response to stationary and non-stationary tropical heating: Non-linear global simulations with a zonally asymmetric jet stream

4.1 Introduction

Global teleconnection patterns identified by e.g. Wallace and Gutzler (1981), Horel and Wallace (1981) and Barnston and Livezey (1987) show statistical evidence for the interaction of distant regions raising the question of their dynamical cause and about the atmospheric mechanisms involved in their generation. Especially the North Atlantic Oscillation (NAO) (e.g. Wanner et al., 2001) and the Pacific/North America pattern (PNA) (e.g. Wallace and Gutzler, 1981) have received great attention over the last decades. Whereas the PNA is seen as a pattern of seasonal variability Feldstein (2002) showed that the PNA anomaly completes its life cycle within 2 weeks indicating the sub-monthly character of the dynamics involved in its generation highlighting the importance of sub-seasonal dynamics in the generation of the PNA.

There are a number of studies relating the growth of low-frequency patterns such as the PNA to linear dispersion of Rossby waves from a source of tropical heating via energy transmission along ray paths resembling great circles (Hoskins et al., 1977; Hoskins and Karoly, 1981) producing patterns like the PNA. Studies mainly comprise a stationary (Hoskins and Ambrizzi, 1993; Lim and Chang, 1983; Branstator, 1985; Sardeshmukh and Hoskins, 1988; Ting and Sardeshmukh, 1993; Ting and Yu, 1998) or non-stationary (Jin and Hoskins, 1995) approach linearized about idealized basic states or the climatological mean winter flow. Other studies propose a barotropic instability due to the zonal asymmetry of the climatological winter mean state as the key mechanism (Simmons et al., 1983; Frederiksen, 1983; Frederiksen and Webster, 1988; Branstator, 1990, 1992). However, it was shown that small changes in the damping or in the forcing eliminate the instability (Borges and Sardeshmukh, 1995; Ting and Sardeshmukh, 1993; Ting and Yu, 1998) casting doubt on role of the proposed mechanism. Further studies indicate the importance of high-frequency eddy feedbacks on the time mean state of the atmosphere in generating low-frequency variability patterns such as the PNA (Egger and Schilling, 1983; Nakamura and Wallace, 1993; Branstator, 1995; Jin et al., 2006).

However, more or less all studies agree on the importance of a tropical forcing in the equatorial eastern Pacific as a trigger for the perturbation in the extra-tropics. One of the most prominent patterns of tropical variability connected to outbreaks of strong convective activity, and thus diabatic heating, is the Madden-Julian Oscillation (MJO) with a recurrence of about 40 days (Madden and Julian, 1971, 1972, 1994; Zhang, 2005). During its convective active phase the MJO is characterized by a slowly eastward progressing (5 m s^{-1}) conglomeration of convection along the equator, where the active phase is limited to the Indian and eastern to central Pacific Ocean (Hendon and Salby, 1994; Matthews, 2000; Zhang, 2005). There have been several studies investigating the impacts of the MJO on the mid-latitudes by means of data analysis and composite studies (Liebmann and Hartmann, 1984; Lau and Phillips, 1986; Knutson and Weickmann, 1987; Kiladis and Weickmann, 1992; Hsu, 1996; Higgins and Mo, 1997; Matthews and Kiladis, 1999; Kim et al., 2006) or modeling approaches (Salby et al., 1994; Hendon and Salby, 1996; Matthews et al., 2004). The MJO was shown to have a significant impact on the mid-latitudes by initiating global circulation patterns as well as changing the Pacific wave guide. Recently Mori and Watanabe (2008) investigated the direct impact of the MJO on the PNA by examining composite life cycles of the PNA. They found a strong coherence between the MJO and the development of a wave train along the Pacific wave guide which they hypothesize to be generated by the divergent winds

primarily associated with anomalous convection of the MJO.

The studies listed above try to describe the dynamical mechanisms involved in the interaction of a tropical diabatic heating (as comprised e.g. by the MJO) and the mid-latitude wave guide mainly based on composite analysis or theories relating evolutions on synoptic time-scales to low-frequency variability. However, the day-to-day high-frequency interactions are still yet to be determined. The wave train along the Pacific wave guide initiated by the MJO (Mori and Watanabe, 2008) resembles the characteristics of a downstream development (Simmons and Hoskins, 1979; Chang, 1993; Chang and Yu, 1999; Chang, 1999). Hakim (2003) and Danielson et al. (2006) also investigated the occurrence and dynamics of downstream developments in the Pacific sector. Latter study successfully used wave activity fluxes (Takaya and Nakamura, 1997a,b) to diagnose the downstream progression of wave energy. However, it should be noted that our dynamical understanding of downstream development, especially the determination of the phase and group velocity of the perturbation, is still rather limited (Chang, 1999; Hakim, 2003). Since Mori and Watanabe (2008) clearly indicate a relationship between the MJO and a subsequent downstream development along the Pacific mid-latitude wave guide it is desirable to gain a better understanding of the dynamics involved in the initiation of the wave train by tropical convection.

In the work of Schierz et al. (2004) the generation of a wave train along a wave guide is discussed in an idealized analytical model. They basically show that the impact of a balanced vortex at some distance to the wave guide is sufficient to produce a downstream development where the characteristics of the wave train are mainly defined by the basic state and only the amplitude of the response is determined by the distance of the vortex to the wave guide and by its amplitude.

In our study we will focus on the non-linear interaction between a prescribed stationary or migratory tropical heating with the extra-tropical flow. The experiments are conducted with the fully non-linear adiabatic version of the global model from the European Centre for Medium Range Weather Forecasts (ECMWF). The model is run in the Held-Suarez (HS, Held and Suarez, 1994) setup. This setup allows for the maintenance of a meandering baroclinic mid-latitude jet enabling an interpretation of the results beyond the realm of linearity and with a more complex and asymmetric structure of the atmosphere compared to a climatological mean. The non-linear response to tropical forcing has previously been studied by Lin and Derome (2004). They found that the amplitude of the PNA features a linear relationship to the magnitude of the tropical forcing. However their study is based on statistics of a long time integration whereas here we will focus on the synoptic evolution of the response in time pinpointing some of the most relevant dynamical processes involved.

Even though the forecast performance on the onset and the progression of the MJO is still very poor in today's numerical weather prediction models (Ferranti et al., 1990; Hendon et al., 2000; Zhang et al., 2006) the results presented in this study help to pinpoint some of the key mechanisms involved in the interaction between a tropical heating and the mid-latitude wave guide shedding light on the main sensitivities of the response.

In section 4.2 we introduce the model used for this study followed by the description of the initial conditions and specify the forcing. In section 4.3 we present the method used for our investigation. Our results are presented in sections 4.4 and 4.5 followed by our discussion of the presented material in section 4.6. In section 4.7 we briefly summarize our findings.

4.2 Experiment setup

4.2.1 Model

We utilize the CY31R2 version of the ECMWF Integrated Forecast System (IFS) (see ECMWF (2007) and references therein). In a nutshell the IFS is a hydrostatic, primitive equation, global spectral model with hybrid levels ($0 \leq \eta \leq 1$) in the vertical (Simmons and Burridge, 1981). It employs a semi-Lagrangian semi-implicit time-stepping scheme and was developed for operational forecasts at ECMWF.

Our experiments are performed with a stripped-down version of the model (i.e. dynamical core), basically constituting an adiabatic version of the full code where we set the model orography to zero everywhere. Since this model version does not allow for an interaction with the surface the atmosphere, there is no response to land-sea contrasts. The model is run in the HS setup which basically comprises a temperature relaxation yielding a baroclinic jet in each hemisphere centered at about 40° N/S and maximizing at a height of around 200 hPa. In addition to the temperature relaxation a Rayleigh damping is applied to the low-level winds to mimic boundary-layer friction. The motivation for the use of this setup is to allow for a state of the atmosphere featuring a transient meandering and baroclinic jet with fronts and eastwards moving high and low pressure systems similar to a more realistic day-to-day situation compared to a climatological mean state.

The neglect of all physical parameterizations (radiation, condensation, convection, boundary layer processes etc.) facilitates the interpretation by eliminating complex diabatic processes thereby focusing purely on the nature of the dynamical response. Together with the HS setup we are thus able to discuss the impacts of non-linearity and non-stationarity in an idealized but more day-to-day like setting in contrast to earlier studies utilizing mainly linearizations about a climatological mean winter background state.

The boundary conditions for the hybrid level vertical velocity are $\dot{\eta} = 0$ at the bottom ($\eta = 1$) and at the top ($\eta = 0$) of the model domain. The condition at $\eta = 0$ would allow for reflection of gravity waves from the lid. The impact of this unphysical reflection is minimized in the IFS by increasing the horizontal diffusion in the uppermost model levels linearly with $\log(p)$.

We integrate the model for a time span of 15 days with 60 levels in the vertical using a triangular truncation T159, which roughly corresponds to a 125 km grid spacing. The time increment was set to 3600 s.

4.2.2 Initial conditions

To obtain our initial fields we integrated the IFS with the setup outlined above for one year and use the 3D fields of the pertinent variables from the last time step of the simulation as the initial fields for the integrations presented in this study. The long time span of the integration allows the model to respond and equilibrate to the HS setup yielding a non-linear, zonally asymmetric transient baroclinic state of the atmosphere. Fig. 4.1 illustrates the initial situation by means of potential vorticity (PV) on the 320 isentropic surface as well as zonal wind and geopotential height on 200 hPa and temperature and geopotential height on 850 hPa. The wavy structure of the baroclinic zone between 30 and 60 N/S is clearly evident featuring PV streamers as well as areas with rather zonal orientation, e.g. between 100° and 180° E in the southern hemisphere. The zonal speed of the jet varies between 20 and 45 m s^{-1} which corresponds to realistic jet velocities. However, the stronger zonal and meridional asymmetries present in reality can yield even higher maximum jet speeds. Comparing the geopotential heights at 200 and 850 hPa (not shown) there are regions with a typical westward phase tilt with height (e.g. 60° E in the northern hemisphere) indicating growing baroclinic waves, whereas most of the mid-latitude baroclinic zone appears to be in a rather mature stage of baroclinic development (vertical aligned phase lines). There are also regions of strong temperature advection evident in Fig. 4.1c indicating the existence of fronts and frontal dynamics.

Thus the initial state of the atmosphere exhibits some of the complexities of a day-to-day situation in reality with strong asymmetries in the zonal directions and is of non-steady character. This richness in structure of our initial fields contrasts the much smoother and more zonal structures within climatological mean states which have been used in similar studies before. The incentive of using a much more complex initial state is to increase the realism of our simulations and to pinpoint dynamical evolutions with applicability to day-to-day weather evolutions in order to illustrate the impact of tropical forcing on a short to medium range weather development and forecast.

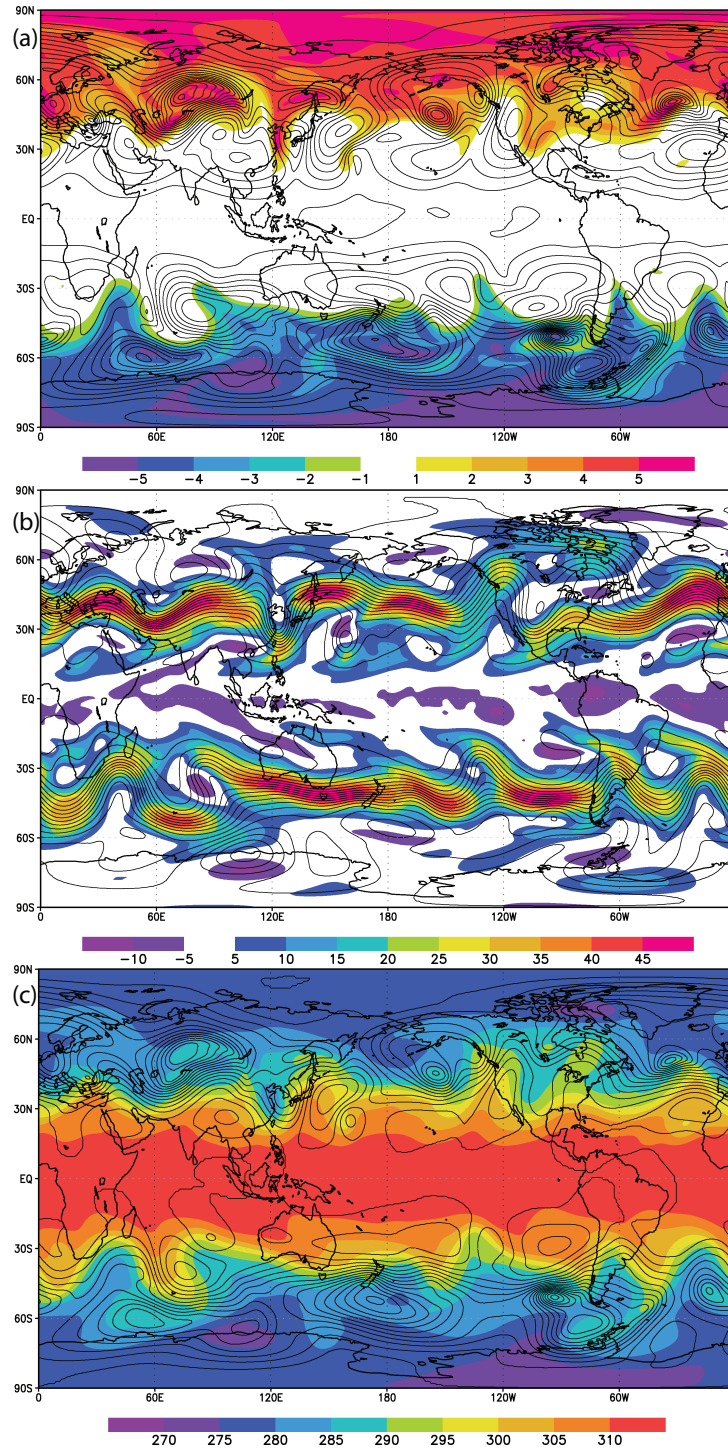


Figure 4.1: Initial fields of potential vorticity [PVU] on the 320 K isentropic surface and surface pressure with contour increment (c.i.) 2.5 hPa (a), Zonal wind speed [m s^{-1}] and geopotential height with c.i. 5 dam at 200 hPa (b) and potential temperature [K] and geopotential height with c.i. 2.5 dam at 850 hPa (c).

4.2.3 Definition of the heating

In addition to the setup lined out above we apply a temperature forcing in the tropical regions to mimic diabatic heating from convection. This heating is applied to all simulations except to one reference experiment which was integrated without the additional heating profile. The specification of our heating

distribution is similar to the ones used by Jin and Hoskins (1995) and Ting and Yu (1998), i.e.

$$\dot{Q} = AV(\eta)H(\lambda, \Phi) \quad (4.1)$$

where A is the amplitude and $V(\eta)$ and $H(\lambda, \Phi)$ are the vertical and horizontal (λ =longitude, Φ =latitude) distribution functions, respectively. The horizontal distribution of the heating is given by

$$H(\lambda, \Phi) = \begin{cases} \cos^2\left(\pi\frac{\lambda-\lambda_0}{2\Delta\lambda}\right)\cos^2\left(\pi\frac{\Phi-\Phi_0}{2\Delta\Phi}\right) & \text{if } |\lambda-\lambda_0| \leq \Delta\lambda, |\Phi-\Phi_0| \leq \Delta\Phi \\ 0 & \text{if } |\lambda-\lambda_0| > \Delta\lambda, |\Phi-\Phi_0| > \Delta\Phi \end{cases}$$

where λ_0 and Φ_0 are the center longitude and latitude of the prescribed heating and $\Delta\lambda$ and $\Delta\Phi$ correspond to the half-width of the forcing in the longitudinal and latitudinal directions, respectively. The standard setting in the study presented here is chosen to be $A = 5 \text{ K d}^{-1}$, $\Delta\lambda = 30$ and $\Delta\Phi = 10$, which is comparable to the heating distributions used by Jin and Hoskins (1995) and Ting and Yu (1998). The sensitivity to the parameters is discussed in section 4.4.5. The center latitude Φ_0 is either 0° N , 15° N or 15° S , whereas 12 different center longitudes λ_0 were investigated for each latitude, encircling the globe with an increment of 30° . The different longitudes are chosen to highlight the sensitivity of the response to the different structures evident in the mid-latitudes. Thus we have 36 experiments with a stationary tropical heating.

The vertical heating distribution takes the form

$$V(\eta) = \sin(\pi\eta) \quad (4.2)$$

which has a maximum at $\eta = 0.5$ and reduces to zero at $\eta = 0$ and $\eta = 1$, i.e. the top and the bottom of the model domain. Thus the maximum is at about the same height as in Ting and Sardeshmukh (1993) ($\sigma = 0.5$) but lower than in Jin and Hoskins (1995) (400 hPa). Matthews et al. (2004) investigated the sensitivity of the response to the height of the maximum tropical heating and found that the amplitude of the response decreases for lower heights of maximum heating. This indicates that the results presented here might underestimate the amplitude of the response compared to more realistic tropical forcing which was shown to maximize around 400 hPa (Matthews et al., 2004). However, the sensitivity of the vertical heating distribution is out of the scope of the study presented here.

For the moving forcing we only investigate the response with $\Phi_0 = 0$ and assume the corresponding λ_0 to be a function of time resembling a speed of 5 m s^{-1} which is comparable to the speed of the MJO signal (Salby et al., 1994; Hendon and Salby, 1994; Zhang, 2005). All other parameters are the same as for the standard setting. Thus we have 12 experiments with a moving tropical heating.

Regarding the similarity of our forcing to the MJO one should keep in mind that whilst we prescribe a tropical heating to mimic the convective active part of the MJO in the Indian and Pacific Ocean, the MJO is a global phenomenon and the perturbations related to it span the entire globe. Thus by solely prescribing a tropical heating the features simulated in our experiments will not be able to reproduce a real MJO circulation.

4.3 Method

We use the difference between the 36 forced model runs with a stationary forcing or the 12 runs with a moving forcing to the model run without the tropical heating for analyses in order to pinpoint the impact

of the forcing on the time evolution. The strategy for this has particularly two aspects. First, the unforced run can be seen as a background state on which the tropical heating generates a response permitting a direct dynamical interpretation. The second aspect can be seen as an immediate application to medium range weather prediction. Since the forecasts of tropical convection, especially the onset and evolution of the MJO in today's numerical weather prediction models are still rather poor (Hendon et al., 2000; Zhang et al., 2006) the difference between the model simulations indicates the possible impact of a missed or incorrectly forecasted event of tropical heating like the MJO on a forecast.

From the large variety of variables the discussion of the results concentrates on the difference of geopotential height on different pressure levels. This choice is especially motivated by the frequent use of geopotential height in the analysis of teleconnections and in weather forecasting. Furthermore, the analysis of the 200 hPa isobaric surface allows for the investigation of the evolution along the tropopause region throughout a large fraction of the globe. An interpretation of PV on an isentropic surface is hampered by the fact that the isentropic surfaces dip down significantly towards the equator where the forcing is usually centered. In addition to the difference in the geopotential height the absolute value of the total gradient of PV on 200 hPa is evaluated where the thick contour line on the plots indicates the 4 PVU per 1000 km value. We have chosen PV on an isobaric surface here instead of an isentropic one in order to be consistent with the analysis of the difference in the geopotential height fields. We will refer to the region enclosed by the contour as the mid-latitude wave guide. This nomenclature is motivated by Rossby wave theory. Rossby waves can only propagate on non-zero PV gradients and can become trapped along sharp gradients in PV.

We also present an analysis indicating the dependence of the downstream extent of the perturbation on the distance of the forcing from the wave guide. This is motivated by Schierz et al. (2004) who showed that the impact of a balanced perturbation on a PV discontinuity is determined by the distance of the perturbation to the PV discontinuity as well as its amplitude, or in other words by the magnitude of the circulation of a balanced vortex in the vicinity of the wave guide. In the following we define the time of the first impact of our tropical forcing on the wave guide (t_{fst}) as the time when the absolute value of the difference of the geopotential height on 200 hPa in the latitudinal belt between 30-60 N/S exceeds 2 dam for the northern/southern hemisphere, respectively. For this time span we define a mean and a minimum distance of the wave guide to the center position of the forcing for each hemisphere. The minimum distance is defined as the minimum great circle distance between (Φ_0, λ_0) and the closest location on the sphere where the absolute PV gradient on 200 hPa exceeds 4 PVU per 1000 km from $t = 0$ until t_{fst} , whereas the mean distance is defined as the average of the minimum distances from $t = 0$ until t_{fst} . Furthermore we define the distance travelled by the perturbation along the wave guide by detecting the absolute value of the difference of geopotential height exceeding a threshold value of 2 dam within the latitudinal belt of 30-60 N/S and looking for its rhomboidal distance to $(\Phi = \pm 45^\circ, \lambda_0)$ to define the distance travelled in the northern/southern hemisphere.

4.4 Response to stationary heating

In the following we present three case studies highlighting the nature of the response to the tropical forcing that is inherent in all simulations. The three cases were chosen because they feature significant differences between each other and yet are recurring features of many simulations.

4.4.1 Time evolution

Forcing centered at 15° N, 120° E

Figs. 4.2a,b,c,d show day 3, 5, 7 and 10 of the experiment with the forcing centered at 15° N and 120° E. The impact of the heating is evident as a positive geopotential height perturbation at the location of the forcing by day 3. There are also intrusions into the equatorial region as well as the mid-latitudes. By day

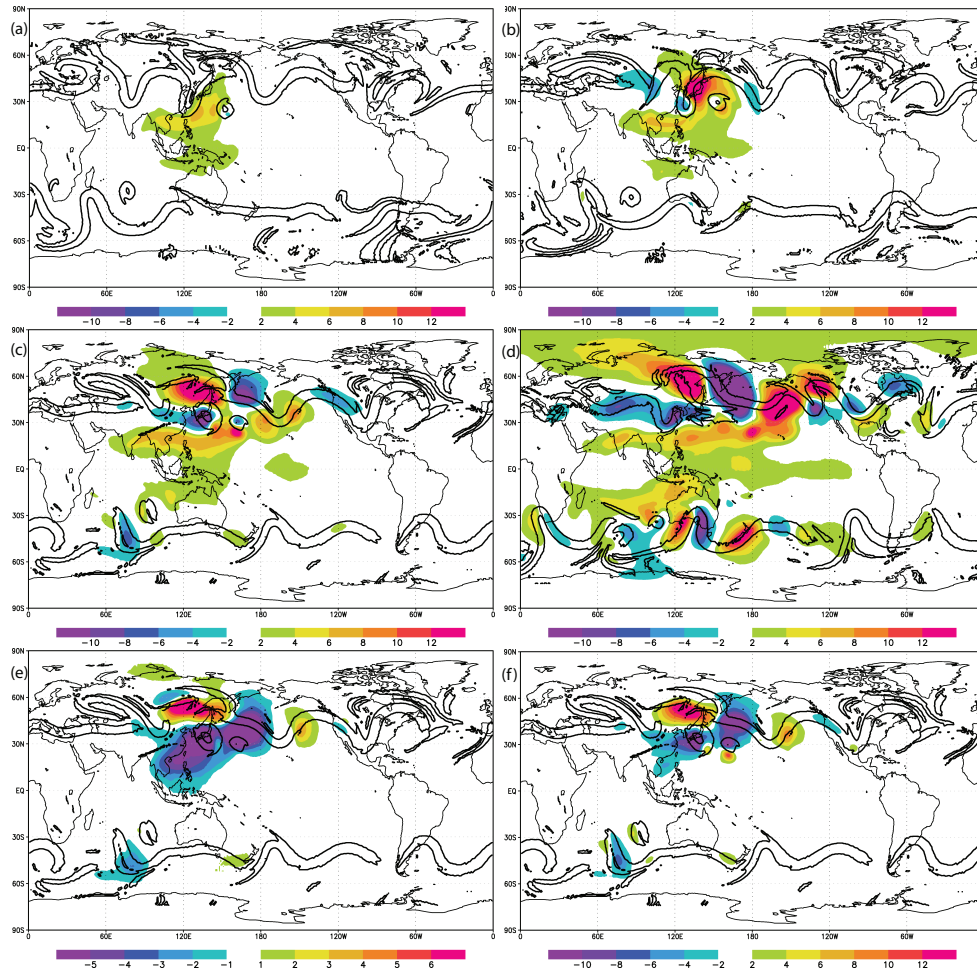


Figure 4.2: Difference in geopotential height between forced minus unforced model run (see text for explanation). Panels (a,b,c,d) are on 200 hPa, (e) on 850 hPa and (f) on 500 hPa. Forcing (5 K d^{-1}) is centered at 15° N and 120° E . Thick contour indicates potential vorticity gradient on 200 hPa exceeding 4 PVU per 1000 km. The different panels correspond to day 3 (a), day 5 (b), day 7 (c,e,f) and day 10 (d).

5 a wave train starts to develop along the PV wave guide in the northern hemisphere, and it subsequently extends downstream. In the southern hemisphere it takes 5 days before the response is evident along the PV wave guide and it too subsequently extends downstream. An eastward propagating Kelvin-like wave response is also evident along the equator at day 10.

Forcing centered at 0° N , 150° E

The second case presented for the stationary forcing is the experiment with the forcing centered at 0° N and 150° E (Fig. 4.3). After three days the typical Matsuno-Gill (Matsuno, 1966; Gill, 1980) response to a stationary equatorial heating is evident featuring the eastward propagating Kelvin wave and the westward propagating Rossby wave couplet. The response differs from the idealized analytical solutions due to non-linearity and the non-uniform background state. By day 5 the influence of the forcing in the northern hemisphere reaches the PV wave guide and proceeds to trigger a downstream development along the same wave guide which becomes clearly evident at day 7. On day 7 there is also a downstream development evident in the southern hemisphere which is also triggered by a lateral propagation towards the southern hemisphere wave guide. By day 10 distinct wave trains along the PV wave guide are evident in each hemisphere with a significant northward intrusion of a negative perturbation in the northern hemisphere around 150° E . The Kelvin wave propagated around 200° along the equator corresponding

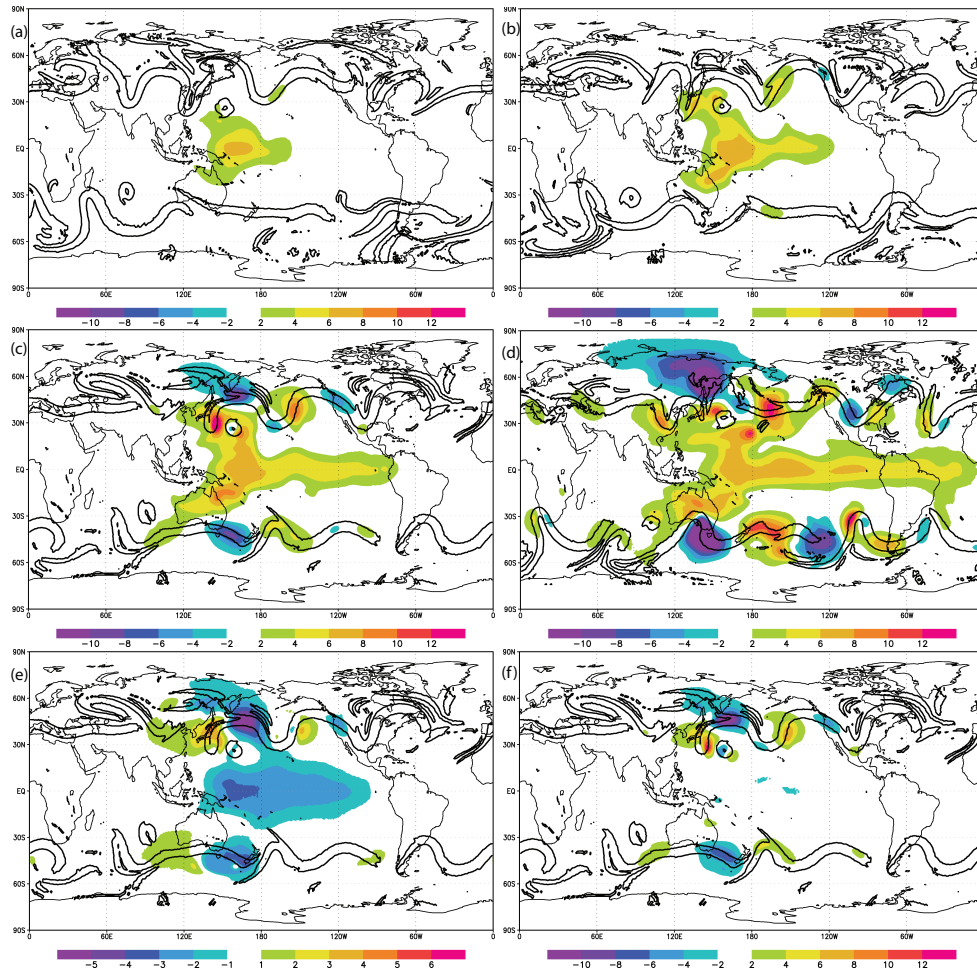


Figure 4.3: Same as Fig. 4.2 but for forcing (5 K d^{-1}) centered at 0° N and 150° E .

to a phase speed of about 25.8 m s^{-1} . It is interesting to note that the wave train along the NH wave guide reaches as far downstream of the center position of the forcing as the Kelvin wave even though the mid-latitude perturbation was initiated a few days after the Kelvin wave. This indicates a higher group velocity of the perturbation along the wave guide compared to the phase velocity of the Kelvin wave.

Forcing centered at 0° N , 30° E

Figs. 4.4a,b,c,d show day 3, 5, 7 and 10 of the experiment with the forcing centered at 0° N and 30° E . The typical Matsuno-Gill (Matsuno, 1966; Gill, 1980) response to stationary equatorial heating is again evident after 3 days featuring the east-ward propagating Kelvin wave and the Rossby wave couplet to the west. At day 5 a perturbation is initiated along the southern hemisphere wave guide in the proximity of the forcing, which subsequently develops downstream (see figures for day 7 and 10). The response along the northern hemisphere wave guide is very weak and is only evident from day 5 onwards. Comparing the structure of the wave guides in the different hemispheres in the vicinity of the forcing a significant excursion of the wave guide towards the tropics is evident in the southern hemisphere, whereas the wave guide in the northern hemisphere is more distant to the forcing and exhibits a less wavy structure at the longitude of interest. The amplitude of the response in the southern hemisphere by day 10 is very large compared to the northern hemisphere and in fact compared to the two case studies presented above. Thus despite the parity of the tropical heating in the different experiments the response can vary significantly due to the relative position of the forcing to the wave guide as well as the structure and character of the wave guide itself.

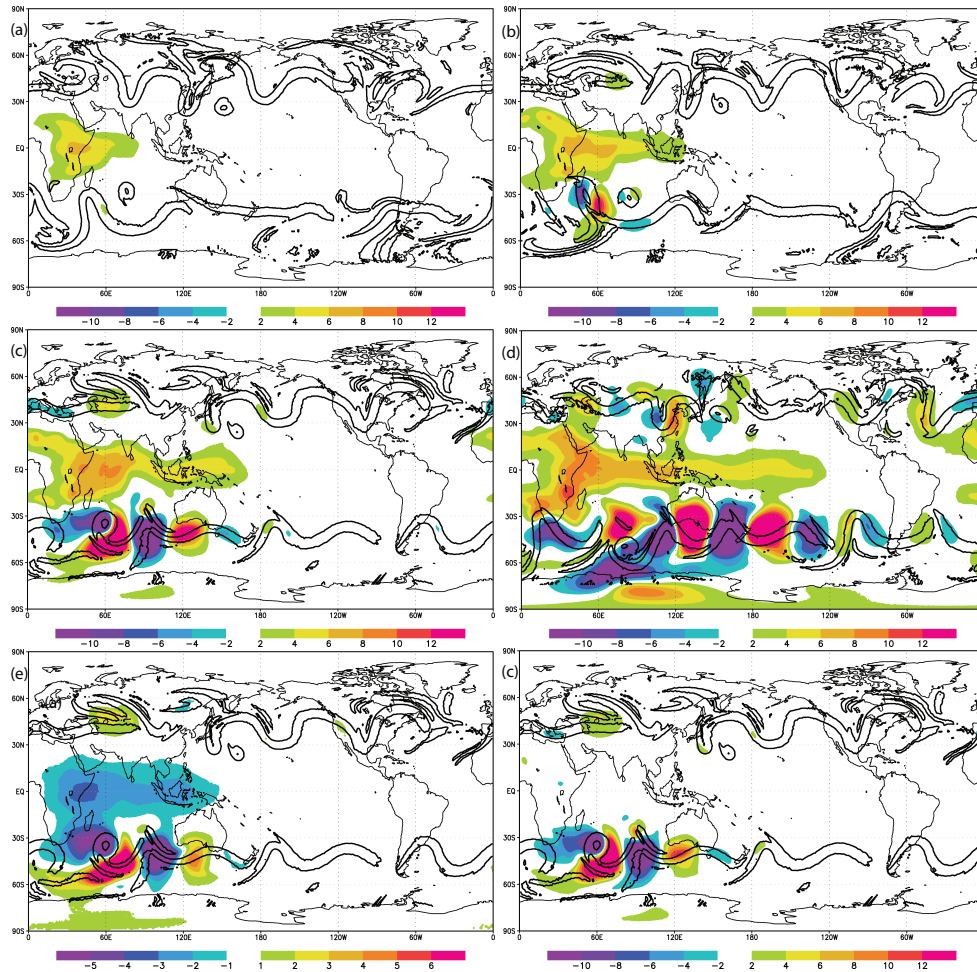


Figure 4.4: Same as Fig. 4.2 but for forcing (5 K d^{-1}) centered at 0° N and 30° E .

Hovmöller diagrams

Fig. 4.5 summarizes the horizontal time evolution of the response along the mid-latitude belt by showing Hovmöller (1949) diagrams of geopotential height averaged between $30\text{--}60 \text{ N/S}$ for the northern (NH)/southern hemisphere (SH) from day 0 until the end of time integration at day 15 for the three case studies presented above. Figs. 4.5a,b show the development for the NH (a) and the SH (b) hemisphere for the first experiment discussed above with the heating situated at $15^\circ \text{ N } 120^\circ \text{ E}$. The disparity in the onset and evolution of the response in the different hemispheres is clearly evident with an earlier initiation of a perturbation along the wave guide with subsequent downstream development in the northern hemisphere. The tilt of the phase lines indicates an eastward phase speed of the perturbations ($c \approx 9 \text{ m s}^{-1}$). However, there is a couple evident in the perturbations from day 7 onwards which is stationary centered about 180° E . The pattern remains stationary for around 6 days before the phase tilt indicates an eastward progression. From Figs. 4.5a,b we can also infer the group velocity of the perturbations propagating along the wave guide by inspecting the inclination of the wave train in the diagram where the wave train encircles the latitudinal belt within about 11 days yielding a group velocity of $c_g \approx 30 \text{ m s}^{-1}$. This value of the group velocity is in fact very close to but smaller than the mean zonal wind speed averaged along the wave guide in the simulations.

Fig. 4.5c,d shows the diagrams for the NH/SH for the experiment with the heating located at $0^\circ \text{ N } 150^\circ \text{ E}$. The picture is less clear compared to the previous case. However, in the NH a perturbation is evident around day 4 and 6 and it subsequently develops downstream. In the southern hemisphere the response along the wave guide is initiated around day 6 consistent with the earlier discussion.

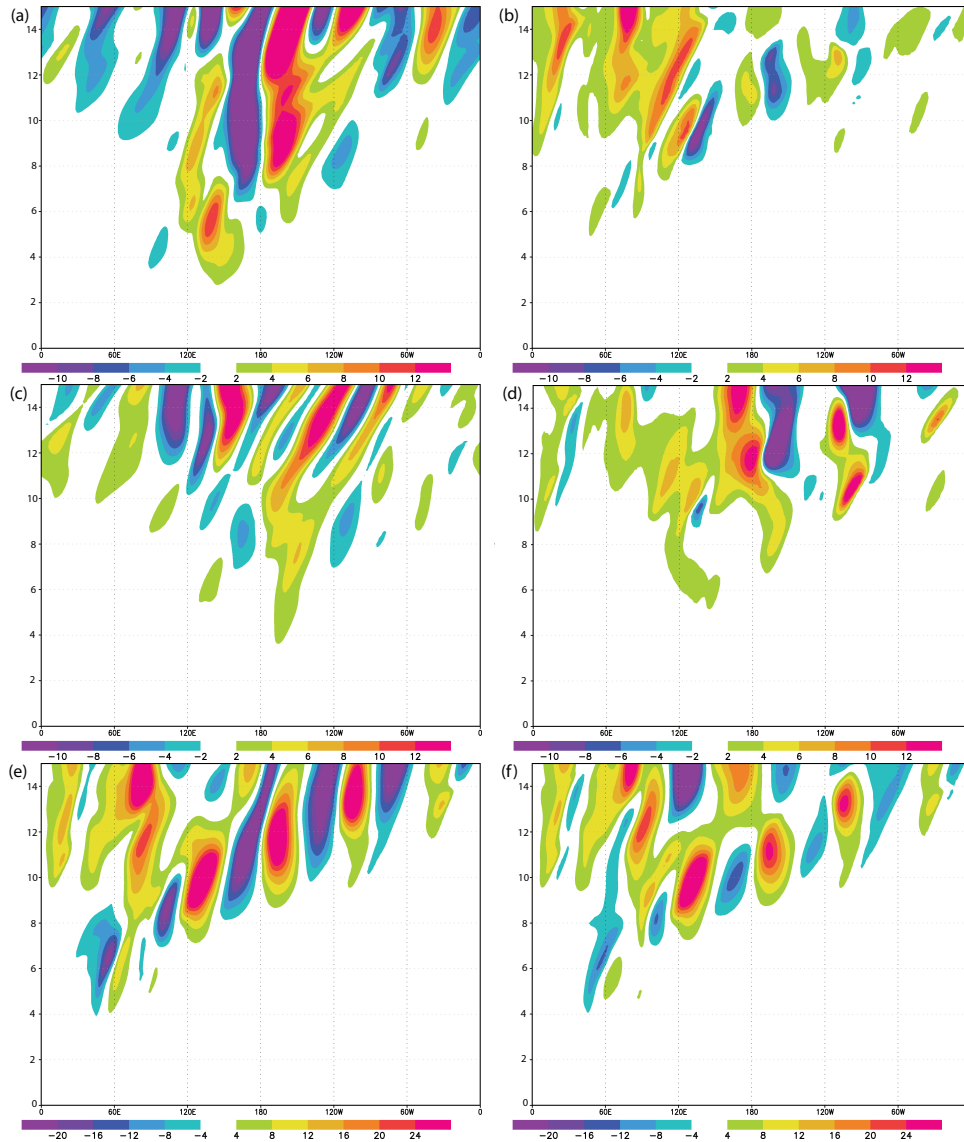


Figure 4.5: Hovmoeller diagrams for difference in geopotential height averaged over 30-60 N (NH) or 30-60 S (SH) at 200 hPa for forcing (5 K d^{-1}) centered at 15° N and 120° E (NH) (a), 15° N and 120° E (SH) (b), 0° N and 150° E (NH) (c), 0° N and 150° E (SH) (d), 0° N and 30° E (SH) (e) and moving forcing starting at 0° N and 30° E (SH) (f).

The Hovmöller diagram for the SH of the experiment with the tropical heating centered at 0° N 30° E is shown in Fig. 4.5e. The initiation of the perturbation on the wave guide as well as its downstream development are clearly evident. Compared to the other experiments discussed above the response is the most clear-cut. The phase and group velocities inferred from the plot are more or less the same as for the first case presented ($c \approx 9 \text{ m s}^{-1}$, $c_g \approx 30 \text{ m s}^{-1}$).

For all experiments presented in Fig. 4.5 the quasi-linear nature of the geometry in the response appears to hold up to about day 12. Afterwards the difference between the forced and un-forced run is of global nature and it becomes difficult to draw a concise picture of the impact of the tropical forcing on the flow evolution. However, it is interesting to note, that the main difference between the forecasts remains more or less confined to the NH and SH wave guides.

4.4.2 Vertical structure

Panels (e) and (f) in Figs. 4.2, 4.4 and 4.4 show the difference in geopotential height on 850 and 500 hPa at day 7 of time integration and are complementary to panel (c) for 200 hPa in the respective figures. For all experiments the baroclinic structure of the tropical response to the forcing is evident, resembling the first baroclinic mode with a reversal in sign of the perturbation between the upper and lower levels.

Fig. 4.6 shows the time evolution of the response with the forcing centered at 0° N 30° E by means of vertical cross-sections of the difference in geopotential height (shaded) and temperature (contour) along 45° S. At day 3 the first response appears at upper levels and then subsequently becomes evident downstream. The response at day 7 and 10 is quasi-barotropic from 100 to 500 hPa before the difference in geopotential height tilts westward with increasing height in contrast to the the difference in temperature which tilts in the other direction. This phase tilt is typical for growing baroclinic waves (e.g. Eady, 1949) and downstream development (Simmons and Hoskins, 1979; Chang, 1993). It should be noted that the perturbation in geopotential height maximizes near the tropopause at 200 hPa, which is also the level of maximum jet speed. Above 500 hPa the perturbations in temperature and geopotential are aligned where positive/negative perturbations in geopotential height are accompanied by negative/positive temperature perturbations above 250 hPa and positive/negative temperature perturbations below. This feature is in accordance with the thermal wind relation of geostrophically balanced flow.

The development in time also indicates that the perturbation in geopotential height is first generated at upper levels and then penetrates downwards and downstream in time, which is in accordance with the modeling work of Simmons and Hoskins (1979) and the analysis of downstream development presented by Chang (1993). However, the tilt of the phase with height of geopotential height and temperature is smaller and only limited to levels below 500 hPa in our study contrasting the analysis presented by

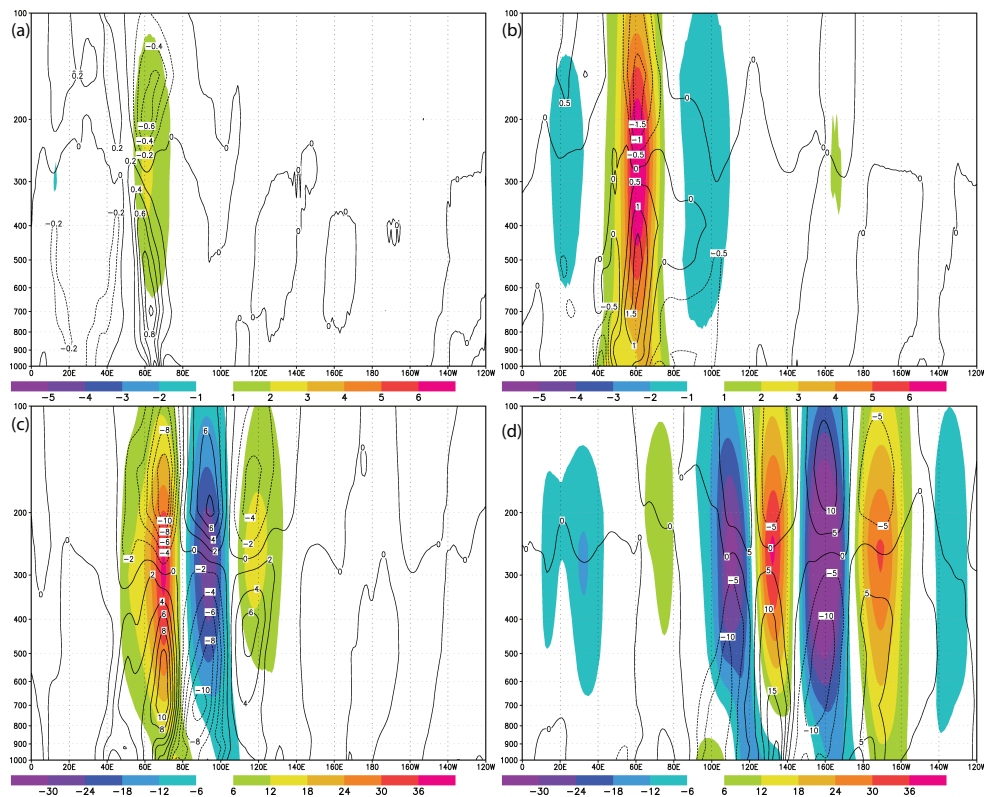


Figure 4.6: Vertical cross-section of difference in geopotential height [dam] (shaded) and difference in temperature [K] (contour) for forcing (5 K d^{-1}) located at 0° N and 30° E. Panels are for day 3 (a), 5 (b), 7 (c) and 10 (d), respectively.

Chang (1993) where the tilt is evident throughout the entire troposphere at a slightly higher angle. This is basically due to the nature of baroclinic waves in the HS setup which was confirmed by looking for the typical vertical tilt of the phase lines in the baroclinic zone in the unforced simulation.

4.4.3 Extent of perturbation versus distance to wave guide

One of the key features evident in the case studies presented above and inherent to all experiments is the wide spread in the onset time of the response along the wave guide as well as its downstream extent and amplitude at a particular time. This raises the question of the salient sensitivities determining these differences. We already pointed out that the relative distance of the tropical heating to the wave guide plays a crucial role in increasing the likelihood of initiating a response in mid-latitudes. In section 4.3 we outlined the method for detecting a perturbation along the wave guide. Our measure for the minimum and mean minimum distance from the forcing to the wave guide as well as the distance propagated by the perturbation in the latitudinal belt between 30 and 60 N/S was also introduced. Using the data for the NH and SH from all 36 experiment we have 72 data points which can be used to compile scatter plots indicating the correlations for different variables.

In Fig. 4.7a the dependence of the time of first detection is plotted against the mean and minimum distance to the wave guide. The alignment of the data points close to the linear fitted curve is quite remarkable indicative of a strong relationship between the two variables with earlier detection for a closer proximity of the forcing to the wave guide. Fig. 4.7b shows the maximum of the absolute amplitude of the response in geopotential height at 200 hPa at day 5 and 7 versus the time of first detection. Again a clear relationship is evident with higher amplitudes for an earlier first detection. This basically denotes that the perturbations are growing in time along the wave guide. Note that the data points for day 5, especially for higher amplitude perturbations, are much closer to their fitted curve than for day 7 pinpointing that the perturbations have a tendency to non-linear growth in some experiments after 5 days of time integration.

Fig. 4.8a/b shows a scatter plot for the distance travelled by day 5/7 versus the minimum and the mean minimum distance of the forcing to the wave guide. Both panels indicate a relationship between the two measures of the distance to the wave guide and the distance propagated by the perturbation, with a further downstream extent of the perturbations for day 5 and 7 for smaller distances of the wave guide to the forcing. The downstream reach of the perturbation is increased for day 7 by about 2000-3000 km, which can be explained by the group velocity of the perturbation along the wave guide pointed out above.

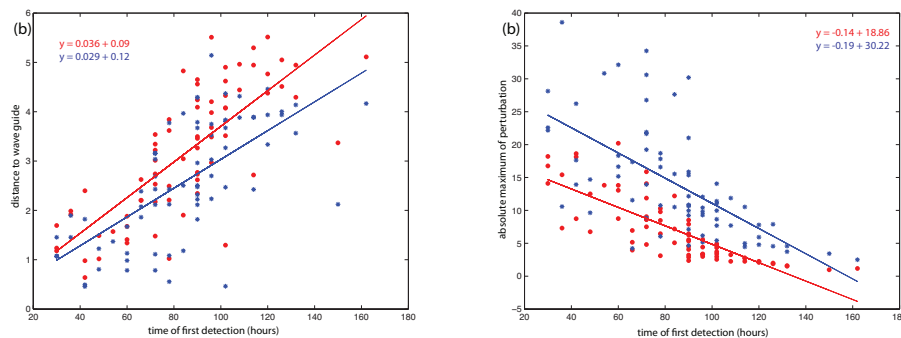


Figure 4.7: (a) Scatter plot of time [hours] (first detection of perturbation in geopotential height at 200 hPa between 30-60 N/S) versus minimum (blue) and mean minimum (red) distance (in 1000 km) to PV wave guide until first detection (see text for details). (b) Scatter plot of time [hours] (first detection of perturbation in geopotential height at 200 hPa between 30-60 N/S) versus maximum absolute value of perturbation in geopotential height [dam] at 200 hPa at day 5 (blue) and day 7 (red). Best fitted linear curves are overlaid.

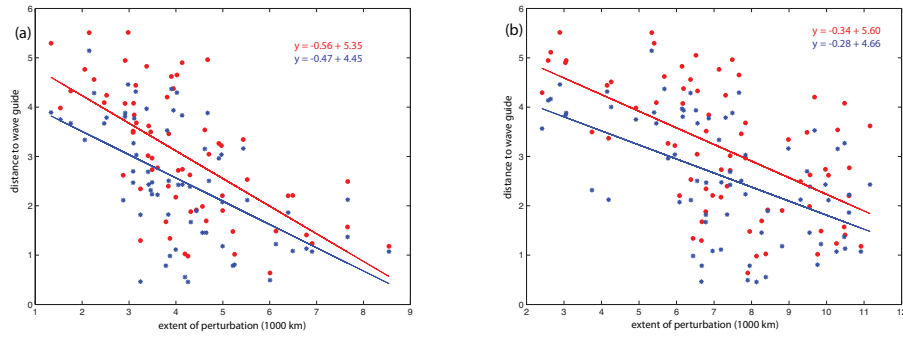


Figure 4.8: Scatter plot of distance (in 1000 km) of perturbation in geopotential height at 200 hPa travelled between 30-60 N/S until day 5 (a) and day 7 (b) versus minimum (blue) and mean minimum (red) distance (in 1000 km) to PV wave guide until first detection (see text for details). Best fitted linear curves are overlaid.

It is interesting to note that the differences between the two measures of the distance to the wave guide, i.e. minimum and mean minimum until first detection, are not very large. From Fig. 4.8 it is also evident that sometimes the spread in the distances travelled by the perturbation in the mid-latitudes for given distances to the wave guide is rather large. This fact can be attributed to the different times of first detection (see Fig. 4.7a), which vary between 30 h and 161 h with a mean value of 88.5 h. Since the group velocity is comparable in all experiments, an earlier initiation of a perturbation allows for a further downstream extent in time compared to a perturbation initiated at a later time.

In Fig. 4.9 the relationship between the maximum absolute amplitude of geopotential height on 200 hPa and the minimum and mean minimum distance to the wave guide is illustrated for day 5 and 7. Again a clear relationship can be inferred between the variables pinpointing higher amplitudes for reduced distances of the forcing to the wave guide.

In summary the key parameter determining the onset time, amplitude and downstream extent at a given time of the perturbation is the relative distance between the forcing and the mid-latitude wave guide. Since all experiments generally never feature the propagation of a wave out of the tropics towards the wave guide the most-plausible explanation for the initiation of the perturbation along the jet is the distant interaction of a vortex with a PV discontinuity as depicted by Schwierz et al. (2004).

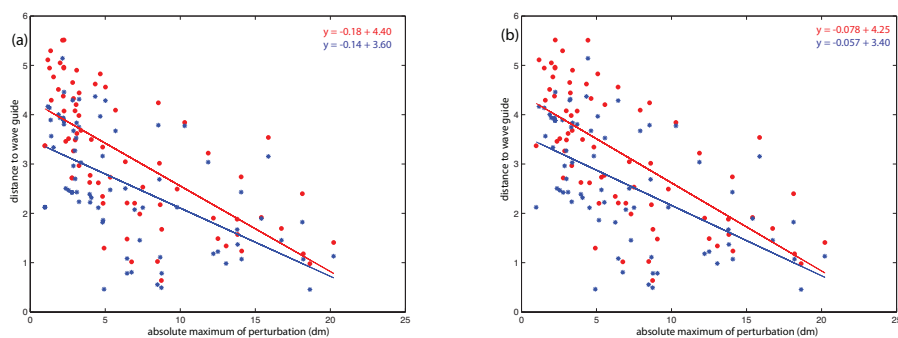


Figure 4.9: Scatter plot of maximum absolute value of perturbation in geopotential height [dam] at 200 hPa between 30-60 N/S until day 5 (a) and day 7 (b) versus minimum (blue) and mean minimum (red) distance (in 1000 km) to PV wave guide until first detection (see text for details). Best fitted linear curves are overlaid.

4.4.4 Response pole-ward of wave guide

Earlier studies investigating the stationary response to a tropical heating pointed out the evidence of a stationary Rossby wave train with energy transmission along a ray path resembling a great circle pole-ward out of the tropics. These stationary Rossby wave patterns are often thought to be the cause for the PNA teleconnection pattern (e.g. Lim and Chang, 1983; Ting and Held, 1990; Ting and Yu, 1998). Jin and Hoskins (1995) and Matthews et al. (2004) showed that these stationary patterns also evolve in non-stationary linear models within the first 15 days of time integration. However, comparing the large scale wave response evident in their simulations to our results we find no equivalent evident in our experiments.

Inspecting the response at day 10 for the three cases presented above (Figs. 4.2d, 4.3d, 4.4d) there is invariably a perturbation evident pole-ward of the wave guide. However, the response does not feature the characteristics of a Rossby wave propagating along a great circle indicating that the cause for the perturbation in the geopotential height is most-likely not due to a Rossby wave propagating through the wave guide. In fact the perturbation for the first two cases can mainly be attributed to an enhanced pole-ward excursion of an existing trough.

However, the significant pole-ward perturbation in the SH in Fig. 4.4d around 90° E is not due to a pole-ward shift of the trough near the forcing. Comparing PV on 320 K (Fig. 4.10) between the unforced and forced model run, the pole-ward response in geopotential height in Fig. 4.4 can be related to an intrusion of tropospheric PV into the higher latitudes which is absent in the unforced experiment. This evolution is strongly linked to a wave-breaking in the forced run at day 10 around 60° S and 90° E with a PV filament subsequently progressing southwards. The filament becomes cut off around day 14

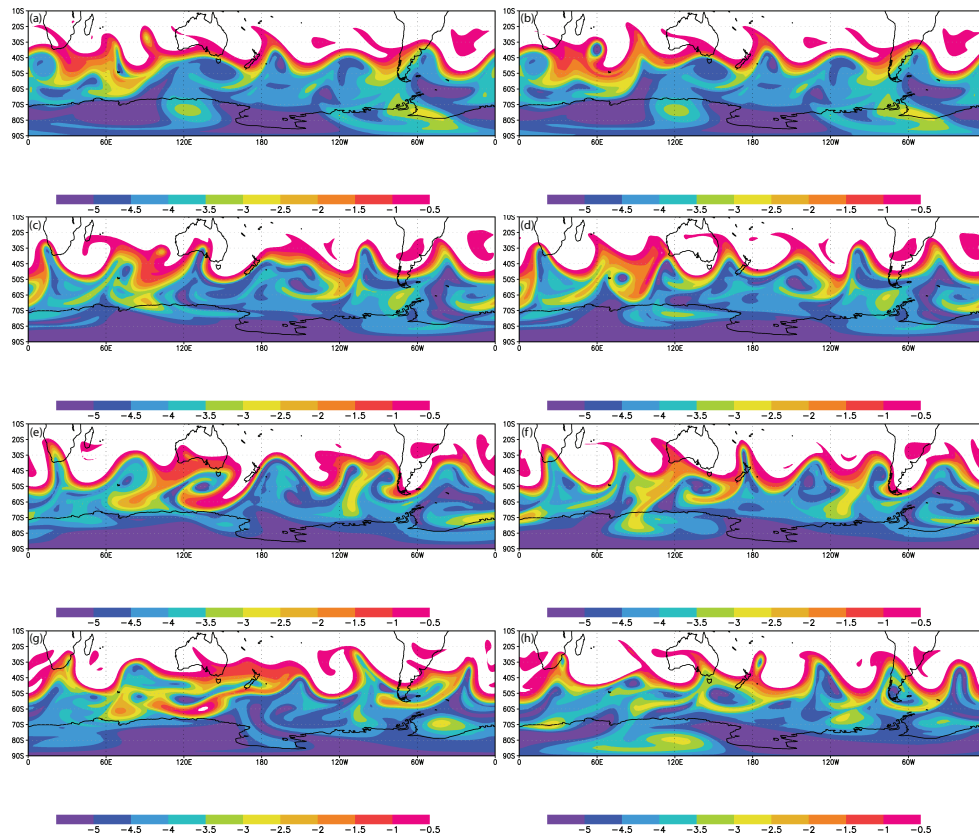


Figure 4.10: PV [PVU] on 320 isentropic surface for the unforced experiment (a,c,e,g) and the experiment with the forcing centered at 0° N 30° E (b,d,f,h) at day 7 (a,b), day 10 (c,d), day 12 (e,f) and day 14 (g,h).

resembling a closed PV perturbation at higher latitudes. Due to the high degree of non-linearity inherent in the wave-breaking producing this pole-ward response it seems implausible to explain the response via stationary linear Rossby wave propagation.

4.4.5 Sensitivity to the amplitude and size of the forcing

Several experiments were repeated with different amplitudes and reduced horizontal extent of the forcing in order to pinpoint the sensitivity of the results described above with the standard forcing outlined in section 4.2.3.

Enhancing or reducing the amplitude of the tropical forcing does not significantly impact on the pattern of the response. An analysis by manual inspection yields that the shapes of the perturbations in the geopotential height field are almost unaltered compared to the standard setting. However, we find a quasi-linear relationship between the amplitude of the perturbation and the maximum heating, where doubling/halving the magnitude of the heating doubles/halves the amplitude of the tropical perturbation as well as the amplitude of the response along the wave guide. This is in accordance with the findings of Schwierz et al. (2004) who showed that the relative magnitude of a vortex reaching the wave guide determines the amplitude of the response. Regarding the linearity with respect to the amplitude of the forcing a similar relationship was also found by Lin and Derome (2004) who investigated the non-linear extra-tropical response to a tropical heating perturbation resembling the ENSO signal.

Interestingly a change in the horizontal distribution of the forcing has a similar effect, i.e. the structures along the wave guide are almost unaltered (checked by manual inspection), whereas the amplitude decreases for smaller forcings. Halving the zonal and meridional extent of the heating (which is equivalent to halving the effective radius) results in a response with half the amplitude compared to the standard setting. The reason for this dependency is most-likely twofold. First, a reduction in the size of the forcing increases the distance to the wave guide, which according to Schwierz et al. (2004) will reduce the amplitude of the response along the wave guide. Second, the smaller area of the forcing projects onto a spectrum with higher zonal wave numbers. Thus the amplitudes of the larger wave components, which primarily impact on the wave guide, are reduced.

4.5 Response to non-stationary heating

The results obtained with a moving heating distribution are designed to mimic some aspects of the impact of a migratory tropical convective event such as the MJO. However, one should bear in mind the simplifications inherent in the chosen model setup neglecting any diabatic processes, which of course might change the response in reality. 12 experiments were carried out with different starting locations of the forcing along the equator. In the following we will present one case study pinpointing similarities and differences to a similar experiment but carried out with a stationary forcing.

Some interesting questions regarding the difference to the stationary heating are raised due to the migratory nature of the tropical heating. First, the tropical response which for a stationary forcing is depicted by the Matsuno-Gill response might feature different phase speeds in the zonal directions. Second, there is the possibility of a Doppler shift in the frequency and thus phase speed of the perturbations along the wave guide yielding a further downstream extent compared to the stationary heating. Another aspect is the maintenance of the forcing along the wave guide. For a stationary response one would expect a decreased amplitude in the response for a non-steady forcing. However, as pointed out in the previous section on the stationary heating, the response is always of transient nature despite the stationarity of the forcing.

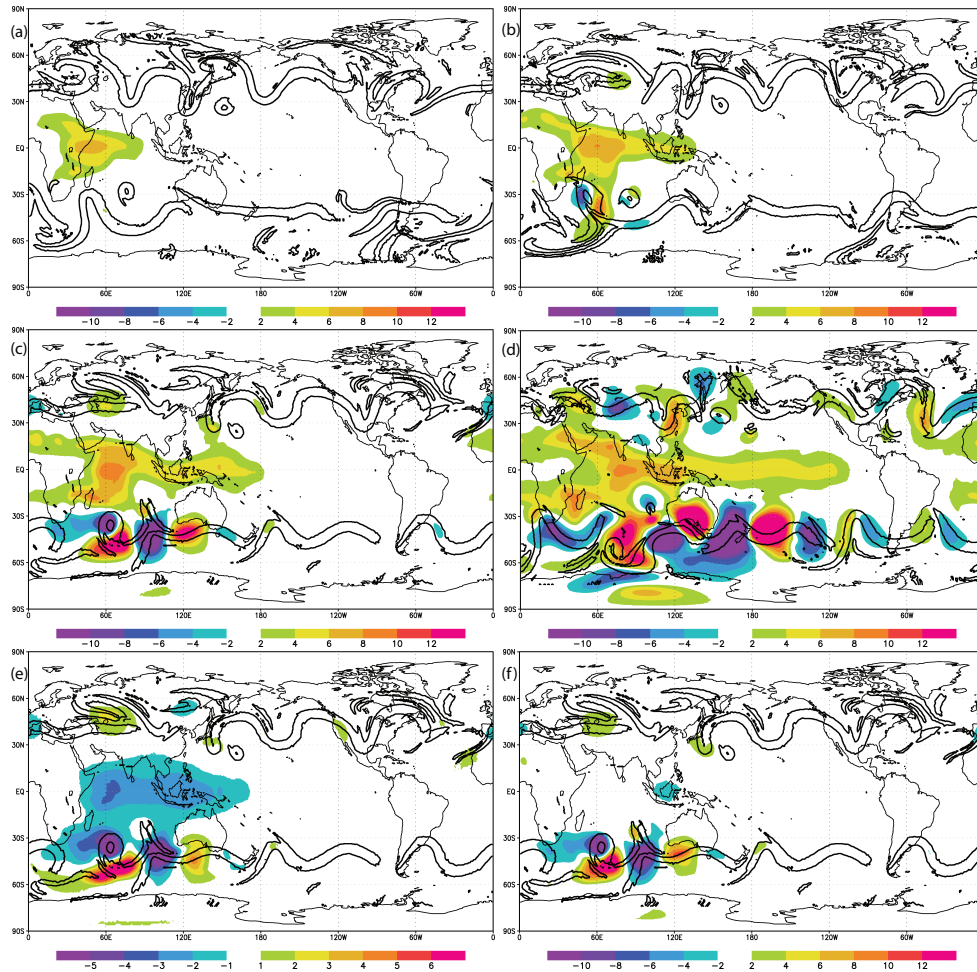


Figure 4.11: Same as Fig. 4.2 but for moving forcing (5 K d^{-1}) starting at 0° N and 30° E .

4.5.1 Time evolution

Fig. 4.11 shows the same fields as the figures discussed in the previous section for the stationary cases, but now for a translating forcing starting at 0° N 30° (the position for the last case discussed within the results for the stationary forcing). Comparing Figs. 4.11a,b,c to Figs. 4.4a,b,c the response is similar and indeed almost identical for the first 5 days but featuring a reduced amplitude compared to its non-stationary counterpart. The shape of the response along the wave guide is more or less unaffected by the non-stationarity of the tropical heating. However, the tropical response is shifted towards the east, which is illustrated by the new center of the response being around 60° E and a further downstream reach of the Kelvin wave.

After day 5 the heating migrates into an area where it subsequently interacts with a tropical excursion of the wave guide further downstream around 100° E . This interaction yields another perturbation along the wave guide. Due to the large distance from the initial longitude the stationary forcing at 30° E is not able to interact with this tropical intrusion of the wave guide. It is this difference in the interaction with the wave guide between the two simulations which results in the distinct patterns at day 10 (Fig. 4.11d). The downstream part of the perturbation along the wave guide is still more or less identical to its non-stationary counterpart (Fig. 4.4d), but the perturbation along the wave guide closer to the forcing is now modulated significantly, with the negative perturbation in the SH around 100° E being shifted eastwards and the positive perturbation in the SH around 140° E being shifted equator-wards. The perturbation triggered later subsequently interferes with the existing perturbation hampering the dynamical interpretation of the further development.

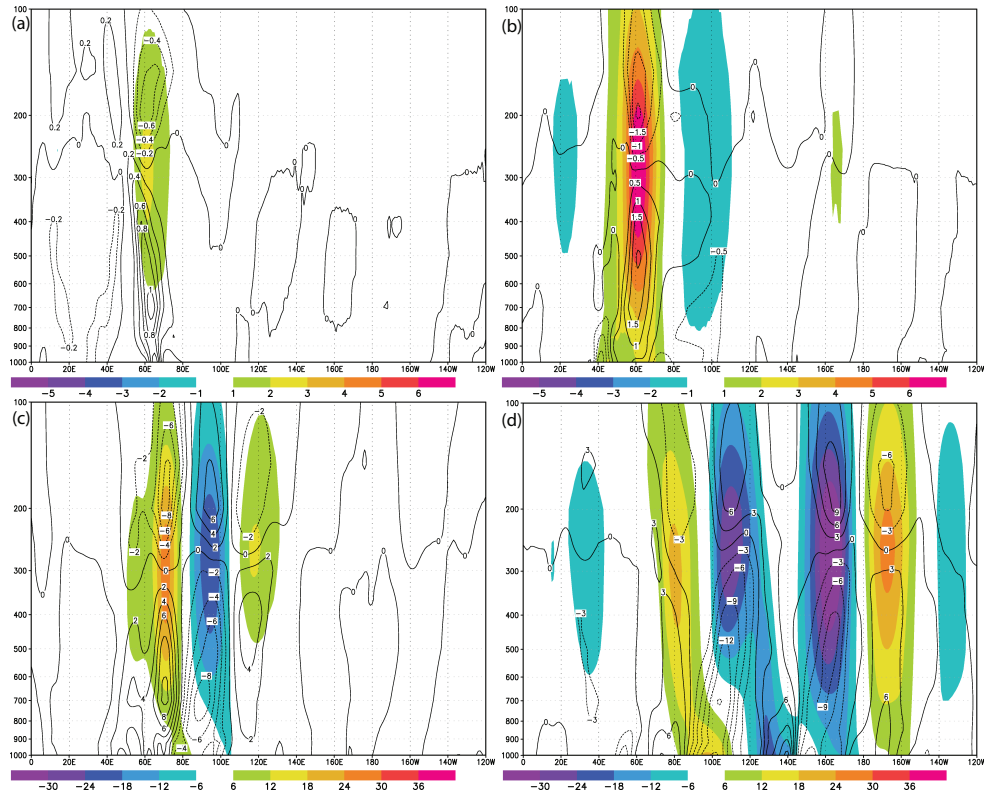


Figure 4.12: Vertical cross-section of difference in geopotential height [dam] (shaded) and difference in temperature [K] (contour) for moving forcing (5 K d^{-1}) starting at 0° N and 30° E . Panels are for day 3 (a), 5 (b), 7 (c) and 10 (d), respectively.

The Hovmöller diagrams in Figs. 4.5e,f clearly illustrate the similarities of the response. There is a large qualitative agreement of the two bottom panels, but it is also evident that the amplitude of the response is reduced for the migratory forcing and almost decays before reaching 0° E at day 15, whereas the response for the stationary forcing maintains its strength. Comparing the initial perturbations around day 5 a reduced initial amplitude for the moving forcing is evident compared to the stationary one. Thus in contrast to the stationary simulation the translating forcing is either not able to maintain the energy supply for the wave train or is not able to create a large enough initial perturbation on the wave guide. Furthermore the interference between the two perturbations triggered along the wave guide might in fact be destructive yielding reduced amplitudes. Assessing the phase and group velocity from the tilt of the phase lines and the angle of the wave train with the x -axis in Figs. 4.5e and f we can infer that the phase as well as the group velocity is unchanged by the moving nature of the forcing ruling out the arguments for a Doppler shifted response.

Comparing the time of first detection as well as the mean and mean minimum distances to the wave guide versus the distance of the perturbation travelled along the mid-latitude belt for the 12 experiments we find almost no differences between the stationary and non-stationary equatorial heating distributions. This indicates that the moving nature of the forcing does not significantly change the character of the first interaction of the forcing with the wave guide.

The similarity between the experiments with a stationary and a moving forcing denotes that it is primarily the first impact of the heating and its footprint on the wave guide which determines the character of the response in the mid-latitudes. In fact since the perturbation is progressing with a group velocity of $\approx 30 \text{ m s}^{-1}$, which is much larger than the speed of the tropical heating, one might expect that the subsequent impact of the moving forcing will always be behind the first perturbation. This explains why the leading edge of the downstream development is almost unchanged compared to the stationary

forcing.

4.5.2 Vertical structure

Inspecting the vertical structure of the response along the wave guide for the moving forcing (Fig. 4.12) we find more or less identical structures compared to the ones presented for the stationary forcing featuring the characteristics of baroclinic downstream development with a maximum perturbation in the upper troposphere. It is only after day 7 that the patterns change significantly around 60-140 E, which can be attributed to the subsequent interaction of the forcing with the wave guide outlined above.

4.6 Discussion

The material presented above highlights the sensitivity of the amplitude and the downstream reach of the response to the relative location of the tropical heating to the mid-latitude wave guide. In the following we will interpret possible dynamical and theoretical explanations for the sensitivity by applying the findings for downstream development (e.g. Simmons and Hoskins, 1979; Chang, 1993; Chang and Yu, 1999; Chang, 1999) as well as the theory of forced interfacial (i.e. at a PV discontinuity) waves on a β -plane discussed by Schwierz et al. (2004).

We showed that the group velocity of the perturbations is always much larger than their phase speed. This was found to be typical for downstream development (Chang, 1993). For neutral non-divergent Rossby waves this behavior can be explained by the dispersion relation of barotropic Rossby waves (Rossby, 1939). However, the view is incomplete if unstable waves exist, such as in our experiments. In contrast to the non-divergent barotropic case the group velocity of the leading wave disturbance is now defined by the fastest growing perturbation (e.g. Pierrehumbert and Swanson, 1995; Hakim, 2003) but its group velocity is also bound by the jet-level wind speed. The latter characteristic is in fact true for all experiments where the perturbation is never progressing downstream faster than the mean zonal wind speed along the wave guide at 200 hPa.

In Figs. 4.2, 4.3, 4.4 and 4.11 there is always a wave packet evident along the wave guide with the maximum amplitude near the forcing and smaller amplitudes at the leading edge. This is also in accordance to wave packet theory in a baroclinically unstable environment with an initially localized disturbance (Pierrehumbert and Swanson, 1995). The structure of the perturbation with the highest amplitude in the center of the wave packet is predicted to bear the properties of the most unstable mode (Simmons and Hoskins, 1979; Farrell, 1983). Comparing the phase tilt in the vertical cross-sections the largest growth tends not to occur at the leading edge but rather some distance into the wave packet. Theory would predict the leading edge to have larger wave numbers than in the middle of the wave packet. However, inspecting the Hovmöller diagrams in Fig. 4.5 we find no evidence for this behavior in the time evolution of particular phase segments.

Further dynamical investigations are needed to determine the ingredients needed to properly predict the group and phase velocities from a three dimensional highly complex atmospheric state. It was stated by e.g. Chang (1999) and Hakim (2003) that we are still lacking a detailed understanding of these properties. Recently developed three dimensional wave activity fluxes (Takaya and Nakamura, 1997a,b) were proven useful to qualitatively indicate the path of wave energy from which phase and group velocity of downstream development can be inferred afterwards (Danielson et al., 2006). Anyhow, we were also able to determine the phase and group velocities directly from the Hovmöller diagrams.

The results presented above indicate that the dynamical mechanism initiating the perturbation along the wave guide is less related to a linear wave packet propagating out of the tropics and then dispersing along the wave guide but is most plausible related to a distant interaction of the wave guide with the tropical circulation generated by the forcing. In fact the linearity of the response with respect to the amplitude of the heating as well as the quasi-linear relationship between the distance of the heating to the wave

guide and the downstream reach of the perturbation make a strong argument for the main mechanism being related to the vortex-wave guide interactions discussed by Schwierz et al. (2004). Thus a vortex at some distance to the wave guide but with a part of its circulation actually reaching the wave guide is sufficient to trigger downstream development along the wave guide. Hence the tropical perturbation does not need to propagate as a wave out of the tropics in order to interact with the mid-latitudes. Indeed in Chapter 2 we demonstrated that stationary Rossby wave propagation through a strongly sheared medium is not feasible. Thus the interaction is mainly determined by the relative distance between the circulation induced by the heating and the wave guide.

4.7 Final remarks

The non-linear response to tropical heating was investigated in a global three dimensional model which was run in the Held-Suarez setup comprising a meandering baroclinic mid-latitude jet in each hemisphere. The forcing always generated a response in the extra-tropics but with its amplitude, structure and time of occurrence being strongly dependent on the distance of the forcing to the wave guide, i.e. the jet stream. A quasi-linear relationship was found between both the minimum and the mean minimum distance of the forcing to the wave guide and the downstream reach of the impact by the tropical heating. The extra-tropical response to the heating was primarily confined to the mid-latitude wave guide. Poleward perturbations were only evident in the case where the forcing generated significant excursions of preexisting troughs and ridges and for wave breaking yielding the intrusion of mid-latitude air into the higher latitudes. Thus the pole-ward response in our experiments is generally not explainable by linear Rossby wave dispersion.

The response along the wave guide always resembles the characteristics of baroclinic downstream development (Simmons and Hoskins, 1979; Chang, 1993; Chang and Yu, 1999; Chang, 1999) with an opposite vertical phase tilt of geopotential height and temperature in the lower troposphere resembling the structure of a growing baroclinic wave (e.g. Eady, 1949). The maximum perturbation in geopotential height is near the tropopause and always precedes the perturbations near the ground in accordance to the modeling work by Simmons and Hoskins (1979) and to the regression analysis presented by Chang (1993). An analysis of the Hovmöller diagrams yielded phase and group velocities of 9 and 30 m s⁻¹, respectively, where the group velocity was found to be close to but still smaller than the mean zonal jet speed along the wave guide.

Since previous studies indicated that the North Pacific mid-latitude wave guide is a region of frequent occurrence of downstream development (e.g. Chang, 1993; Chang and Yu, 1999; Hakim, 2003) it was always tempting to assign the role of triggering these wave trains to the convective activity over the tropical Pacific warm pool area. In fact the results presented here strongly encourage this interpretation. Of course similar arguments apply for other regions on the globe where tropical heating occurs in the proximity of a wave guide such as e.g. the western Atlantic Ocean.

The radius and magnitude of the tropical heating were found to project linearly onto the amplitude of the extra-tropical response indicating that the dynamics involved in the initiation of the first perturbation along the wave guide might be explainable by linear theory. In fact the applicability of a simple model with a balanced vortex impacting on a PV interface at some distance proved very useful in interpreting the results. This implies that the interaction of the tropical heating with the wave guide is dominated by the distant impact of a balanced perturbation in contrast to Rossby waves emerging directly from the tropics and dispersing into the mid-latitudes.

However, some open questions remain. We were not able to produce patterns like the PNA in our simulations which were shown to emerge in similar linear studies with a climatological mean background flow within the first 15 days of time integration. Earlier studies always highlighted the zonal asymmetries of the climatological mean state as one of the key ingredients in order to obtain a pattern similar to the PNA. Since the time mean state of the Held-Suarez setup is zonally symmetric the lack of zonal

asymmetry might in fact explain the deficiency of our experiments to reproduce a pattern similar to the PNA. But there is also the absence of orography and land-sea contrast in our model simulations which in fact might also play a crucial role in interacting with the downstream developing baroclinic wave train and the importance of those interactions in setting up the PNA pattern remain yet to be determined.

Chapter 5

Concluding remarks and Outlook

In the first part analytic solutions were presented for horizontal stationary Rossby wave propagation through linear and parabolic zonal basic states ($\bar{u} = U_0 + \Lambda y$ or Λy^2) utilizing the barotropic, the QGSW and the stratified QG framework. In addition we also discussed analytic solutions for vertical stationary Rossby wave propagation through zonal basic states with a linear and parabolic structure in the vertical ($\bar{u} = U_0 + \Lambda z$ or $U_0 + \Lambda z^2$) for the stratified QG system.

It was shown that the ability of horizontal and vertical stationary Rossby wave propagation decreases for increasing linear or parabolic shear. For large shear the propagation of Rossby waves is inhibited. It was shown that an increase in the zonal and vertical wave numbers decreases the horizontal propagability, and likewise an increase in the zonal and meridional wave numbers decreases the vertical propagability. Numerical simulations performed with a linear barotropic model supplemented the analytic findings. Within the analytic framework we also identified several trapped modal solutions for all basic state profiles except for the parabolic profile in the horizontal ($\bar{u} = \Lambda y^2$). Albeit the academic nature of these modal solutions and their limited applicability to the real atmosphere, their existence illustrates certain issues for idealized model studies. Numerical simulations with similar basic state profiles and boundary conditions ($\Psi = 0$ at $y = 0$ or $z = 0$) can be significantly contaminated by these resonant modes, which might hamper the interpretation of the results.

In the second part the time and space evolution of a global response to a single mountain located at different latitudes in an idealized atmospheric setting with a zonal jet of variable strength in each hemisphere was investigated. In accordance to earlier studies it was found that a constant forcing (i.e. the mountain) always yields a stationary response in the hemisphere in which it is centered and that the response is mainly composed of two wave trains: One along the jet and one crossing the jet into higher latitudes. The concepts of ray tracing of stationary non-divergent barotropic Rossby waves proved to be useful in order to explain the differences in the 3D response. Especially the dependence of the higher latitude response was to a great extent attributable to differences in the latitudinal profiles of the stationary wave number. The three dimensional structure of forced QG stationary Rossby waves was found to account for the difference in the vertical composition of the response along (wave-like in vertical) compared to north of the jet (quasi-barotropic). Furthermore it was shown that a change in the latitude of the mountain leads to a phase shift of the stationary response north of the jet, which can be attributed to the different path lengths of the rays of the waves.

A remarkable finding of this study is the non-stationarity of the response in the hemisphere without the mountain which is in fact explainable by barotropic Rossby wave theory. Furthermore the concepts of wave refraction still hold for waves with a phase speed unequal zero. However, the generation of the non-stationary Rossby waves by a stationary mountain requires further analysis.

In the third part of the thesis the non-linear response to tropical heating was investigated in a global three dimensional model which was run in a setup comprising a meandering baroclinic mid-latitude jet in each hemisphere. The forcing always generated a response in the extra-tropics but with its amplitude, structure and time of occurrence being strongly dependent on the distance of the forcing to the wave guide, i.e. the jet stream. A quasi-linear relationship was found between both the minimum and the mean minimum distance of the forcing to the wave guide and the downstream reach of the impact by the tropical heating. The extra-tropical response to the heating was primarily confined to the mid-latitude wave guide. Pole-ward perturbations were only evident in the case where the forcing generated enhanced excursions of preexisting troughs and ridges and for wave breaking yielding the intrusion of mid-latitude

air into the higher latitudes. Thus the pole-ward response in the experiments is not explainable by linear Rossby wave dispersion.

The response along the wave guide always resembles the characteristics of downstream development with an opposite vertical phase tilt of geopotential height and temperature in the lower troposphere resembling the structure of a growing baroclinic wave. The maximum perturbation in geopotential height is near the tropopause and always precedes the perturbations near the ground in accordance to earlier modeling work and regression analysis on an atmospheric data set. An analysis of the Hovmöller diagrams yielded phase and group velocities of 9 and 30 m s⁻¹, respectively, where the group velocity was found to be close to but still smaller than the mean zonal jet speed along the wave guide.

Since previous studies indicated that the North Pacific mid-latitude wave guide is a region of frequent occurrence of downstream development it appears feasible to assign the role of triggering these wave trains to the convective activity over the tropical Pacific warm pool area. In fact the results presented here strongly encourage this interpretation. Of course similar arguments apply for other regions on the globe where tropical heating occurs in the proximity of a wave guide such as e.g. the western Atlantic Ocean.

The radius and magnitude of the tropical heating were found to project linearly onto the amplitude of the extra-tropical response indicating that the dynamics involved in the initiation of the first perturbation along the wave guide might be explainable by linear theory. In fact the applicability of a simple model with a balanced vortex impacting on a PV interface at some distance proved very useful in interpreting the results. This implies that the interaction of the tropical heating with the wave guide is dominated by the distant impact of a balanced perturbation in contrast to Rossby waves emerging directly from the tropics and dispersing into the mid-latitudes.

However, some open questions remain. While the response to a single mountain with a weak zonally symmetric jet yielded a response resembling the characteristics of a great circle similar to a pattern such as the PNA the simulations with a stronger baroclinic and meandering jet did not feature the large scale stationary wave response. Earlier studies always highlighted the zonal asymmetries of the climatological mean state as one of the key ingredients in order to obtain a pattern similar to the PNA. Since the time mean state of the baroclinic setup chosen is zonally symmetric the lack of zonal asymmetry might in fact explain the deficiency of our experiments to reproduce a pattern similar to the PNA. But there is also the absence of orography and land-sea contrast in our model simulations which in fact might also play a crucial role in interacting with the downstream developing baroclinic wave train and the importance of those interactions in setting up the PNA pattern remain yet to be determined.

Still, it seems equivocal that the response of a tropical forcing in an idealized initial symmetric basic state is able to reproduce patterns similar to the PNA and on the other hand a setting with a baroclinic meandering jet which actually comprises a zonally symmetric climatological mean state yields a very distinct result. One possible implication is that the non-linear interactions between the forcing and the mid-latitude wave guide, which are argued to be important in the generation of a pattern like the PNA, are altered by an asymmetry of the time averaged basic state yielding preferred regions for wave breaking and areas in favor for shifting preexisting troughs and ridges. However, further analysis is needed to dynamically pinpoint these aspects in the generation of the PNA teleconnection pattern.

Bibliography

- Abramowitz, M. and Stegun, I. A.: Handbook of Mathematical Functions with Formulas, Graphs, and Mathematical Tables, Dover, New York, ninth dover printing, tenth gpo printing edn., 1964.
- Barnston, A. G. and Livezey, R. E.: Classification, Seasonality and Persistence of low-frequency Atmospheric Circulation Patterns, *Mon. Wea. Rev.*, 115, 1083–1126, 1987.
- Bjerknes, J.: Atlantic air-sea interaction, *Adv. Geophys.*, 10, 1–82, 1964.
- Bjerknes, J.: A possible response of the atmospheric circulation to equatorial anomalies of ocean temperatures, *Tellus*, 18, 820–829, 1966.
- Bjerknes, J.: Atmospheric teleconnections from the equatorial Pacific, *Mon. Wea. Rev.*, 97, 163–172, 1969.
- Borges, M. D. and Sardeshmukh, P. D.: Barotropic Rossby wave dynamics of zonally varying upper-level flows during northern winter, *J. Atmos. Sci.*, 52, 3779–3796, 1995.
- Branstator, G.: Analysis of general circulation model sea-surface temperature anomaly simulations using a linear model. Part I: Forced solutions, *J. Atmos. Sci.*, 42, 1037–1049, 1985.
- Branstator, G.: Low-frequency patterns induced by stationary waves, *J. Atmos. Sci.*, 47, 629–648, 1990.
- Branstator, G.: The maintenance of low-frequency atmospheric anomalies, *J. Atmos. Sci.*, 49, 1924–1945, 1992.
- Branstator, G.: Organization of storm track anomalies by recurring low-frequency circulation anomalies, *J. Atmos. Sci.*, 52, 207–226, 1995.
- Brillouin, L.: La mécanique ondulatoire de Schrödinger: une méthode générale de resolution par approximations successives, *Comptes Rendus de l'Academie des Sciences*, 183, 24–26, 1926.
- Brunet, G. and Haynes, P. H.: Low-latitude reflection of Rossby wave trains, *J. Atmos. Sci.*, 53, 482–496, 1996.
- Chang, E. K. M.: Downstream Development of Baroclinic Waves as Inferred from Regression Analysis, *J. Atmos. Sci.*, 50, 2038–2053, 1993.
- Chang, E. K. M.: Characteristics of Wave Packets in the Upper Troposphere. Part II: Seasonal and Hemispheric Variations, *J. Atmos. Sci.*, 56, 1729–1747, 1999.
- Chang, E. K. M. and Yu, D. B.: Characteristics of Wave Packets in the Upper Troposphere. Part I: Northern Hemisphere Winter, *J. Atmos. Sci.*, 56, 1708–1728, 1999.
- Charney, J. G.: The Dynamics of Long Waves in a Baroclinic westerly Current, *J. Meteor.*, 4, 135–162, 1947.
- Charney, J. G. and Drazin, P. G.: Propagation of planetary-scale disturbances from the lower into the upper atmosphere, *J. Geophys. Res.*, 66, 83–110, 1961.
- Charney, J. G. and Eliassen, A.: A numerical method for predicting the perturbations of the middle latitudes westerlies, *Tellus*, 1, 38–54, 1949.
- Danielson, R. E., Gyakum, J. R., and Straub, D. N.: A Case study of downstream baroclinic development over the North Pacific Ocean. Part I: Diagnoses of eddy energy and wave activity, *Mon. Wea. Rev.*, 134, 1549–1567, 2006.
- Davies, H. C.: Limitations of some common lateral boundary schemes in regional NWP models, *Mon. Wea. Rev.*, 111, 2013–2020, 1983.

- Defant, A.: Die Schwankungen der atmosphärischen Zirkulation über dem Nordatlantischen Ozean im 25-jährigen Zeitraum 1881-1905, *Geogr. Ann.*, 6, 13–41, 1924.
- Dickinson, R. E.: Planetary Rossby waves propagating vertically through weak westerly wind waveguides, *J. Atmos. Sci.*, 25, 984–1002, 1968.
- Dickinson, R. E.: Development of a Rossby wave critical layer, *J. Atmos. Sci.*, 27, 627–633, 1970.
- Drazin, P. G., Beaumont, D. N., and Coaker, S. A.: On Rossby waves modified by basic shear, and barotropic instability, *J. Fluid. Mech.*, 124, 439–456, 1982.
- Eady, E. T.: Long waves and cyclone waves, *Tellus*, 1, 33–52, 1949.
- ECMWF: IFS Documentation - CY31r1, Operational implementation 12 September 2006; Part III: Dynamics and Numerical Procedures, Tech. rep., European Centre for Medium Range Weather Forecasts, URL <http://www.ecmwf.int/research/ifsdocs/CY31r1/index.html>, 2007.
- Egger, J.: The linear response of a hemispheric two-level primitive equation model to forcing by topography, *Mon. Wea. Rev.*, 104, 351–364, 1976a.
- Egger, J.: On the theory of the steady perturbations in the troposphere, *Tellus*, 28, 381–389, 1976b.
- Egger, J. and Schilling, H.-D.: On the Theory of the Long-Term Variability of the Atmosphere, *J. Atmos. Sci.*, 40, 1073–1085, 1983.
- Eliassen, A. and Palm, E.: On the transfer of energy in stationary mountain waves, *Geofysiske Publikasjoner*, 22 (3), 1–22, 1961.
- Exner, F. M.: Übermonatliche Witterungsanomalien auf der nördlichen Erdhälfte im Winter, *Sitzungsberichte d. Kaiserl. Akad. der Wissenschaften*, 122, 1165–1241, 1913.
- Exner, F. M.: Monatliche Luftdruck- und Temperaturanomalien auf der Erde, *Sitzungsberichte d. Kaiserl. Akad. der Wissenschaften*, 133, 307–408, 1924.
- Farrell, B. F.: Pulse asymptotics of three-dimensional baroclinic waves, *J. Atmos. Sci.*, 40, 2202–2210, 1983.
- Feldstein, S. B.: Fundamental mechanisms of the growth and decay of the PNA teleconnection pattern, *Quart. J. Roy. Meteor. Soc.*, 128, 775–796, 2002.
- Ferranti, L., Palmer, T. N., Molteni, F., and Klinker, E.: Tropical-Extratropical Interaction Associated with the 30-60 Day Oscillation and Its Impact on Medium and Extended Range Prediction, *J. Atmos. Sci.*, 47, 2177–2199, 1990.
- Frederiksen, J. S.: A unified three-dimensional instability theory of the onset of blocking and cyclogenesis. II: Teleconnection patterns, *J. Atmos. Sci.*, 40, 2593–2609, 1983.
- Frederiksen, J. S. and Webster, P. J.: Alternative theories of atmospheric teleconnections and low-frequency fluctuations, *Rev. Geophys.*, 26, 459–494, 1988.
- Gill, A. E.: Some simple solutions for heat-induced tropical circulation, *Quart. J. Roy. Meteor. Soc.*, 106, 447–462, 1980.
- Grose, W. L. and Hoskins, B. J.: On the influence of Orography on Large-Scale Atmospheric Flow, *J. Atmos. Sci.*, 36, 223–234, 1979.
- Hakim, G. J.: Developing wave packets in the North Pacific storm track, *Mon. Wea. Rev.*, 131, 2824–2837, 2003.
- Harlander, U., Schönfeld, H.-J., and Metz, W.: Rossby waveguides in high-latitude shear flows with boundaries, *J. Geophys. Res.*, 105, 17 063–17 078, 2000.
- Harlander, U., Gassmann, A., and Metz, W.: Stationary Rossby wave propagation in a shear-flow along a reflective boundary, *Meteorol. Atmos. Phys.*, 78, 245–260, 2001.
- Held, I. M. and Suarez, M. J.: A Proposal for the Intercomparison of the Dynamical Cores of Atmospheric General Circulation Models, *Bull. Amer. Meteor. Soc.*, 75, 1825–1830, 1994.

- Held, I. M. and Ting, M.: Orographic versus thermal forcing of stationary waves: The importance of the mean low-level wind, *J. Atmos. Sci.*, 47, 495–500, 1990.
- Held, I. M., Tingand, M., and Wang, H.: Northern Winter Stationary Waves: Theory and Modeling, *J. Climate*, 15, 2125–2144, 2002.
- Hendon, H. H. and Salby, M. L.: The Life Cycle of the Madden-Julian Oscillation, *J. Atmos. Sci.*, 51, 2225–2237, 1994.
- Hendon, H. H. and Salby, M. L.: Planetary-Scale Circulations Forced by Intraseasonal Variations of Observed Convection, *J. Atmos. Sci.*, 53, 1751–1758, 1996.
- Hendon, H. H., Liebmann, B., Newman, M., Glick, J. D., and Schemm, J. E.: Medium-Range Forecast Errors Associated with Active Episodes of the Madden-Julian Oscillation, *Mon. Wea. Rev.*, 128, 69–86, 2000.
- Higgins, R. W. and Mo, K. C.: Persistent north Pacific circulation anomalies and the tropical intraseasonal oscillation, *J. Climate*, 10, 223–244, 1997.
- Horel, J. D. and Wallace, J. M.: Planetary-Scale Atmospheric Phenomena Associated with the Southern Oscillation, *Mon. Wea. Rev.*, 109, 813–829, 1981.
- Hoskins, B. J. and Ambrizzi, T.: Rossby wave propagation on a realistic longitudinally varying flow, *J. Atmos. Sci.*, 50, 1661–1671, 1993.
- Hoskins, B. J. and Karoly, D. J.: The steady linear response of a spherical atmosphere to thermal and orographic forcing, *J. Atmos. Sci.*, 38, 1179–1196, 1981.
- Hoskins, B. J., Simmons, A. J., and Andrews, D. G.: Energy dispersion in a barotropic atmosphere, *Quart. J. Roy. Meteor. Soc.*, 103, 553–567, 1977.
- Hovmöller, E.: The trough ridge diagram, *Tellus*, 1, 62–66, 1949.
- Hsu, H. H.: Global view of the intraseasonal oscillation during northern winter, *J. Climate*, 9, 2386–2406, 1996.
- Jeffreys, H.: On certain approximate solutions of linear differential equations of the second order, *Proc. London Math. Soc.*, 23, 428–436, 1924.
- Jin, F. and Hoskins, B. J.: The direct response to tropical heating in a baroclinic atmosphere, *J. Atmos. Sci.*, 52, 307–319, 1995.
- Jin, F.-F., Pan, L.-L., and Watanabe, M.: Dynamics of Synoptic Eddy and Low-Frequency Flow Interaction. Part I: A linear Closure, *J. Atmos. Sci.*, 63, 1677–1694, 2006.
- Karoly, D. J.: Rossby wave propagation in a barotropic atmosphere, *Dyn. Atmos. Oceans*, 7, 111–125, 1983.
- Kiladis, G. N. and Weickmann, K. M.: Circulation anomalies associated with tropical convection during northern winter, *Mon. Wea. Rev.*, 120, 1900–1923, 1992.
- Killworth, P. D. and McIntyre, M. E.: Do Rossby wave critical layers absorb, reflect, or over-reflect?, *J. Fluid. Mech.*, 161, 449–492, 1985.
- Kim, B.-M., Lim, G., and Kim, K.-Y.: A new look at the midlatitude-MJO teleconnection in the northern hemisphere winter, *Quart. J. Roy. Meteor. Soc.*, 132, 485–503, 2006.
- Knutson, T. and Weickmann, K. M.: 30-60 day atmospheric oscillations: Composite life cycles of convection and circulation anomalies, *Mon. Wea. Rev.*, 115, 1407–1436, 1987.
- Kramers, H. A.: Wellenmechanik und halbzahlige Quantisierung, *Zeit. Physik*, 39, 1407–1436, 1926.
- Lau, K. M. and Phillips, T. J.: Coherent fluctuations of extratropical geopotential height and tropical convection in intraseasonal time scales, *J. Atmos. Sci.*, 43, 1164–1181, 1986.
- Liebmann, B. and Hartmann, D.: An observational study of tropical-midlatitude interaction on intraseasonal time scales during winter, *J. Atmos. Sci.*, 41, 3333–3350, 1984.

- Lim, H. and Chang, C. P.: Dynamics of teleconnections and Walker circulations forced by equatorial heating, *J. Atmos. Sci.*, 40, 1897–1915, 1983.
- Lin, H. and Derome, J.: Nonlinearity of the Extratropical Response to Tropical Forcing, *J. Climate*, 17, 2597–2608, 2004.
- Lindzen, R. S., Aso, T., and Jacqmin, D.: Linearized Calculations of Stationary Waves in the Atmosphere, *J. Meteor. Soc. Japan*, 60, 66–77, 1982.
- Madden, R. A. and Julian, P. R.: Detection of a 40-50 day oscillation in the zonal wind in the tropical Pacific, *J. Atmos. Sci.*, 28, 702–708, 1971.
- Madden, R. A. and Julian, P. R.: Description of a 40-50 day oscillation in the zonal wind in the tropical Pacific, *J. Atmos. Sci.*, 28, 702–708, 1972.
- Madden, R. A. and Julian, P. R.: Observations of the 40-50-day Tropical Oscillation-A Review, *Mon. Wea. Rev.*, 122, 814–837, 1994.
- Matsuno, T.: Quasi-geostrophic motions in the equatorial area, *J. Meteor. Soc. Japan*, 44, 25–43, 1966.
- Matsuno, T.: Vertical Propagation of Stationary Planetary Waves in the Winter Northern Hemisphere, *J. Atmos. Sci.*, 27, 871–883, 1970.
- Matsuno, T.: A Dynamical Model of the Stratospheric Sudden Warming, *J. Atmos. Sci.*, 28, 1479–1494, 1971.
- Matthews, A. J.: Propagation mechanism for the Madden-Julian Oscillation, *Quart. J. Roy. Meteor. Soc.*, 126, 2637–2651, 2000.
- Matthews, A. J. and Kiladis, G. N.: The Tropical-Extratropical Interaction between the High-Frequency Transients and the Madden-Julian-Oscillation, *Mon. Wea. Rev.*, 127, 661–677, 1999.
- Matthews, A. J., Hoskins, B. J., and Masutani, M.: The global response to tropical heating in the Madden-Julian oscillation during the northern winter, *Quart. J. Roy. Meteor. Soc.*, 130, 1991–2011, 2004.
- McIntyre, M. E.: How well do we Understand the Dynamics of Stratospheric Warmings?, *J. Meteor. Soc. Japan*, 60, 37–65, 1982.
- Moncrieff, M., Waliser, D., and Coauthors: Year of Tropical Convection (YOTC): A joint WCRP-WWRP/THORPEX International Initiative, 2008.
- Mori, M. and Watanabe, M.: The Growth and Triggering Mechanisms on the PNA: A MJO-PNA Coherence, *J. Meteor. Soc. Japan*, 86, 213–236, 2008.
- Nakamura, H. and Wallace, J. M.: Synoptic behavior and baroclinic eddies during the blocking onset, *Mon. Wea. Rev.*, 121, 1892–1903, 1993.
- Pedlosky, J.: *Geophysical Fluid Dynamics*, 710 pp, Springer-Verlag New York, 1987.
- Pierrehumbert, R. T.: Stratified semigeostrophic flow over two-dimensional topography in an unbounded atmosphere, *J. Atmos. Sci.*, 42, 523–526, 1985.
- Pierrehumbert, R. T. and Swanson, K. L.: Baroclinic instability, *Ann. Rev. Fluid Mech.*, 27, 419–467, 1995.
- Rossby, C. G.: Relation between variations in the intensity of the zonal circulation of the atmosphere and the displacement of semi-permanent centers of action, *J. Mar. Res.*, 2, 38–55, 1939.
- Salby, M. L., Garcia, R. R., and Hendon, H. H.: Planetary-Scale Circulations in the Presence of Climatological and Wave-Induced Heating, *J. Atmos. Sci.*, 51, 2344–2367, 1994.
- Sardeshmukh, P. D. and Hoskins, B. J.: The generation of global rotational flow by steady idealized tropical divergence, *J. Atmos. Sci.*, 45, 1228–1251, 1988.
- Schwierz, C., Dirren, S., and Davies, H. C.: Forced waves on a zonally aligned jet stream, *J. Atmos. Sci.*, 61, 73–87, 2004.

- Scott, R. K. and Polvani, L. M.: Internal Variability of the Winter Stratosphere: Part I: Time-Independent Forcing, *J. Atmos. Sci.*, 63, 2758–2776, 2006.
- Simmons, A. J.: The forcing of stationary wave motion by tropical diabatic heating, *Quart. J. Roy. Meteor. Soc.*, 108, 503–534, 1982.
- Simmons, A. J. and Burridge, D. M.: An energy and angular momentum conserving vertical finite difference scheme and hybrid vertical coordinates, *Mon. Wea. Rev.*, 109, 758–766, 1981.
- Simmons, A. J. and Hoskins, B. J.: The Downstream and Upstream Development of Unstable Baroclinic Waves, *J. Atmos. Sci.*, 36, 1239–1254, 1979.
- Simmons, A. J., Wallace, J. M., and Branstator, G. W.: Barotropic wave propagation and instability, and atmospheric teleconnection patterns, *J. Atmos. Sci.*, 40, 1363–1392, 1983.
- Smagorinsky, J.: The dynamical influence of large-scale heat sources and sinks on the quasi-stationary mean motions of the atmosphere, *Quart. J. Roy. Meteor. Soc.*, 79, 342–366, 1953.
- Takaya, K. and Nakamura, H.: A formulation of a wave-activity flux for stationary Rossby waves on a zonally varying basic flow, *Geophys. Res. Lett.*, 24, 2985–2988, 1997a.
- Takaya, K. and Nakamura, H.: A formulation of a phase-independent wave-activity flux for stationary and migratory quasigeostrophic eddies on a zonally varying basic flow, *J. Atmos. Sci.*, 24, 608–627, 1997b.
- Ting, M.: Maintenance of northern summer stationary waves in a GCM, *J. Atmos. Sci.*, 51, 3286–3308, 1994.
- Ting, M. and Held, I. M.: The stationary wave response to a tropical SST anomaly in an idealized GCM, *J. Atmos. Sci.*, 47, 2546–2566, 1990.
- Ting, M. and Sardeshmukh, P. D.: Factors determining the extra-tropical response to equatorial diabatic heating anomalies, *J. Atmos. Sci.*, 50, 907–918, 1993.
- Ting, M. and Yu, L.: Steady response to tropical heating in a wavy linear and nonlinear baroclinic models, *J. Atmos. Sci.*, 55, 3565–3582, 1998.
- Uppala, S. and Coauthors: The ERA-40 re-analysis, *Quart. J. Roy. Meteor. Soc.*, 131, 2961–3012, 2005.
- Valdes, P. J. and Hoskins, B. J.: Linear Stationary Waves of the Time-Mean Climatological Flow, *J. Atmos. Sci.*, 46, 2509–2527, 1989.
- Walker, G. T.: Correlation in seasonal variation of climate, *Mem. Ind. Met. Dept.*, 20, 122, 1909.
- Walker, G. T.: Correlation in seasonal variation of weather, IX, *Mem. Roy. Meteor. Soc.*, 4, 53–84, 1924.
- Walker, G. T. and Bliss, E. W.: World Weather V, *Mem. Roy. Meteor. Soc.*, 4, 53–84, 1932.
- Wallace, J. M. and Gutzler, D. S.: Teleconnections in the geopotential height field during the northern hemisphere winter, *Mon. Wea. Rev.*, 109, 784–812, 1981.
- Wang, H. and Ting, M.: Seasonal cycle in the climatological stationary waves in the NCEP-NCAR reanalysis, *J. Atmos. Sci.*, 56, 3892–3919, 1999.
- Wanner, H., Brönnimann, S., Casty, C., Gyalistras, D., Luterbacher, J., Schmutz, C., Stephenson, D. B., and Xoplaki, E.: North Atlantic Oscillation-Concepts and studies, *Surveys in Geophys.*, 22, 321–382, 2001.
- Webster, P. J.: Response of the tropical atmosphere to local steady forcing, *Mon. Wea. Rev.*, 100, 518–540, 1972.
- Wentzel, G.: Eine Verallgemeinerung der Quantenbedingungen für die Zwecke der Wellenmechanik, *Zeit. Physik*, 38, 518–529, 1926.
- Wurtele, M. G., Sharman, R. D., and Keller, T. L.: Analysis and Simulations of a Troposphere-Stratosphere Gravity Wave Model. Part I, *J. Atmos. Sci.*, 44, 3269–3281, 1987.

- Zhang, C.: Madden-Julian oscillation, *Rev. Geophys.*, 43, RG2003, doi:10.1029/2004RG000158, 2005.
- Zhang, C., Dong, M., Gualdi, S., Hendon, H. H., Maloney, E. D., Marshall, A., Sperber, K. R., and Wang, W.: Simulations of the Madden-Julian oscillation in four pairs of coupled and uncoupled global models, *Clim. Dynam.*, 27, 573–592, 2006.

Curriculum Vitae

PERSONAL DETAILS

Name	Spengler	First Name	Thomas
Date of Birth	4th September 1978	Place of Birth	Munich, Germany
Citizenship	German		

UNIVERSITY EDUCATION

Doctorate in Atmospheric Science	2005 - 2008
Institute for Atmospheric and Climate Science (IAC), ETH Zurich, Switzerland	
Thesis: Influence of the ambient flow upon Rossby wave propagation between the tropics and extra-tropics	
Diploma in Meteorology	2001 - 2005
Meteorological Institute Munich, University of Munich, Germany	
Thesis: The Dynamics of Heat Lows in simple background Flows	
Study of Atmospheric Sciences (supported by a DAAD scholarship)	2002
School of Mathematics, Monash University, Melbourne Australia	
Intermediate Diploma in Meteorology	1999 - 2001
Meteorological Institute Munich, University of Munich, Germany	

INTERNSHIPS AND PARTICIPATION IN FIELD EXPERIMENTS

Participation in the Irminger Sea Cruise Kn194 with the Research Vessel Knorr	2008
Irminger Sea	
Participation in the IPY-Thorpex Andøya-campaign	2008
Norway	
Participation in the Flow over and around Hofjökull Experiment (FLOHOF)	2007
Iceland	
Head of the Allgäu Experiment (AllgEx) in south-eastern Bavaria	2005
Germany	
Participation in the Arctic Cruise ARK XX/3 with the Research Vessel Polarstern	2004
Polar Sea	
Internship at the Alfred Wegener Institute for Polar and Marine Research	2004
Bremerhaven, Germany	
Participation in the Gulf Line Experiment (GLEX)	2002
Northern Australia	
Research assistant at the School of Mathematical Sciences	2002
Monash University, Melbourne, Australia	

TEACHING EXPERIENCE

Tutorials for: Environmental Fluid Dynamics Part I ETH Zurich	2006, 2007, 2008, 2009
Tutorials for: Dynamics of large scale flow ETH Zurich	2007, 2008, 2009
Bachelor Seminar: Atmosphere and Climate ETH Zurich	2006, 2007, 2009
Weather Discussion ETH Zurich	2007, 2008

VOCATIONAL TRAINING

Project management for supervising bachelor and master thesis ETH Zurich	2008
Rhetoric tools for teaching ETH Zurich	2008
Rhetoric for seminar and lecture ETH Zurich	2008
Presenting-Publishing-Communicating ETH Zurich	2007
Newcomers Workshop (Presenting-Teaching-Communicating) ETH Zurich	2007
How to write and publish a scientific paper ETH Zurich	2006

COMPUTING EXPERIENCES

Programming:

FORTRAN, Matlab, shell scripts

Visualization tools:

NCAR Graphics, GrADS

Systems:

UNIX, Linux, Windows, Macintosh

Software:

Microsoft Office, Maple

SUPERVISION OF STUDENTS

Brunner N. E. (Master Thesis, 2008) Forced stationary Rossby waves in an equatorial beta-plane one-layer shallow water model	ETH Zurich
Tay P. (Semester Thesis, 2007) Forced Quasi-Geostrophic Rossby Waves in a stratified Fluid	ETH Zurich
Čampa J. (Diploma Thesis, 2007) Interactions of Forced sub-tropical Rossby Waves with extra-tropical Flow	ETH Zurich
Ablinger M. (Diploma Thesis, 2007) Data and Results from the field campaign AllgEx in the Allgäu	University of Munich

INTERNATIONAL CONFERENCES AND WORKSHOPS

IPY-Thorpex-Norway annual meeting Rømskog (Norway)	January 2009
Conference on Teleconnection in Atmosphere and Oceans ICTP Trieste (Italy)	November 2008
AMMA Conference Karlsruhe (Germany)	November 2007
7th EMS / 8th ECAM Meeting San Lorenzo de El Escorial (Spain)	October 2007
LATSIS Symposium Zurich (Switzerland)	September 2007
DACH Hamburg (Germany)	September 2007
IUGG Perugia, (Italy)	July 2007
THORPEX STISS Meeting Landshut (Germany)	December 2006
13th Cyclone Workshop Monterey, California (USA)	October 2006
EGU General Assembly Vienna (Austria)	April 2006
9th national AMOS Conference Brisbane, (Australia)	July 2004
11th national AMOS Conference Melbourne, (Australia)	February 2002

SCIENTIFIC COLLABORATIONS

Heat Low dynamics Prof. Dr. Roger K. Smith	University of Munich, Germany
Rosby wave activity flux Prof. Dr. Michael J. Reeder	Monash University, Australia
Orographic and themally driven flow phenomena em. Prof. Dr. Joseph Egger	University of Munich, Germany
Greenland Tip Jet Kjetil Våge and Dr. Robert Pickart	Woods Hole Oceanographic Institution, USA
Interaction MJO - mid-latitudes Prof. Dr. Richard Moore	Naval Postgraduate School, Monterey, USA

PUBLICATIONS

Reviewed Articles

Spengler, T. and Smith, R. K.: The dynamics of heat lows over flat terrain. *Quart. J. Roy. Meteor. Soc.*, **134**, Oct B, 2157-2172

Spengler, T., Reeder, M. J. and Smith, R. K., 2005: The Dynamics of Heat Lows in Simple Background Flows. *Quart. J. Roy. Meteor. Soc.*, **131**, Oct B, 3147-3166

Jackson, G. E., Smith, R. K. and Spengler, T., 2002: The Prediction of low-level convergence lines over northeastern Australia. *Aust. Meteor. Mag.*, **51**, 13-23

Submitted Articles

Våge, K., Spengler, T. and Davies, H. C.: Multi-event analysis of the Greenland tip jet based on 45 winters in ERA-40. *Climatology. Quart. J. Roy. Meteor. Soc.*, *submitted*

Spengler, T., Ablinger, M., Schween, J. H., Zängl, G. and Egger, J.: Thermally driven Flows at an asymmetric valley exit: Observations and Model Studies at the Lech Valley exit. *Mon. Wea. Rev.*, *submitted*

Spengler, T. and Egger, J.: Comments on "Dry-Season Precipitation in Tropical West Africa and Its Relation to Forcing from the Extratropics". *Mon. Wea. Rev.*, *submitted*

Extended Abstracts

Spengler, T., Schwiertz C. and Davies, H. C., 2006: Sub-tropical synoptic-scale forcing of extra-tropical flow: Diagnostic analysis and model simulations. *Second THORPEX International Science Symposium (STISS) Extended Abstracts*, 88-89

Articles in preparation

Spengler, T. and Davies, H. C.: On stationary Rossby waves modified by basic shear. *in prep.*

Spengler, T., Čampa, J. and Davies, H. C.: Extra-tropical Response to sub-tropical Forcing: Global simulations with idealized jet. *in prep.*

Spengler, T., Čampa, J. and Davies, H. C.: Mid-latitude response to stationary and non-stationary tropical heating: Non-linear global Simulations with a zonally asymmetric Jet Stream. *in prep.*

Moore, R., Martius, O., Spengler, T. and Davies, H. C.: The modulation of extratropical wave breaking and surface weather patterns by the Madden Julian Oscillation. *in prep.*

Spengler, T., A. Dörnbrack, M. Weissmann, and S. Rahm, Våge, K., G. W. K. Moore and Davies, H. C.: The wind field in the lee of Greenland during a tip jet event – Airborne Doppler observations and meteorological modelling. *in prep.*

Egger, J. and Spengler, T.: Surface pressure adjustment to atmospheric temperature anomalies. *in prep.*

Egger, J. and Spengler, T.: Does rain affect surface pressure. *in prep.*

Acknowledgements

I would like to thank Huw Davies for the opportunity of being his last Doctoral student at IACETH. I really enjoyed the stimulating discussions and greatly appreciated the humor present in all the meetings we had. I truly learnt a lot about science and scientific politics the last three years which I am very grateful for. Above all I am much obliged for the freedom in research he gave me the last three years.

Special thanks are due to Sepp Egger. He actually was the one encouraging me applying for a Doctorate at ETH with Huw Davies. I admire his incessant enthusiasm for research which definitely was an inspiration for my own scientific career. I would also like to thank Sepp for the opportunity of financing my own field experiment at the begin of my dissertation and for taking me on a field trip to Iceland.

Furthermore I would like to thank the IACETH for providing an interesting environment to work in and particularly Eva Choffat for keeping everything running so smoothly regarding organizational issues. I would especially like to thank all the members of our Dynamics group: Olivia, Marco, Johannes, Sarah, Dani, Rich, Linda, Jana, Michael, Mischa, Harald, Kjetil and Sandro who contributed to a stimulating scientific environment during the last three years.

Gratefully acknowledged are ECMWF for providing ECWF ERA40 data and the support in getting started with the IFS system. Special thanks are due to Nils Wedi who continuously helped me when I ran into coding problems with the IFS.

And of course last but not least: Ich danke meiner Familie für die allzeitige Unterstützung in all den Jahren, allen voran meinen Eltern die immer an mich geglaubt haben und für mich da waren.